[redacted]

X72-10684

NASA TM X-2584

NASA TECHNICAL MEMORANDUM

NASA TM X-2584

CLASSIFICATION CHANGE

UNCLASSIFIED

To [redacted]

By [redacted], NASA

Cl[redacted]

Cl[redacted]

Scientific and Technical Information Facility

[redacted] CLASSIFIED

BY [redacted]

SU[redacted]

[redacted] INTERVALS AND DECLASSIFI[redacted]

[redacted]

CASE FILE COPY

BOUNDARY-LAYER EDGE CONDITIONS AND TRANSITION REYNOLDS NUMBER DATA FOR A FLIGHT TEST AT MACH 20 (REENTRY F)

by C. B. Johnson, P. C. Stainback,
K. C. Wicker, and L. R. Boney

Langley Research Center
Hampton, Va. 23365

NATIONAL AERONAUTICS AND SPACE ADMINISTRATION • WASHINGTON, D. C. • JULY 1972

[redacted]

[redacted]

1. Report No.	2. Government Accession No.	3. Recipient's Catalog No.
NASA TM X-2584		

4. Title and Subtitle	5. Report Date
BOUNDARY-LAYER EDGE CONDITIONS AND TRANSITION REYNOLDS NUMBER DATA FOR A FLIGHT TEST AT MACH 20 (REENTRY F) (U)	July 1972
	6. Performing Organization Code
7. Author(s) Charles B. Johnson, P. Calvin Stainback, Kathleen C. Wicker, and Lillian R. Boney	8. Performing Organization Report No. L-8313
	10. Work Unit No. 136-13-04-01
9. Performing Organization Name and Address NASA Langley Research Center Hampton, Va. 23365	11. Contract or Grant No.
	13. Type of Report and Period Covered Technical Memorandum
12. Sponsoring Agency Name and Address National Aeronautics and Space Administration Washington, D.C. 20546	14. Sponsoring Agency Code

15. Supplementary Notes

16. Abstract

Boundary-layer edge conditions that account for the effects of the entropy layer were calculated for a flight vehicle designated Reentry F. Calculations were made over an altitude range from 36.58 to 18.29 km (120 000 to 60 000 ft) at a flight velocity of approximately 6.069 km/sec (20 000 ft/sec). Local transition Reynolds numbers are presented and are correlated with previous flight data over a Mach number range from 3 to 12. The parameters used in the correlations include the effects of local unit Reynolds number, boundary-layer wall-to-edge enthalpy ratio, and local Mach number.

[redacted] Confidential [redacted] CLASSIFIED
[redacted] DECLASSIFICATION SCHEDULE [redacted] 11652. AUTOMATIC [redacted] INTERVALS AND DECLASSIFICATION [redacted] 1978.

NATIONAL SECURITY INFORMATION

UNAUTHORIZED DISCLOSURE SUBJECT TO CRIMINAL SANCTIONS

17. Key Words (Suggested by Author(s))	18. Distribution Statement
Boundary-layer edge conditions Free-flight cone Boundary-layer transition Variable-entropy edge conditions	[redacted] Available to U.S. Government Agencies and Their Contractors Only

19. Security Classif. (of this report)	20. Security Classif. (of this page)	21. No. of Pages	22. Price
[redacted]	Unclassified	81	

[redacted]

[redacted]

[redacted]

BOUNDARY-LAYER EDGE CONDITIONS AND TRANSITION REYNOLDS NUMBER DATA FOR A FLIGHT TEST AT MACH 20 (REENTRY F)*

By Charles B. Johnson, P. Calvin Stainback,
Kathleen C. Wicker, and Lillian R. Boney
Langley Research Center

SUMMARY

A flight experiment, designated Reentry F, was conducted to measure heat-transfer rates for laminar, transitional, and turbulent boundary layers on a 5° half-angle cone 3.962 m (13 ft) long with a preflight nose radius of 2.54 mm (0.10 in.). Data were obtained over an altitude range from 36.58 to 18.29 km (120 000 to 60 000 ft) at a flight velocity of about 6.096 km/sec (20 000 ft/sec). The nominal values of the free-stream total enthalpy, sharp-cone Mach number, and the wall-to-total enthalpy ratio were 18 MJ/kg (8000 Btu/lb), 15, and 0.03, respectively.

Calculated boundary-layer edge conditions that account for effects of the entropy layer and corresponding local transition Reynolds numbers are reported in the present paper. Fully developed turbulent flow occurred with essentially constant boundary-layer edge conditions near the sharp-cone values. Transition data were obtained with local edge Mach numbers ranging from about 5.55 to 15. Transition Reynolds numbers, based on local condition, were as high as 6.6×10^7 with an edge Mach number of about 14.4 at an altitude of 24.38 km (80 000 ft). The transition could be correlated with previous flight data taken over a Mach number range from 3 to 12 in terms of parameters including the effects of local unit Reynolds number, boundary-layer wall-to-edge enthalpy ratio, and local Mach number.

INTRODUCTION

The optimization of heat protection systems for vehicles that operate at high Mach numbers in the atmosphere requires reliable predictions for heating rates, particularly transitional and turbulent heating rates. Existing theoretical prediction methods are based on data obtained in ground facilities and limited flight experiments. (See refs. 1 to 3.) Most of these test conditions fall significantly short of those experienced by reentry vehicles operating at high Mach numbers.

*Title, Unclassified.

[redacted]

Because of the limitations in previous transitional and turbulent heat-transfer data, the Reentry F flight experiment was conducted to obtain heating and transition data at boundary-layer edge Mach numbers up to 15, total enthalpies of about 18 MJ/kg (8000 Btu/lb), and wall-to-total enthalpy ratios of about 0.03. These data will extend the range of existing data and can also be used to evaluate current theories for turbulent boundary layers (refs. 2 and 3) and to guide future development of these theories.

Initial results from the experiment were reported in reference 4. The basic measurements and analysis of results have been reported in references 5, 6, 7, 8, 9, 10, and 11. Some of the work in these references, particularly that concerned with heat transfer and boundary-layer transition, required knowledge of the local flow conditions. These local conditions, used in the references, were taken from initial results of the computation of boundary-layer edge conditions presented herein. This report discusses the methods used and presents the final results for the calculated boundary-layer edge conditions for the Reentry F flight experiment. The results of a study of the correlation of the Reentry F transition data (refs. 4 and 5) with other flight data will also be presented. The effects of vehicle nose geometry, angle of attack, and Reynolds number on transition are presented on the basis of ground test data at Mach 8.

SYMBOLS

Values are given in both SI and U.S. Customary Units. The measurements and calculations were made in U.S. Customary Units.

A,B constants in equation (2)

a_{ij} coefficients in equation (1)

D base diameter of model

$$F_1 = M_e\left(\frac{h_w}{h_e}\right)^{0.7\exp\left(-0.05M_e^2\right)}$$

$$F_2 = \sum_0^i\sum_0^j a_{ij}M_e^j\left(\frac{t_w}{t_e}\right)^i$$

H total enthalpy

h altitude; static enthalpy

[redacted]

L	nondimensionalizing transition length variable used in calculating Reynolds number (see eq. (1)), can be s, δ^*, θ, or some other length variable
l	nondimensionalizing constant length used in calculating Reynolds number (see eq. (1)), can be D, 1 meter, model length, or some other constant length
M	Mach number
N	exponent for N-power-law profile, $\frac{u}{u_e} = \left(\frac{y}{\delta}\right)^{1/N}$
$N_{Pr,e}$	effective Prandtl number
n	power for unit Reynolds number
R	local unit Reynolds number, $\frac{\rho_e u_e}{\mu_e}$
R_s	local Reynolds number based on surface distance from stagnation point, $\frac{\rho_e u_e}{\mu_e} s$
R_{s_t}	local Reynolds number based on surface distance to transition, $\frac{\rho_e u_e}{\mu_e} s_t$
R_∞	free-stream unit Reynolds number
$R_{\delta_t^*}$	local transition Reynolds number based on approximate δ_t^* (see ref. 12)
r_n	nose radius
s	surface distance from stagnation point
s_t	surface distance from stagnation point to beginning of transition
t	time
$t_e = \frac{h_e}{H_e}$	
$t_w = \frac{h_w}{H_e}$	
u	local velocity

[redacted]

V_∞	free-stream velocity
x_t	axial distance to transition from virtual origin of vehicle
y	distance normal to body surface
α	mean angle of attack of vehicle at center of gravity
α_R	exponent in modified Crocco relation, $\frac{H - H_w}{H_e - H_w} = \left(\frac{u}{u_e}\right)^{\alpha_R}$
β	mean angle of yaw at center of gravity
δ	boundary-layer thickness
δ^*	displacement thickness
δ_t^*	approximate displacement thickness defined in reference 12
θ	momentum thickness
θ_c	cone half-angle
$\theta_{c,eff}$	effective cone angle used to obtain surface pressures by tangent-cone theory
θ_s	cone half-angle for which shock shape was obtained
μ	coefficient of viscosity
ρ	density
φ	azimuthal angle for cylindrical coordinate system

Subscripts:

E	reference conditions
e	local conditions at edge of boundary layer
w	wall conditions

FLIGHT VEHICLE AND TRAJECTORY

Description of Vehicle

The Reentry F flight vehicle, shown in figure 1, was a 5° half-angle cone 3.962 m (156 in.) long with an initial nose radius of 2.54 mm (0.10 in.). Except for the graphite nose, the vehicle was constructed from several truncated beryllium conical shells, 1.524 cm (0.6 in.) thick, bolted together to form a smooth external surface. (See ref. 6.) The nose of the vehicle back to station 21.59 cm (8.5 in.) was constructed from graphite to withstand the severe heating near the apex. This nose piece had an initial cone half-angle of 5.3833°. This change in cone angle resulted in a 1.016-mm (0.040-in.) rearward-facing step at the graphite-beryllium junction, which prevented a forward-facing step during the data acquisition period. A gap was also provided at the graphite-beryllium junction to allow for thermal expansion of the outer graphite shell of the nose. This gap tended to close during the data period. (See ref. 6 for construction details of the nose.) Details of the exterior geometry of the graphite nose are shown in figure 1.

Instrumentation

The vehicle was instrumented with thermocouples at 21 stations, 12 of which were located on one conical ray. (See fig. 1.) The ray with the 12 stations is denoted as the major instrumentation ray, or simply the major ray. The calculations presented herein are applied mainly to this ray. A more detailed description of the Reentry F instrumentation can be obtained from reference 6.

Trajectory and Vehicle Motion

The vehicle was launched from the NASA Wallops Station on a modified Scout vehicle. The launch operation and trajectory are described in reference 6. The prime data acquisition period occurred over the altitude range from about 36.58 to 18.29 km (120 000 to 60 000 ft). However, the body motions were such that below about 27.43 km (90 000 ft) the trim angle of attack increased, with the major thermocouple ray being continuously located on the leeward side of the body. (See ref. 7 and figs. 2 and 3.) Consequently, the temperatures of the beryllium shell were higher along the ray opposite from the major ray, and as a result, some axial distortion or bending of the vehicle occurred. The analysis of this thermal distortion is given in reference 10.

The mean trim angle of attack, as measured from the axis of symmetry of the undeformed vehicle, never exceeded 0.75° during the prime data acquisition period. (See fig. 2.) Locally, however, thermal distortion (ref. 10) increased or decreased the local inclination angle with respect to the free-stream velocity vector. For example, at 18.29 km (60 000 ft) altitude with a trim angle of attack of 0.75°, thermal distortion increased the local angle of attack at the most forward thermocouple station on the main

ray to 1.55°. This angle of attack is rather large for a 5° cone; however, it occurred only at the most forward station at the end of the useful data period and had a negligible effect on the main objective of obtaining transitional and turbulent heating data.

Although the main ray was predominantly leeward below about 25.91 km (85 000 ft) altitude, this ray was not the most leeward ray, but was about 10° from the most leeward ray. This circumferential displacement could have some influence on the local heating rates and the variation of transition with angle of attack. The possible influence of angle of attack and roll angle on boundary-layer transition will be discussed in a subsequent section in which ground-facility test data are described.

METHODS FOR SOLVING BOUNDARY-LAYER EQUATIONS WITH VARIABLE EDGE ENTROPY

The effects of nose bluntness on boundary-layer edge conditions were first discussed in reference 13. Subsequently, several methods were developed for calculating these effects for laminar, transitional, and turbulent boundary layers. (See refs. 14 and 15, for example.) In reference 14 the problems associated with matching the viscid and inviscid portions of the flow were noted. However, a recent paper (ref. 16) compared a boundary-layer method including variable-entropy effects with results from a more exact viscous-shock-layer method and found excellent agreement between the two methods. Therefore, one of the possible limitations of conventional boundary-layer variable-entropy methods has been shown to be minor.

Laminar Boundary Layer

A description of the present method used to account for the effect of variable entropy at the outer edge of the laminar boundary layer for an ideal gas is presented in reference 17. A brief review of this method and a description of its extension to include the effects of a real gas in thermodynamic equilibrium will be presented.

In reference 17 the similar boundary-layer equations were solved numerically, and an iterative procedure was used to determine the external inviscid flow condition. In this procedure the mass flow in the boundary layer at a given station for each iteration is equated to the free-stream mass flow through a portion of the bow shock. For the first iteration, the constant value of normal-shock entropy is used. For a known shock shape, it is then possible to locate the coordinate, on the shock, of the streamline that enters the boundary layer at the selected body station. The shock shape and entropy downstream of the shock were obtained from conventional inviscid flow-field calculations. (See refs. 18 and 19.) The gas with this entropy and total enthalpy (determined from known flight velocity and static enthalpy) is expanded isentropically to the static pressure at the selected

body station. The static pressure at the edge of the boundary layer was obtained by the method of references 18 and 19. The new values for the fluid conditions exterior to the boundary layer are used in the next iteration. The boundary-layer equations are solved again, and a new set of edge conditions are determined by the use of the mass balance noted above. This iteration procedure continues until suitable convergence to a specified external flow property results. For the present application, the convergence criterion was a 1-percent (or less) change in the external velocity.

Tables of the fluid properties, ρ/ρ_E, $\rho\mu/\rho_E\mu_E$, and $N_{Pr,e}$ used in reference 20 for the solution of the boundary-layer equations, were extended (by use of refs. 21 and 22) to include the variation of these properties with local pressure. These tables were used for the solution of the boundary-layer equations, and they were also used to obtain fluid properties for calculating Reynolds and Stanton numbers. The acoustic velocity, including the effect of pressure, was obtained from reference 21.

Transitional and Turbulent Boundary Layer

A description of the method for calculating the real-gas flow properties at the edge of the turbulent boundary layer, including the effects of variable entropy, is presented in reference 15. A brief description of the main features of the method is as follows: The momentum integral equation, modified for variable entropy, is integrated by using the Van Driest II skin-friction relation given in reference 23. The boundary-layer velocity profiles are determined from a correlation of N with a parameter defined in reference 15 and the density profiles are obtained from a modified form of the Crocco enthalpy-velocity relationship. Heat transfer is calculated from an empirical correlation of the Reynolds analogy factor as a function of the ratio of wall to total enthalpy. (See refs. 24 and 25.) The properties of air in thermodynamic equilibrium were obtained from a computer subroutine described in references 18 and 19 and the Prandtl number from reference 22.

In the transition region the skin-friction coefficient and the velocity-profile exponent N were assumed to vary with surface distance as hyperbolic tangent functions from a laminar value at the start of transition to a turbulent value at the end of transition. At the start of transition, the entropy at the edge of the boundary layer was matched with that from the laminar-boundary-layer calculation described previously. In addition, the boundary-layer velocity and total-enthalpy profiles were matched as closely as possible to laminar values by adjusting N and α_R (ref. 15). This procedure resulted in reasonably well matched values of the boundary-layer thickness and boundary-layer integral quantities at the beginning of transition.

The general method of solution is iterative, in which repeated calculations from the beginning of transition to the end of the body are carried out until the change in velocity

at the edge of boundary layer from one iteration to the next falls within the convergence limits. The convergence criterion is the same as that used for laminar flow, that is, a change in velocity of less than 1 percent between iterations.

DISCUSSION OF RESULTS

Boundary-Layer Edge Conditions

The boundary-layer edge conditions were calculated for the flight conditions listed in table I. These flight conditions represent (1) the most probable nose radii (ref. 8) (the nose radii presented in ref. 8 are close to the nose radii used in the calculations of the edge conditions), (2) the mean trim angle of attack (ref. 7), (3) vehicle deformation (ref. 10), and (4) the location of the beginning and end of transition (ref. 5). The angle of attack for 25.91 km (85 000 ft) and above, given as zero in table I, was actually finite but was so small that the assumption of zero angle of attack could be made with a negligible effect on the boundary-layer edge conditions. The effect of vehicle deformation on the local angle of attack was very small down to altitudes of 21.34 km (70 000 ft) and was not considered except at 18.29 km (60 000 ft), where two cases were computed. The first case was calculated for the mean trim angle of attack of the undeformed vehicle. This case, with no deformation, is believed to represent the vehicle attitude for that part of the body with a turbulent boundary layer since the body bending in these areas is small. The second case at 18.29 km (60 000 ft) included the effect of angle of attack and body bending by assuming that the representative angle of attack on the forward part of the body is the sum of the mean angle of attack and the angle due to thermal deformation in the area of the forward measuring station. This case is believed to represent the local attitude of the vehicle at the beginning of transition which occurred near the 40.6-cm (16-in.) station at this altitude.

The calculated edge conditions R_s, M_e, t_e, and t_w are presented in figures 4, 5, 6, and 7, respectively. The edge conditions for the laminar portion of the boundary layer were calculated to the 3.658-m (144-in.) station for all altitudes. The curves representing the laminar conditions in figures 4 to 7 are dashed downstream of the beginning of transition. Sharp-cone conditions are represented by a dash-dot curve for conditions that vary with surface distance and by an arrow for values that are constant.

A modified tangent-cone approximation was used to obtain inviscid flow properties at the edge of the boundary layer at angle of attack. Presumably, the small angles of attack experienced by the vehicle would make this approach reasonable. The method consisted of solving the variable-entropy boundary-layer equations for a cone with a pressure distribution equal to that of the basic 5° cone plus or minus the trim angle of attack. The shock shape used, however, was for a 5° cone at zero angle of attack. This

procedure appeared justified on the basis of results obtained from linear perturbation methods. (See ref. 26.)

In figures 4 and 5 the variable-entropy edge conditions often overshoot the sharp-cone values. This overshoot is caused by the overexpansion around the blunt nose of the cone, which results in a value of entropy along the shock that is below the sharp-cone value. However, a short distance downstream from the overexpansion, the entropy at the shock approaches the sharp-cone values and then the edge conditions approach the sharp-cone values.

From figures 4 and 5 it can be seen that the Reynolds and Mach numbers at the edge of the turbulent boundary layer were very near sharp-cone values. The Mach number was essentially constant, with a value of about 14.6, from the end of transition to the last measuring station. The wall-to-total enthalpy ratio (fig. 7) was essentially constant, with values ranging from about 0.03 to 0.05, over the vehicle where the boundary layer was turbulent. The velocity of the vehicle was almost constant over the altitudes where turbulent flow was obtained; therefore, the total enthalpy was nearly constant and equal to about 18 MJ/kg (8000 Btu/lb). Thus, the only boundary-layer edge fluid property which varied significantly for the turbulent portion of the boundary layer was the local Reynolds number. This varied from a minimum of 94×10^6 at 25.91 km (85 000 ft) altitude to a maximum of 320×10^6 at 18.29 km (60 000 ft) altitude. These results, therefore, indicate achievement of the major goal of the flight experiment – namely, to obtain turbulent heating rates at high Mach number, high total enthalpy, and low wall-to-total enthalpy ratios.

The boundary-layer edge conditions for the laminar and transitional regions can be significantly different from those for a sharp cone. For example, the Reynolds number for the blunt cone at 36.58 km (120 000 ft) altitude is about a factor of 10 less than the sharp-cone values at $s \approx 12.7$ cm (5 in.). This difference increases about two orders of magnitude at 18.29 km (60 000 ft). In addition, the local Mach number at this location is also reduced by a factor of two or three.

The bluntness effects on the laminar boundary-layer edge conditions are small in the downstream portion of the cone. In fact, the calculated laminar edge conditions approach the sharp-cone values near the end of the vehicle for all altitudes.

These large variations of edge conditions with altitude and distance along the body strongly influence the local Reynolds numbers and the local Mach numbers at transition. For example, the transition Reynolds numbers at the beginning of transition varied from a maximum of 65.6×10^6 at 24.38 km (80 000 ft) to a minimum of 0.81×10^6 at 18.29 km (60 000 ft). The corresponding Mach numbers were 14.43 and 5.55. The highest Mach number at the beginning of transition was 15.1, which occurred at 30.48 km (100 000 ft) altitude with the location of transition near the rear of the vehicle.

Transition Data

Reentry F data.- The transition Reynolds number data from table I are plotted as a function of unit Reynolds number in figure 8. At 30.48 km (100 000 ft) the transition Reynolds number is about 43×10^6 with a unit Reynolds number of 15.1×10^6 per meter (4.6×10^6 per foot). At 24.38 km (80 000 ft) the transition and unit Reynolds numbers increase to about 65.6×10^6 and 33×10^6 per meter (10.05×10^6 per foot), respectively. Below 24.38 km (80 000 ft) the transition and unit Reynolds numbers decrease and at 18.29 km (60 000 ft) are 0.81×10^6 and 1.94×10^6 per meter (0.59×10^6 per foot), respectively. In figure 9 the transition Reynolds number is presented as a function of local Mach number. The maximum Mach number for which transition data were obtained was 15.1 at 30.48 km (100 000 ft) altitude. Here the Reynolds number was about 43×10^6. As the altitude decreased, the transition Reynolds number first increased and then decreased while the local Mach number decreased. The maximum transition Reynolds number is obtained at a Mach number of about 14.43. Figures 8 and 9 should only be used to indicate the range of transition Reynolds number, unit Reynolds number, and Mach number for the Reentry F data, since only a few of the parameters that can influence transition Reynolds number were constant over the trajectory.

Data points from Reentry F for the beginning and end of transition (x_t) for intervals of not more than every 609.6 m (2000 ft) are shown in figure 10. These values of x_t were obtained from reference 5 from experimental measurements of heating plotted against axial distance for a given altitude. The edge conditions for the x_t locations were found from cross plots made from figures 4 to 7, in which edge conditions were plotted against altitude for a given x_t location. These edge conditions and transition distance were then used in determining transition correlating parameters.

Correlations of Reentry F data.- In reference 12 correlations of transition data were obtained from over 700 data points from flight and ground tests. The flight data were limited to sharp cones at small angles of attack ($\alpha \approx 0^{\circ}$) with local Mach numbers ranging from 3 to 12. The correlations were obtained from a statistical, parametric study, by use of a large computer program which considered the combined effects of unit Reynolds number, Mach number, and boundary-layer wall-to-edge enthalpy ratio.

Correlations of the Reentry F data by using two correlating parameters, $\log_{10}\left[\frac{R_{s_t}}{(R_l)^{0.65}}\right]$ and $\log_{10}\left[\frac{R_{\delta_t^*}}{(R_l)^{0.225}}\right]$ as functions of F_1, similar to those of reference 12, are shown in figure 11. Both correlating parameters indicate a linear variation with F_1, and both parameters appear to correlate the data equally well. The hooklike variation of R_{s_t} with R and M_e, which is noted for the high-altitude data in figures 8 and 9, is almost eliminated by using the correlating parameters in figure 11. The results

in figure 11 suggest an influence of both local unit Reynolds number and Mach number on the transition data since the wall-to-total enthalpy ratio was essentially constant over the altitude range where the plots in figures 8 and 9 had the hooklike variation.

A refinement and extension of the method of obtaining the transition correlations presented in reference 12 is described in part in reference 27. The general objective of this new method is a further reduction of the standard deviation from least-squares curve fits of the correlated data. This second method was formulated by assuming that the parameters which determine the laminar-boundary-layer profile have a strong influence on the stability of the laminar boundary layer and its transition to turbulent flow. For a sharp cone with no mass transfer from the wall, the major parameters which control the mean laminar profile are M_e and t_w. In addition, the local unit Reynolds number must also be considered as a parameter in view of results reported in reference 12. The total enthalpy and pressure level can have some influence on the laminar profiles; however, their influence on transition is expected to be small. As a result of such reasoning plus the insight gained from past experience, the following form for a correlation was assumed (ref. 27):

$$\log_{10} \frac{R_L}{(R_l)^n} = \sum_0^i \sum_0^j a_{ij} M_e{}^j \left(\frac{t_w}{t_e}\right)^i \tag{1}$$

The largest value for i and j actually used in the calculation was 2; therefore, the form of the equation should be able to account for the data with a transition reversal which occurs as a result of the lowering of the wall temperature. (The equation cannot account for a re-reversal in transition unless $i > 2$.) The parameter t_w/t_e correlated the data better and resulted in a simpler equation than t_w alone. $\left(\text{Note that } t_e = f(M_e)\right.$ for an ideal gas.$\left.\right)$ The constants for n and the matrix of a_{ij} values given in table II were determined by trial and error as described in reference 27, which used the over 700 data points from flight and ground tests from reference 12.

A correlation of the Reentry F data is shown in figure 12 by using the correlating parameters from equation (1) and the empirical coefficients from table II. (Additional coefficients for flight, ballistic-range, and wind-tunnel data can be found in ref. 27.) If there was a perfect correlation with equation (1), the data would lie along a straight line through the origin with a slope of 1, referred to as the line of perfect fit. The parameter $R_{\delta_t^*}/(R_l)^{0.3}$ (where $l = 0.3048$ m (1 ft)) correlated the data near the line of perfect fit. The $R_{s_t}/(R_l)^{0.7}$ parameter did not correlate with the line of perfect fit but did show a linear variation. Generally, a group of parameters can be found that will adequately correlate transition data from a particular experiment, as seen with the $R_{s_t}/(R_l)^{0.7}$ parameter. However, the generality of a group of parameters is increased if they correlate

data from several experiments. The transition data from free-flight tests of cones used in reference 12 and the Reentry F data have been compared in terms of the above correlation parameters.

Comparisons of Reentry F data with other flight data.- In figure 13 about 80 flight data points from reference 12 and the Reentry F data are correlated by use of the parameters $R_{s_t}/(R_l)^{0.65}$ and F_1. The standard deviation from a straight line fitted by the method of least squares for the 80 data points from reference 12 is less than 45 percent. The Reentry F data, except at the highest values of F_1 (high local Mach number), lie significantly below the linear curve. The deviation of the Reentry F data from the curve at values of F_1 less than about 6 is mainly due to the influence of nose bluntness on transition. In reference 28 the effect of bluntness and angle of attack is shown for a transition correlation of $R_{\delta_t^*}/(R_l)^{0.25}$ with M_e for both flight and wind-tunnel data. The correlation showed that for a local Mach number less than about 5 the data departed from the high Mach number linear correlation in a manner similar to the data shown in figure 13. The data that departed from the linear fit were represented by a blunt-body low Mach number $(M_e < 5)$ linear curve fit with a much higher slope than the high Mach number $(M_e > 5)$ straight line.

The data correlate better when the parameters $R_{\delta_t^*}/(R_l)^{0.225}$ and F_1 are used, as shown in figure 14. The apparent improvement of the correlation in figure 14 over that of figure 13 is caused partly by the fact that $R_{\delta_t^*} \propto \sqrt{R_s}$. Despite the indication of an improved correlation in figure 14, the standard deviation from the faired line is about 43 percent in terms of R_s. However, for this correlation the Reentry F data are in closer agreement with the other 80 data points than they were in figure 13.

The Reentry F data and other flight data used in figures 13 and 14 are also correlated by using equation (1) with the coefficients given in table II. Results in the form of $R_{s_t}/(R_l)^{0.7}$ plotted against F_2, shown in figure 15(a), indicate reasonable agreement between the Reentry F data and the other flight data, with the Reentry F data usually a little lower than most of the other flight data. For values of F_2 less than 2.0, the large scatter band is probably due to the effects of bluntness. Neither the other flight data nor the Reentry F data lie along the line of perfect agreement (dashed line). However, a straight line (solid line) was fitted to the flight data (ref. 12) by using the method of least squares. The standard deviation of all the flight data (ref. 12) from the solid line is about 42 percent. The linear fit to the flight data (ref. 12) in terms of the parameters of figure 15(a) is given by

$$\log_{10} \frac{R_{s_t}}{(R_l)^{0.7}} = A + BF_2 \tag{2}$$

where A and B are 0.282 and 1.07, respectively.

The two sets of flight data are also compared by using the parameters $R_{\delta_t^*}/(R_l)^{0.3}$ and F_2, as shown in figure 15(b). Here again, the flight data (ref. 12) do not agree with equation (1) (line of perfect agreement, dashed line). The flight data do agree with the line faired through the data to within 38 percent (solid line), and the Reentry F data agree well with the faired curve. The equation for the faired curve is

$$\log_{10} \frac{R_{\delta_t^*}}{(R_l)^{0.3}} = 0.81645F_2 + 0.56591 \tag{3}$$

It is concluded that the Reentry F transition data agree well with other data in terms of appropriate correlation parameters. Hence, the Reentry F data extend the range of correlating parameters to a condition of higher local Mach number.

Wind-tunnel transition results.- It has been previously noted that the graphite nose of the Reentry F vehicle was designed with an initial rearward-facing step at the graphite-beryllium junction that prevented a forward-facing step during the data acquisition period. In addition, a gap provided at this junction allowed for thermal expansion of the outer shell of the graphite nose piece. (See fig. 1 and refs. 4 and 6.) A wind-tunnel investigation was conducted at a Mach number of 8 to determine the possible effect of this gap and step on transition.

Tests were conducted with a thin-skin metal model by use of the transient technique for measuring heating to the model. A description of the model, the facility the model was tested in, the test procedure, and the data reduction procedure are described in reference 29. Locations of the beginning and end of transition were obtained from the intersection of straight lines faired through the laminar, transitional, and turbulent portions of plots of Stanton number against Reynolds number. Four different nose configurations (ref. 29) were used in the wind-tunnel tests. A model with a smooth nose having a radius of 2.54 mm (0.10 in.) served as the reference configuration. A 0.96-scale model of the preflight Reentry F nose with the step gap shown in figure 1 was the second nose configuration tested. The third configuration tested was a 0.96 scale with a 3.56-mm (0.14-in.) forward-facing step. (At one time it was postulated that a failure of the outer shell, which would result in a forward-facing step, might explain the unusual laminar heating rates at the lower altitudes of the data acquisition period. However, after the ground test of the nose configuration was completed it was determined that the unusual laminar heating was due not to a failure of the outer shell but rather to effects of angle of attack (ref. 29).) The total length of the wind-tunnel models was 72.4 cm (28.5 in.). Therefore, when the nose radius was about 2.54 mm (0.10 in.), the test simulated only the first 72.4 cm (28.5 in.) of the Reentry F vehicle. In order to simulate the full-scale vehicle in terms of s/r_n, a fourth model with a 0.508-mm-radius (0.020-in.) nose was also tested. For a significant portion of the data acquisition period of the flight experiment, the mean

location of the main thermocouple ray was about 10° from the most leeward ray. The wind-tunnel model was therefore tested with the thermocouple ray 10° from the most windward and most leeward rays. The wind-tunnel tests, by using the various noses and 10° of roll, were performed over an angle-of-attack range from 0° to 1.5° in 0.5° increments.

The results of the wind-tunnel investigation for the location of transition s_t, using the same four models described above, are presented in figure 16 for $\alpha = 0^{\circ}$ and for the windward and leeward rays ($\alpha = 0.5^{\circ}$, 1.0°, and 1.5°). In comparison with the data from the model with the 2.54-mm (0.10-in.) nose radius, the influence of the step-gap on transition was negligible at all test Reynolds numbers and angles of attack. The forward-facing step, however, tends to move transition forward with respect to the other data at the higher angle of attack. This forward movement of transition is more pronounced on the windward ray. The effect of 10° roll on the beginning and end of transition was investigated and found to be negligible for these nose shapes at the angles of attack investigated.

The transition data for the smooth nose geometry with $r_n = 2.54$ and 0.508 mm (0.100 and 0.020 in.) and $\varphi = 0^{\circ}$ are plotted in figure 17 as a function of angle of attack for various values of the free-stream unit Reynolds number. There is much disagreement between existing data as to the influence of angle of attack on the location of the beginning of transition. Some data indicate that with respect to $\alpha = 0^{\circ}$ data, the location of transition moves rearward on the windward surface and forward on the leeward surface (ref. 30); other data indicate that transition moves forward on both the windward and leeward surfaces but at different rates with angle of attack. These apparently conflicting results may depend on nose radius, angle of attack, unit Reynolds number, Mach number, cone angle, and test facility. The results of figure 17(a) indicate that for the large nose radius $\left(r_n = 2.54 \text{ mm } (0.100 \text{ in.})\right)$ transition moves forward with an increase in angle of attack for both the windward and leeward surfaces over the range of unit Reynolds numbers tested. In addition, for a given unit Reynolds number, the leeward surface has an onset of transition closer to the nose than the windward surface. In figure 17(b) data for a small nose radius $\left(r_n = 0.508 \text{ mm } (0.020 \text{ in.})\right)$ over the same range of unit Reynolds numbers show the same trend for the leeward surface as figure 17(a). However, for the windward surface, the four highest unit Reynolds numbers show a nearly constant location for the onset of transition, whereas for the three lowest unit Reynolds numbers, a rearward movement of the onset of transition is shown. The conflicting results for the movement of transition with the angle of attack on the windward surface indicate a strong dependency of the location of transition on unit Reynolds number and nose radius. The present wind-tunnel data do not agree with the trend shown by the Reentry F data (refs. 4 and 5) and found by others (ref. 31) – namely, a more forward movement of transition on the windward ray than on the leeward ray. The present wind-

tunnel data do illustrate the complexity of the transition problem on blunted cones at angle of attack and serve to emphasize the need for caution in generalizing the results of a few tests.

CONCLUSIONS

Boundary-layer edge conditions that include the effects of variable entropy have been calculated for the Reentry F flight test over a range of altitudes from 36.58 to 18.29 km (120 000 to 60 000 ft) and velocities near 6.096 km/sec (20 000 ft/sec). The geometry and vehicle attitudes used in the calculation of edge conditions were obtained from previous publications and include the effects of nose radius, angle of attack, and deformation caused by unsymmetrical heating. The transition Reynolds numbers based on these local conditions and the known locations of transition have been determined, and data have been compared and correlated with previous flight and wind-tunnel data from sharp cones at small angles of attack. The following conclusions can be made:

1. Boundary-layer edge conditions over that part of the body where fully developed turbulent boundary-layer flow was experienced were approximately constant and close to the sharp-cone values. The edge Mach number was approximately 15, and the maximum local Reynolds number was about 3×10^8.

2. Transition Reynolds numbers varied considerably during the prime data acquisition period. The maximum local transition Reynolds number was about 6.6×10^7 for a local Mach number of about 14.4 at 24.38 km (80 000 ft) altitude. The minimum transition Reynolds number was 0.8×10^6 with an edge Mach number of about 6 at 18.29 km (60 000 ft) altitude.

3. The transition Reynolds numbers for the Reentry F flight were correlated in terms of local parameters, which included the unit Reynolds number, Mach number, and the wall-to-edge enthalpy ratio. The correlations of the Reentry F data agreed well with correlations from other flight data for some correlating parameters.

4. A wind-tunnel investigation of the effects of small angles of attack on transition along the windward rays of a 5° half-angle cone shows that the movement of transition is modified considerably by unit Reynolds number and nose bluntness. The results on the leeward ray always indicate a forward movement of transition with angle of attack.

Langley Research Center,
National Aeronautics and Space Administration,
Hampton, Va., June 12, 1972.

[redacted]

REFERENCES

1. Kline, S. J.; Morkovin, M. V.; Sovran, G.; and Cockrell, D. J., eds.: Computation of Turbulent Boundary Layers – 1968 AFOSR-IFP-Stanford Conference. Vol. I – Methods, Predictions, Evaluation and Flow Structure. Stanford Univ., c.1969.
   Coles, D. E.; and Hirst, E. A., eds.: Computation of Turbulent Boundary Layers – 1968 AFOSR-IFP-Stanford Conference. Vol. II – Compiled Data. Stanford Univ., c.1969.
2. Bertram, Mitchel H., moderator: Panel and General Discussion. Compressible Turbulent Boundary Layers, NASA SP-216, 1969, pp. 547-564.
3. Beckwith, Ivan E.: Recent Advances in Research on Compressible Turbulent Boundary Layers. Analytical Methods in Aircraft Aerodynamics, NASA SP-228, 1970, pp. 355-416.
4. Rumsey, Charles B.; Carter, Howard S.; Hastings, Earl C., Jr.; Raper, James L.; and Zoby, Ernest V.: Initial Results From Flight Measurements of Turbulent Heat Transfer and Boundary-Layer Transition at Local Mach Numbers Near 15 (Reentry F). NASA TM X-1856, 1969.
5. Wright, Robert L.; and Zoby, Ernest V.: Flight Measurements of Boundary-Layer Transition on a 5° Half-Angle Cone at a Free-Stream Mach Number of 20 (Reentry F). NASA TM X-2253, 1971.
6. Carter, Howard S.; Raper, James L.; Hinson, William F.; and Morris, W. Douglas: Basic Measurements From a Turbulent-Heating Flight Experiment on a 5° Half-Angle Cone at Mach 20 (Reentry F). NASA TM X-2308, 1971.
7. Woodbury, Gerard E.; and Morris, W. Douglas: Angle-of-Attack Analysis of a Spinning Slender Cone With Aerodynamic and Mass Asymmetries (Reentry F). NASA TN D-5948, 1970.
8. Dillon, James L.: Analysis of Surface Pressure on a 5° Cone in Free Flight Near Mach 20 (Reentry F). NASA TM X-2210, 1971.
9. Howard, Floyd G.: Thermal Analysis Methods and Basic Heat-Transfer Data for a Turbulent Heating Flight Experiment at Mach 20 (Reentry F). NASA TM X-2282, 1971.
10. Alley, Vernon L., Jr.; and Guillotte, Robert J.: Postflight Analysis of Thermal Distortions of the Reentry F Spacecraft. NASA TM X-2250, 1971.
11. Zoby, Ernest V.; and Rumsey, Charles B.: Analysis of Free-Flight Laminar, Transitional, and Turbulent Heat-Transfer Results at Free-Stream Mach Numbers Near 20 (Reentry F). NASA TM X-2335, 1971.

[redacted]

[redacted]

12. Bertram, Mitchel H.; and Beckwith, Ivan E.: NASA-Langley Boundary Layer Transition Investigations. Boundary Layer Transition Study Group Meeting, William D. McCauley, ed., BSD-TR-67-213, Vol III, U.S. Air Force, Aug. 1967, pp. 18-i – 18-73. (Available from DDC as AD 384 006.)

13. Ferri, Antonio; and Libby, Paul A.: Note on an Interaction Between the Boundary Layer and the Inviscid Flow. J. Aeronaut. Sci., vol. 21, no. 2, Feb. 1954, p. 130.

14. Ferri, Antonio: Some Heat Transfer Problems in Hypersonic Flow. Aeronautics and Astronautics, Nicholas John Hoff and Walter Guido Vincenti, eds., Pergamon Press, Inc., 1960, pp. 344-377.

15. Johnson, Charles B.; and Boney, Lillian R.: A Simple Integral Method for the Calculation of Real-Gas Turbulent Boundary Layers With Variable Edge Entropy. NASA TN D-6217, 1971.

16. Mayne, A. W., Jr.; and Adams, J. C., Jr.: Streamline Swallowing by Laminar Boundary Layers in Hypersonic Flow. AEDC-TR-71-32, U.S. Air Force, Mar. 1971. (Available from DDC as AD 719 748.)

17. Stainback, P. Calvin (With appendix by P. Calvin Stainback and Kathleen C. Wicker): Effect of Unit Reynolds Number, Nose Bluntness, Angle of Attack, and Roughness on Transition on a 5° Half-Angle Cone at Mach 8. NASA TN D-4961, 1969.

18. Inouye, Mamoru; and Lomax, Harvard: Comparison of Experimental and Numerical Results for the Flow of a Perfect Gas About Blunt-Nosed Bodies. NASA TN D-1426, 1962.

19. Lomax, Harvard; and Inouye, Mamoru: Numerical Analysis of Flow Properties About Blunt Bodies Moving at Supersonic Speeds in Equilibrium Gas. NASA TR R-204, 1964.

20. Cohen, Nathaniel B.: Boundary-Layer Similar Solutions and Correlation Equations for Laminar Heat-Transfer Distribution in Equilibrium Air at Velocities up to 41,000 Feet Per Second. NASA TR R-118, 1961.

21. Neel, C. A.; and Lewis, Clark H.: Interpolations of Imperfect Air Thermodynamic Data. II. At Constant Pressure. AEDC-TDR-64-184, U.S. Air Force, Sept. 1964.

22. Hansen, C. Frederick: Approximations for the Thermodynamic and Transport Properties of High-Temperature Air. NASA TR R-50, 1959. (Supersedes NACA TN 4150.)

23. Hopkins, Edward J.; Keener, Earl R.; and Louie, Pearl T.: Direct Measurements of Turbulent Skin Friction on a Nonadiabatic Flat Plate at Mach Number 6.5 and Comparison With Eight Theories. NASA TN D-5675, 1970.

[redacted]

[redacted]

24. Wilson, Donald M.: A Correlation of Heat-Transfer and Skin-Friction Data and an Experimental Reynolds Analogy Factor for Highly Cooled Turbulent Boundary Layers at Mach 5.0. NOLTR-69-51, U.S. Navy, Mar. 5, 1969. (Available from DDC as AD 690 454.)

25. Cary, Aubrey M., Jr.: Summary of Available Information on Reynolds Analogy for Zero-Pressure-Gradient, Compressible, Turbulent-Boundary-Layer Flow. NASA TN D-5560, 1970.

26. Rakich, John V.: Numerical Calculation of Supersonic Flows of a Perfect Gas Over Bodies of Revolution at Small Angles of Yaw. NASA TN D-2390, 1964.

27. Beckwith, Ivan E.; and Bertram, Mitchel A.: A Survey of NASA Langley Studies on High-Speed Transition and the Quiet Tunnel. NASA TM X-2566, 1972.

28. Johnson, Charles B. (With appendix by George C. Ashby, Jr.): Boundary-Layer Transition and Heating Criteria Applicable to Space Shuttle Configuration From Flight and Ground Tests. Vol. I of NASA Space Shuttle Technology Conference, NASA TM X-2272, 1971, pp. 97-156.

29. Stainback, P. Calvin; Johnson, Charles B.; Boney, Lillian R.; and Wicker, Kathleen C.: A Comparison of Theoretical Predictions and Heat-Transfer Measurements for a Flight Experiment at Mach 20 (Reentry F). NASA TM X-2560, 1972.

30. Stetson, Kenneth F.; and Rushton, George H.: Shock Tunnel Investigation of Boundary-Layer Transition at M = 5.5. AIAA J., vol. 5, no. 5, May 1967, pp. 899-906.

31. Maddalon, Dal V.; and Henderson, Arthur, Jr.: Hypersonic Transition Studies on a Slender Cone at Small Angles of Attack. AIAA J., vol. 6, no. 1, Jan. 1968, pp. 176-177.

[redacted]

[redacted]

TABLE I.- TRANSITION DATA FOR REENTRY F VEHICLE

$\left[\theta_c = 5^\circ\right]$

(a) SI Units

Altitude, km	V_∞, km/sec	M_∞	r_n, mm	α, deg	$\theta_{c,eff}$, deg	Beginning of transition				End of transition		
						s_t, m	M_e	Local Reynolds number, R_{s_t}	Local unit Reynolds number, R, per meter	s_t, m	M_e	Local Reynolds number, R_{s_t}
36.58	6.03	19.25	2.896	0	5							
30.48	6.02	19.79	3.099	0	5	2.908	15.10	43.0×10^6	14.78×10^6			
27.43	6.00	20.07	3.251	0	5	2.294	14.93	53.5	23.32			
25.91	5.99	20.03	3.327	0	5	2.169	14.78	60.0	27.65	3.42	14.8	94×10^6
24.38	5.97	19.97	3.429	.140	4.860	1.986	14.43	65.6	32.97	3.117	14.85	113
22.86	5.94	19.89	3.556	.425	4.575	1.402	13.29	39.5	28.16	2.629	15.25	120
21.34	5.90	19.95	3.683	.660	4.340	1.186	11.93	29.0	24.44	2.380	15.60	140
19.81	5.86	19.97	3.835	.715	4.285	.818	9.34	10.5	12.83	2.256	15.60	168
[a] 18.29	5.80	19.95	3.988	.750	4.250	.419	5.78	1.21	2.88	2.253	15.37	203
[b] 18.29	5.80	19.95	3.988	1.55	3.45	.419	5.55	.81	1.93	2.253		

(b) U.S. Customary Units

Altitude, ft	V_∞, ft/sec	M_∞	r_n, in.	α, deg	$\theta_{c,eff}$, deg	Beginning of transition				End of transition		
						s_t, in.	M_e	Local Reynolds number, R_{s_t}	Local unit Reynolds number, R, per foot	s_t, in.	M_e	Local Reynolds number, R_{s_t}
120 000	19 786	19.25	0.114	0	5							
100 000	19 747	19.79	.122	0	5	114.5	15.10	43.0×10^6	4.507×10^6			
90 000	19 687	20.07	.128	0	5	90.3	14.93	53.5	7.110			
85 000	19 638	20.03	.131	0	5	85.4	14.78	60.0	8.43	134.8	14.8	94×10^6
80 000	19 572	19.97	.135	.140	4.860	78.2	14.43	65.6	10.05	122.7	14.85	113
75 000	19 482	19.89	.140	.425	4.575	55.2	13.29	39.5	8.585	103.5	15.25	120
70 000	19 367	19.95	.145	.660	4.340	46.7	11.93	29.0	7.45	93.7	15.60	140
65 000	19 215	19.97	.151	.715	4.285	32.2	9.34	10.5	3.912	88.8	15.60	168
[a] 60 000	19 018	19.95	.157	.750	4.250	16.5	5.78	1.21	.88	88.7	15.37	203
[b] 60 000	19 018	19.95	.157	1.55	3.45	16.5	5.55	.81	.589	88.7		

[a] Condition assumed to be most applicable for turbulent portion of boundary layer.

[b] Condition for 40.6-cm (16-in.) station and assumed to be most applicable for laminar boundary layer at beginning of transition.

[redacted]

[redacted]

TABLE II. - COEFFICIENTS[a] FOR F_2 PARAMETER BASED ON FLIGHT- AND GROUND-TEST DATA[b]

$\left[l = 0.3048 \text{ m} \quad (1 \text{ ft})\right]$

i	a_{ij} for j equal to –		
	0	1	2
$R_{s_t}/(R_l)^n$; n = 0.7			
0	1.6788	0.049553	0
1	.064804	-.0039106	0
2	-.013079	-.013260	.0015698
$R_{\delta_t^*}/(R_l)^n$; n = 0.3			
0	0.70579	0.17929	0
1	.37680	-.042345	0
2	-.11602	.024173	-.0011112

[a] Based on minimum standard deviation.

[b] Reference 12.

[redacted]

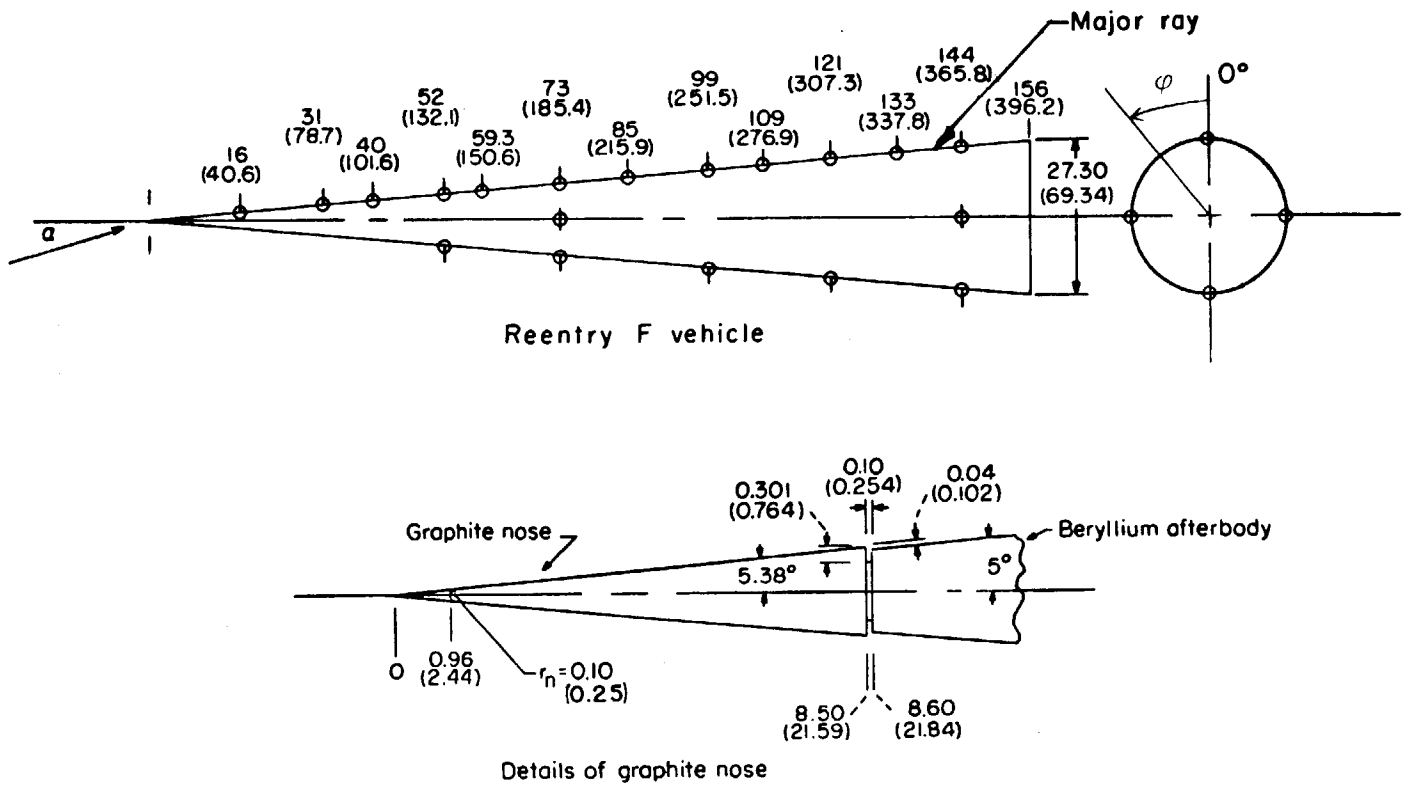

Figure 1.- Vehicle geometry and thermocouple locations. All dimensions are in inches (cm) and are for preflight condition.

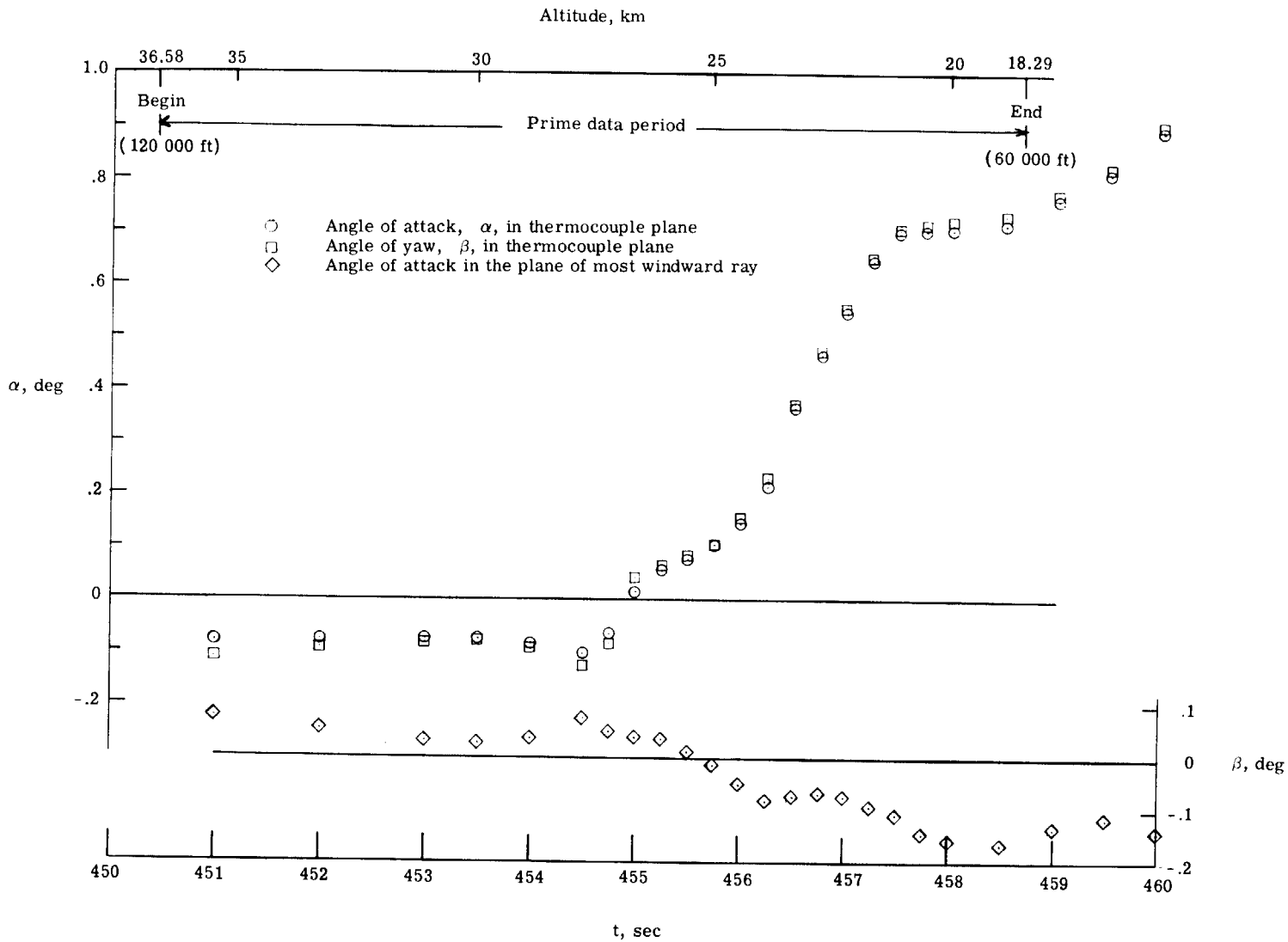

Figure 2.- Mean angle of attack and yaw of most windward ray and thermocouple plane.

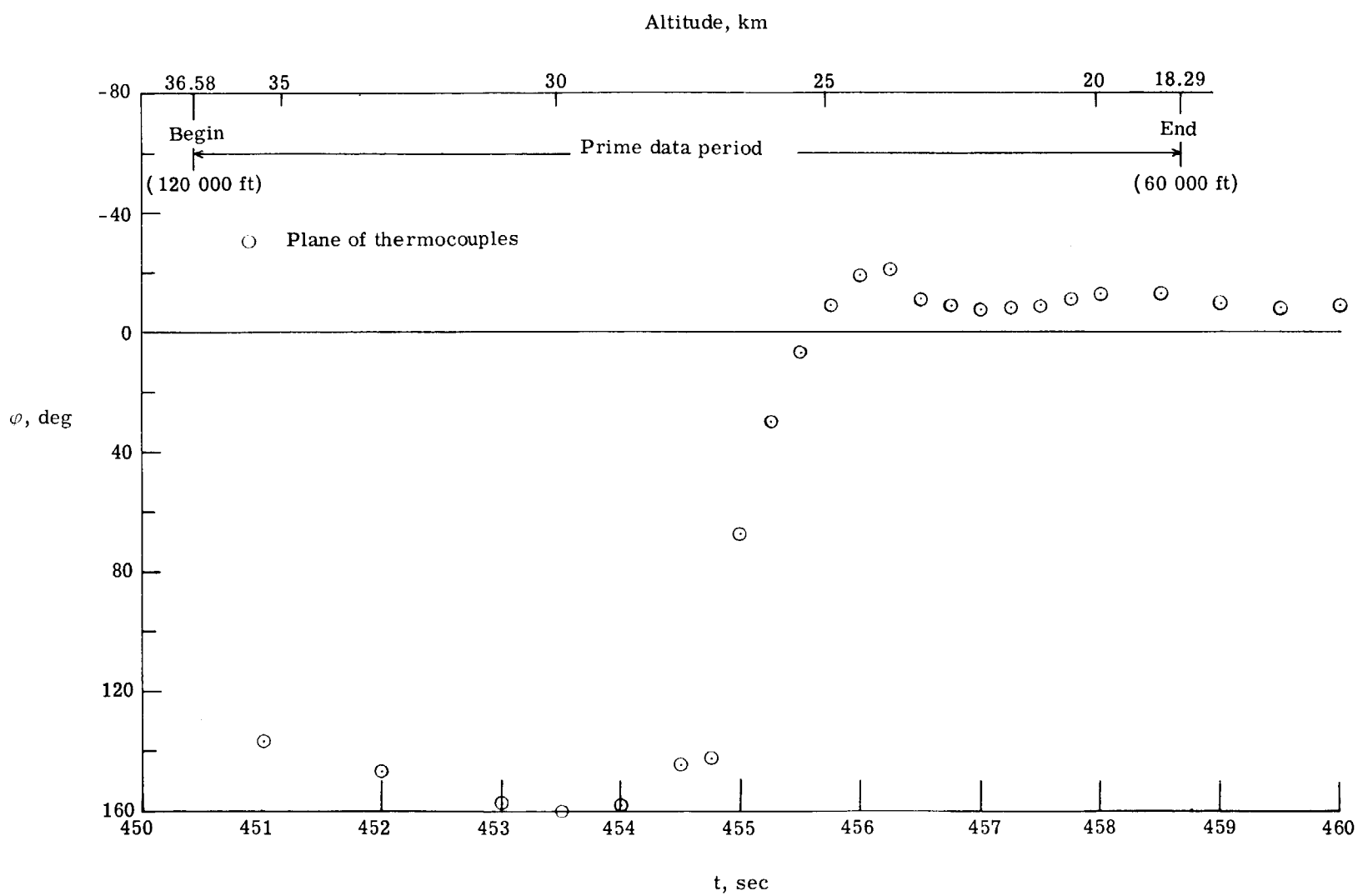

Figure 3.- Mean circumferential orientation of most leeward ray and instrumentation ray.

[redacted]

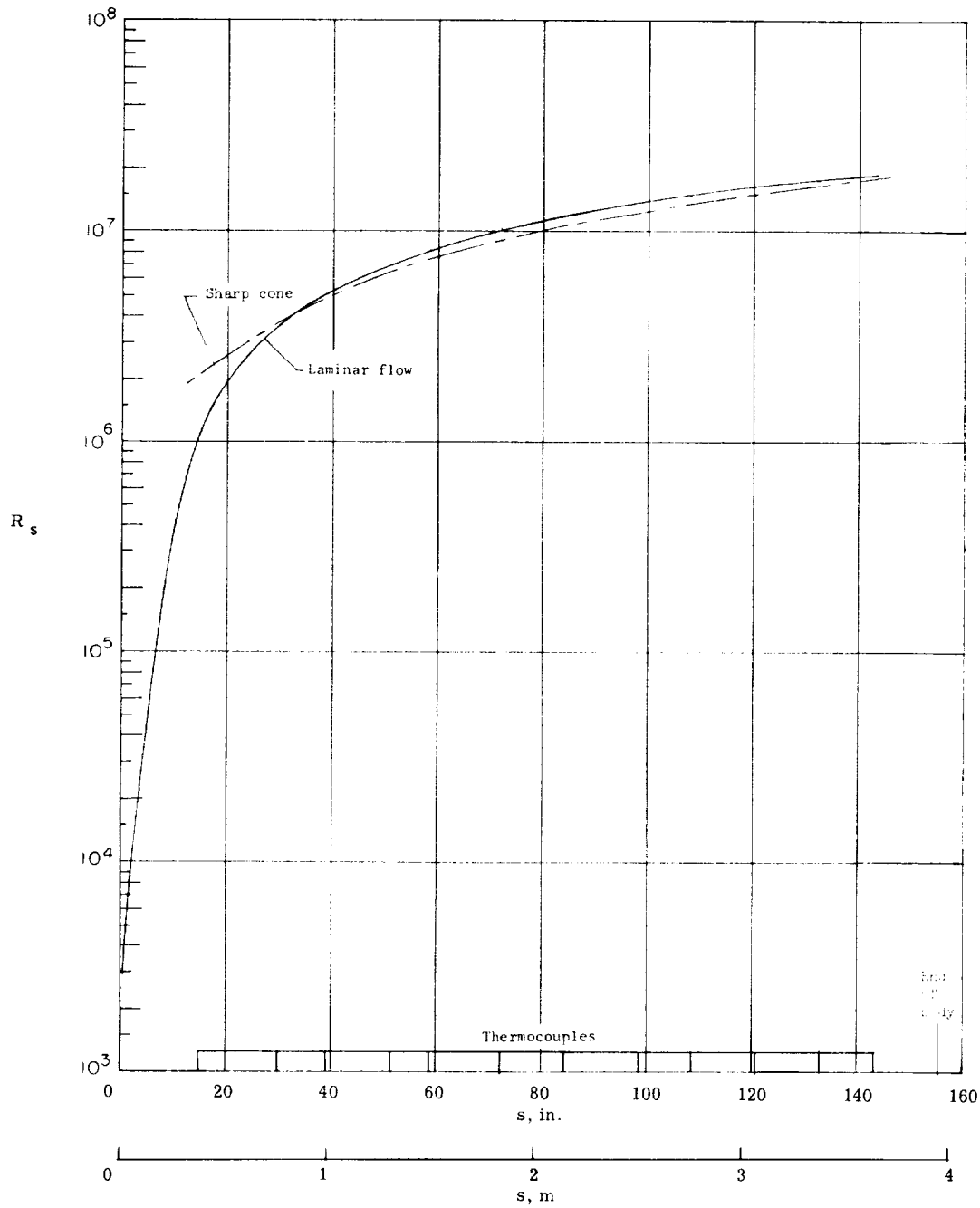

(a) h = 36.58 km (120 000 ft); V_∞ = 6.03 km/sec (19 786 ft/sec); r_n = 2.896 mm (0.114 in.); $\theta_{c,eff} = 5^\circ$.

Figure 4.- Local Reynolds number along vehicle. $\theta_s = 5^\circ$.

[redacted]

[redacted]

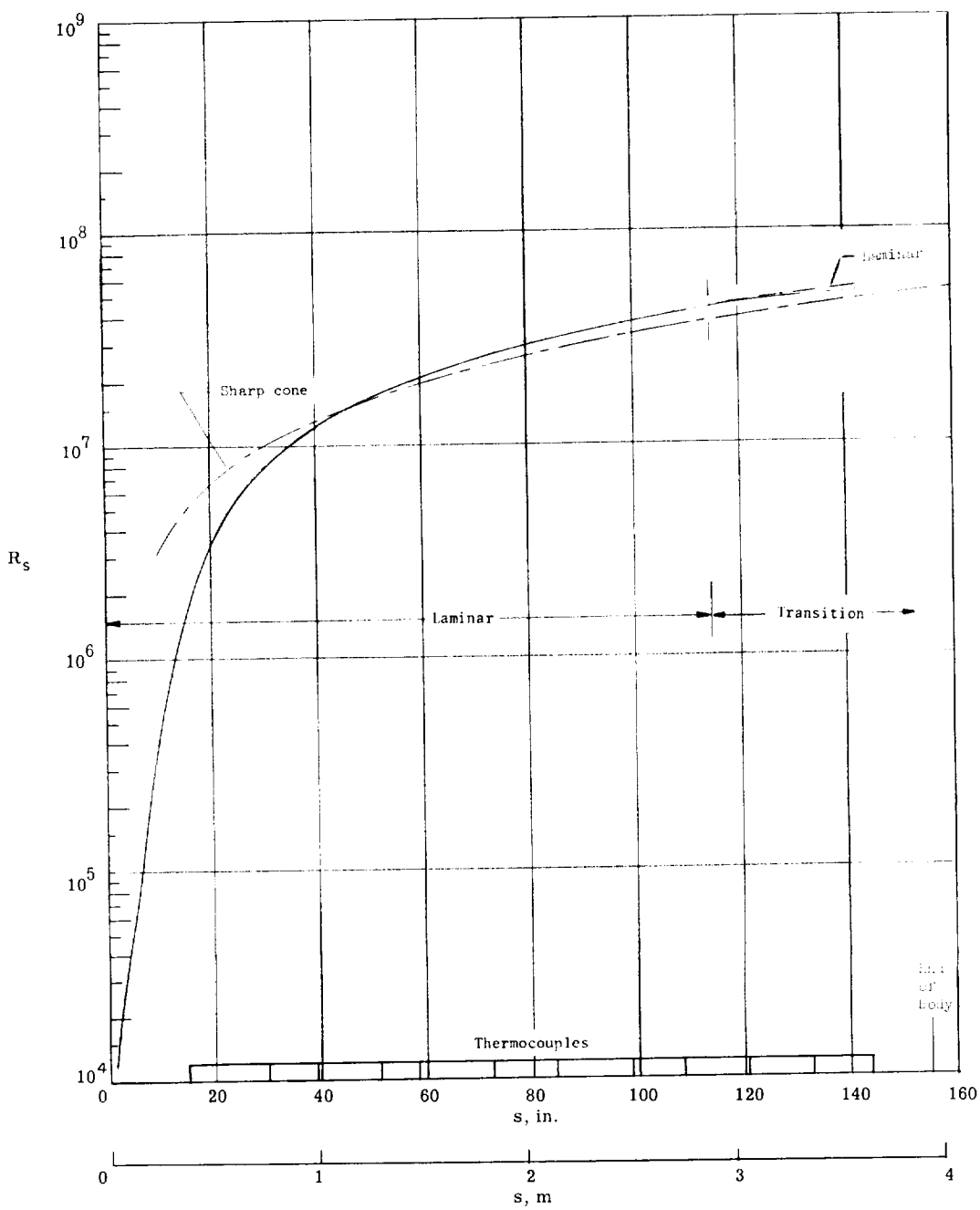

(b) h = 30.48 km (100 000 ft); V_∞ = 6.02 km/sec (19 747 ft/sec); r_n = 3.099 mm (0.122 in.); $\theta_{c,eff} = 5^o$.

Figure 4.- Continued.

[redacted]

[redacted]

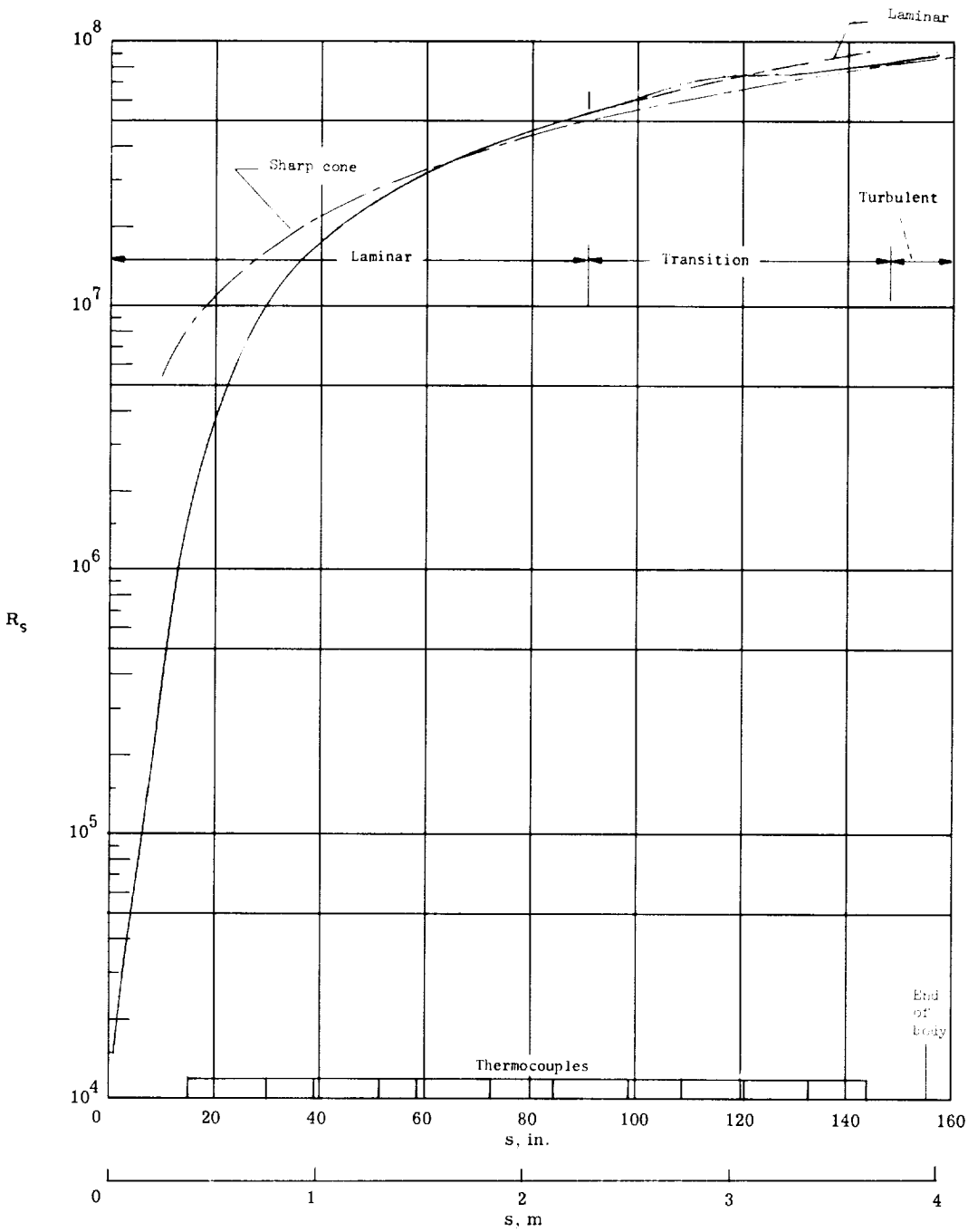

(c) h = 27.43 km (90 000 ft); V_∞ = 6.00 km/sec (19 687 ft/sec); r_n = 3.251 mm (0.128 in.); $\theta_{c,eff} = 5^\circ$.

Figure 4.- Continued.

[redacted]

[redacted]

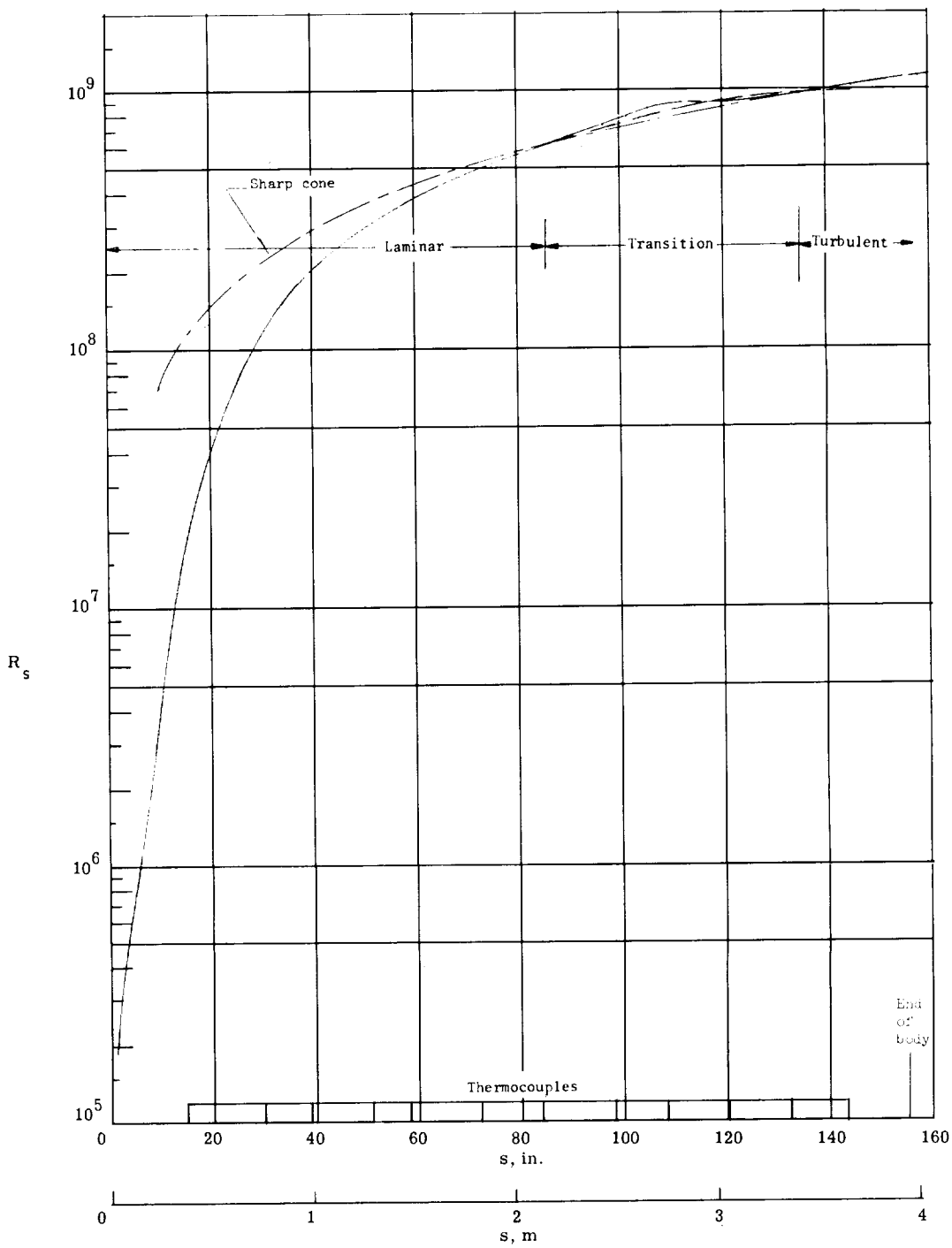

(d) h = 25.91 km (85 000 ft); V_∞ = 5.99 km/sec (19 638 ft/sec); r_n = 3.327 mm (0.131 in.); $\theta_{c,eff} = 5^o$.

Figure 4. - Continued.

[redacted]

[redacted]

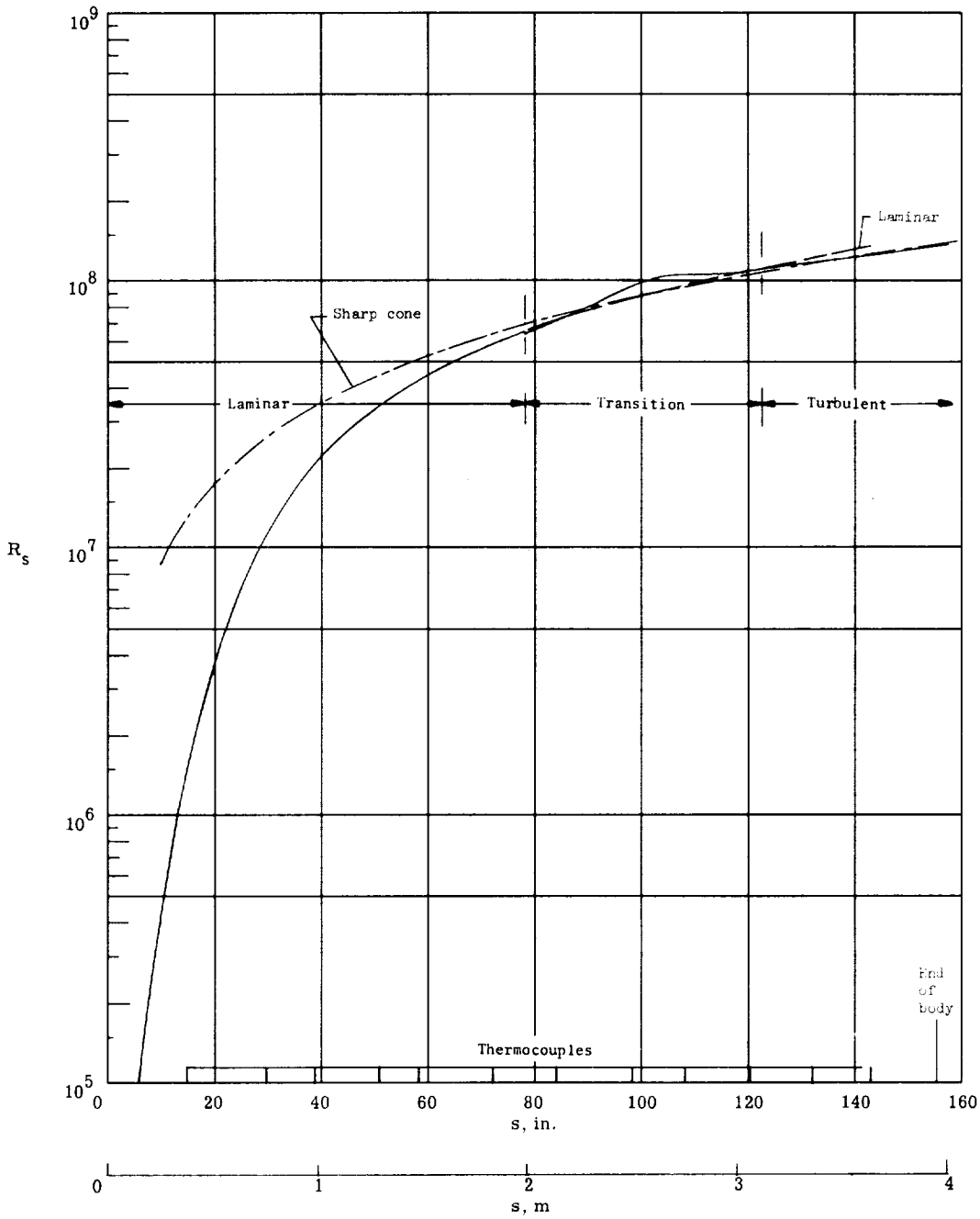

(e) h = 24.38 km (80 000 ft); V_∞ = 5.97 km/sec (19 572 ft/sec); r_n = 3.429 mm (0.135 in.); $\theta_{c,eff} = 4.860^\circ$.

Figure 4.- Continued.

[redacted]

[redacted]

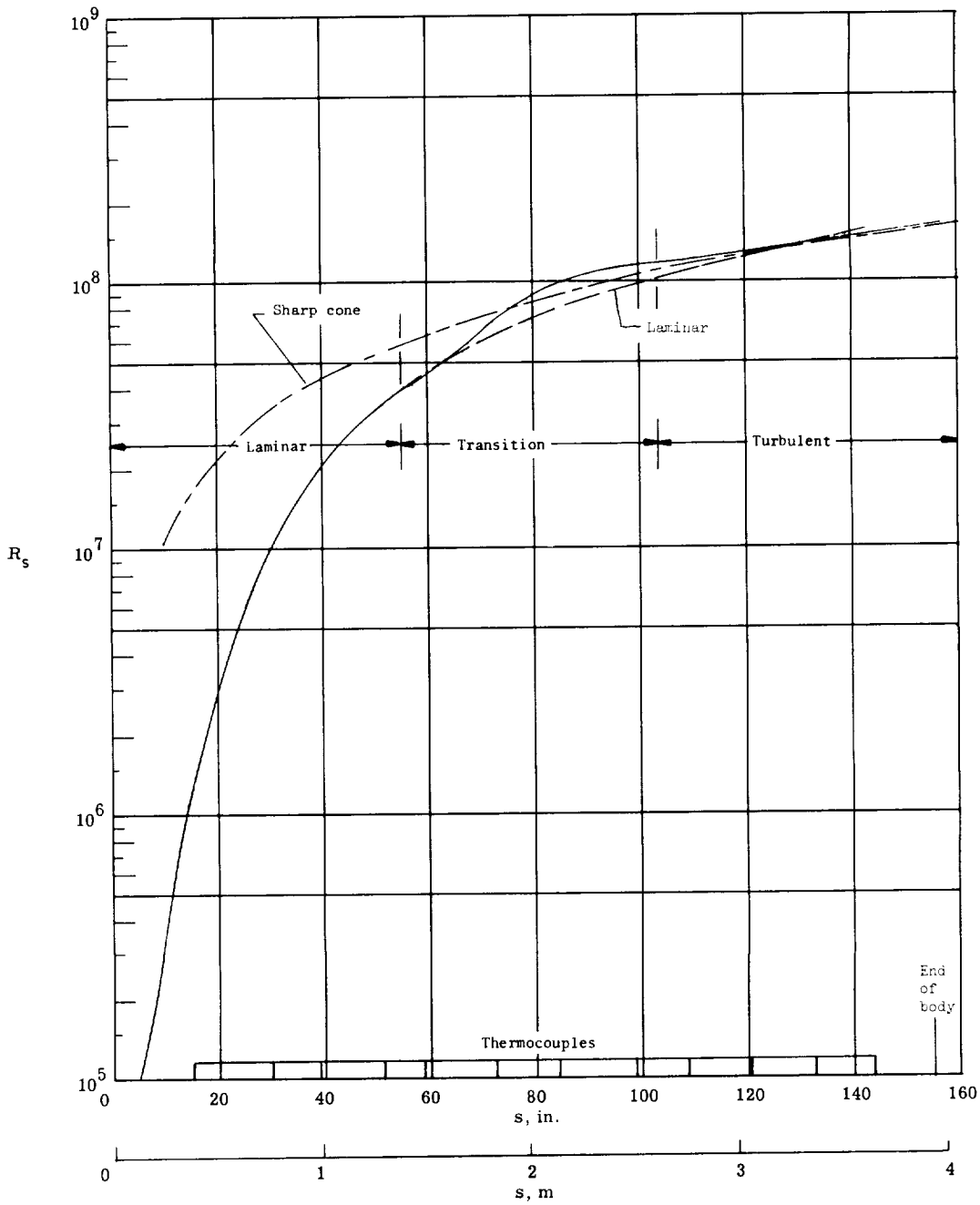

(f) h = 22.86 km (75 000 ft); V_∞ = 5.94 km/sec (19 482 ft/sec); r_n = 3.556 mm (0.140 in.); $\theta_{c,eff} = 4.575^\circ$.

Figure 4.- Continued.

[redacted]

[redacted]

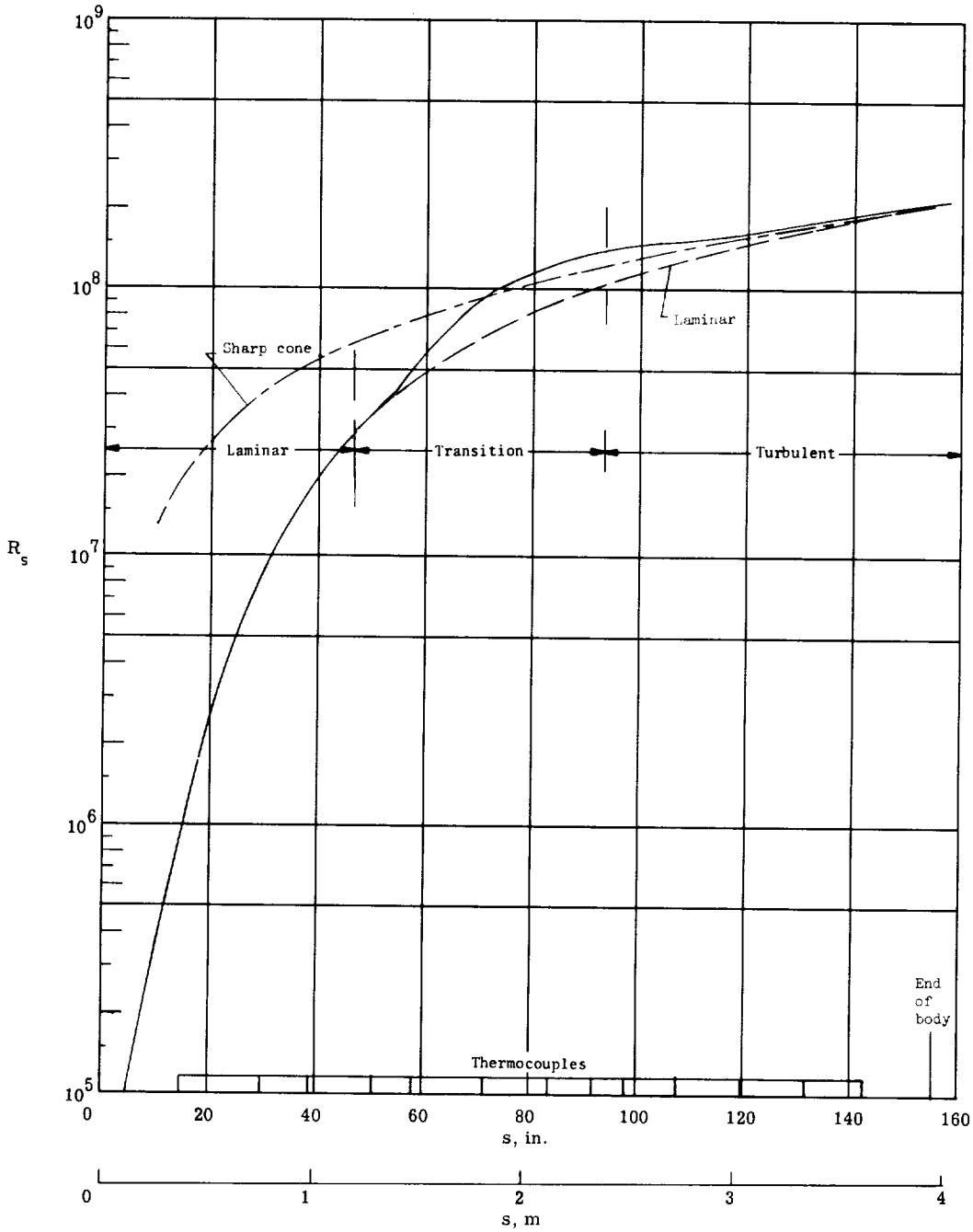

(g) h = 21.34 km (70 000 ft); V_∞ = 5.90 km/sec (19 367 ft/sec); r_n = 3.683 mm (0.145 in.); $\theta_{c,eff}$ = 4.340°.

Figure 4.- Continued.

[redacted]

[redacted]

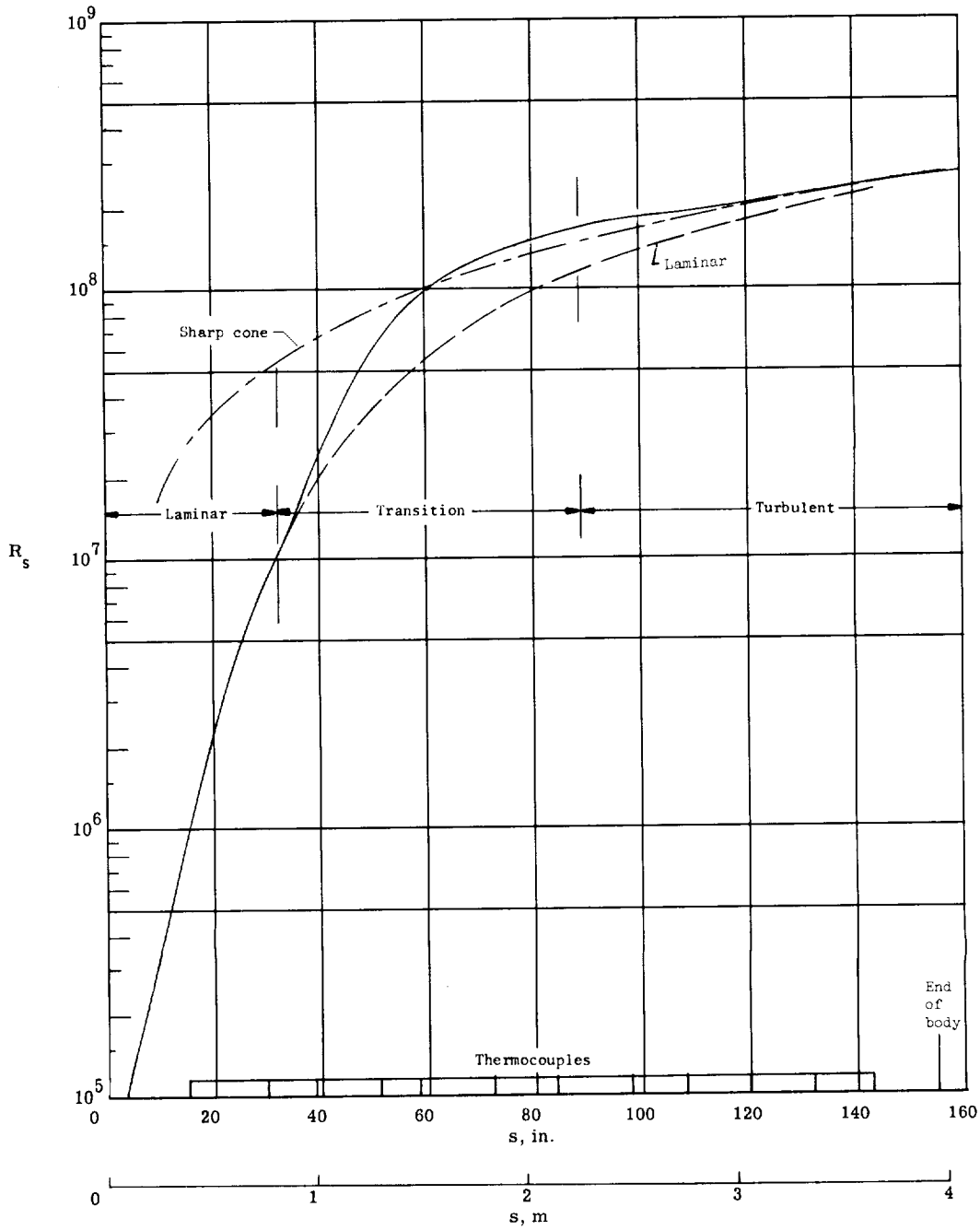

(h) h = 19.81 km (65 000 ft); V_∞ = 5.86 km/sec (19 215 ft/sec); r_n = 3.835 mm (0.151 in.); $\theta_{c,eff}$ = 4.285°.

Figure 4.- Continued.

[redacted]

[redacted]

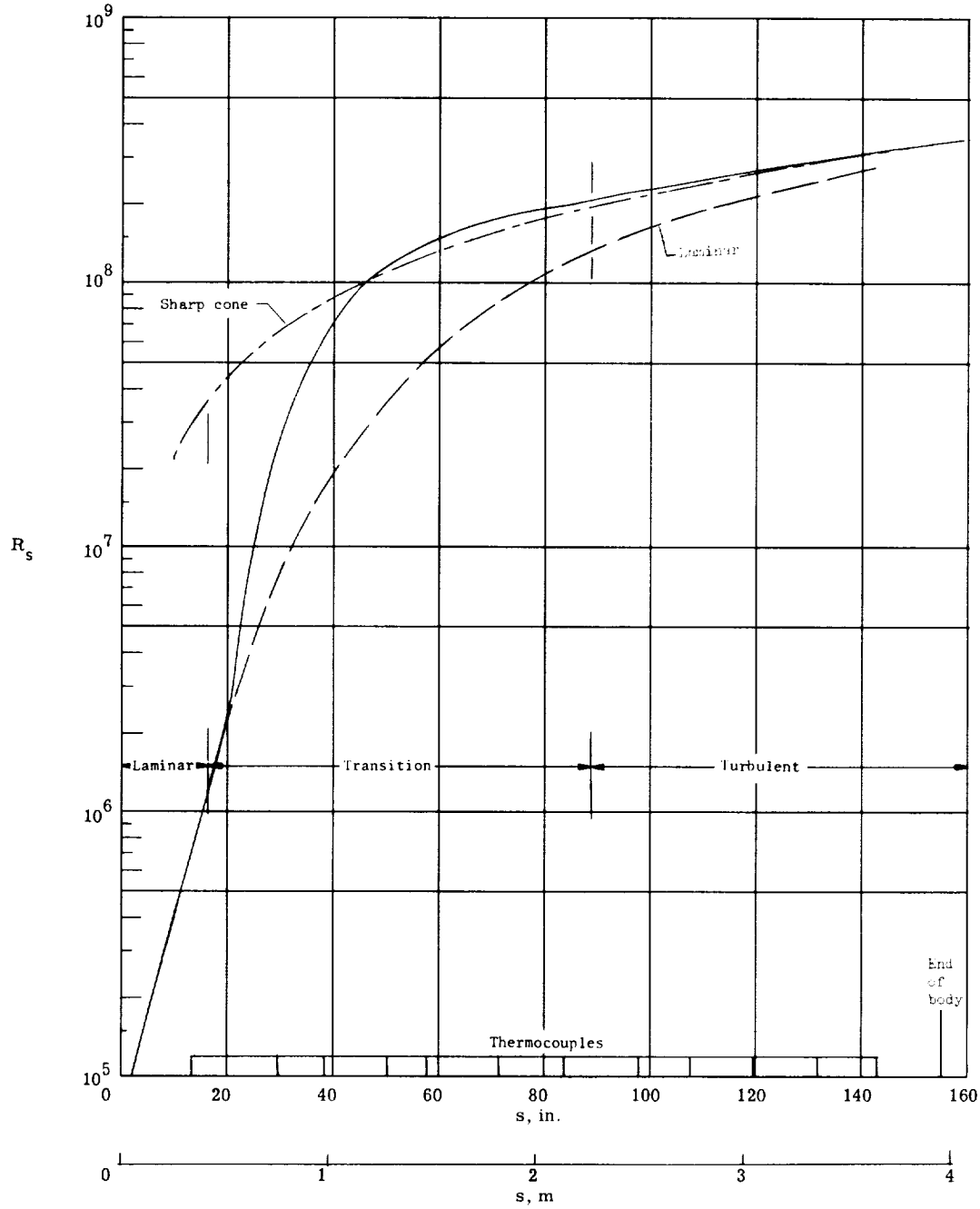

(i) h = 18.29 km (60 000 ft); V_∞ = 5.80 km/sec (19 018 ft/sec); r_n = 3.988 mm (0.157 in.); $\theta_{c,eff}$ = 4.250°.

Figure 4.- Continued.

[redacted]

[redacted]

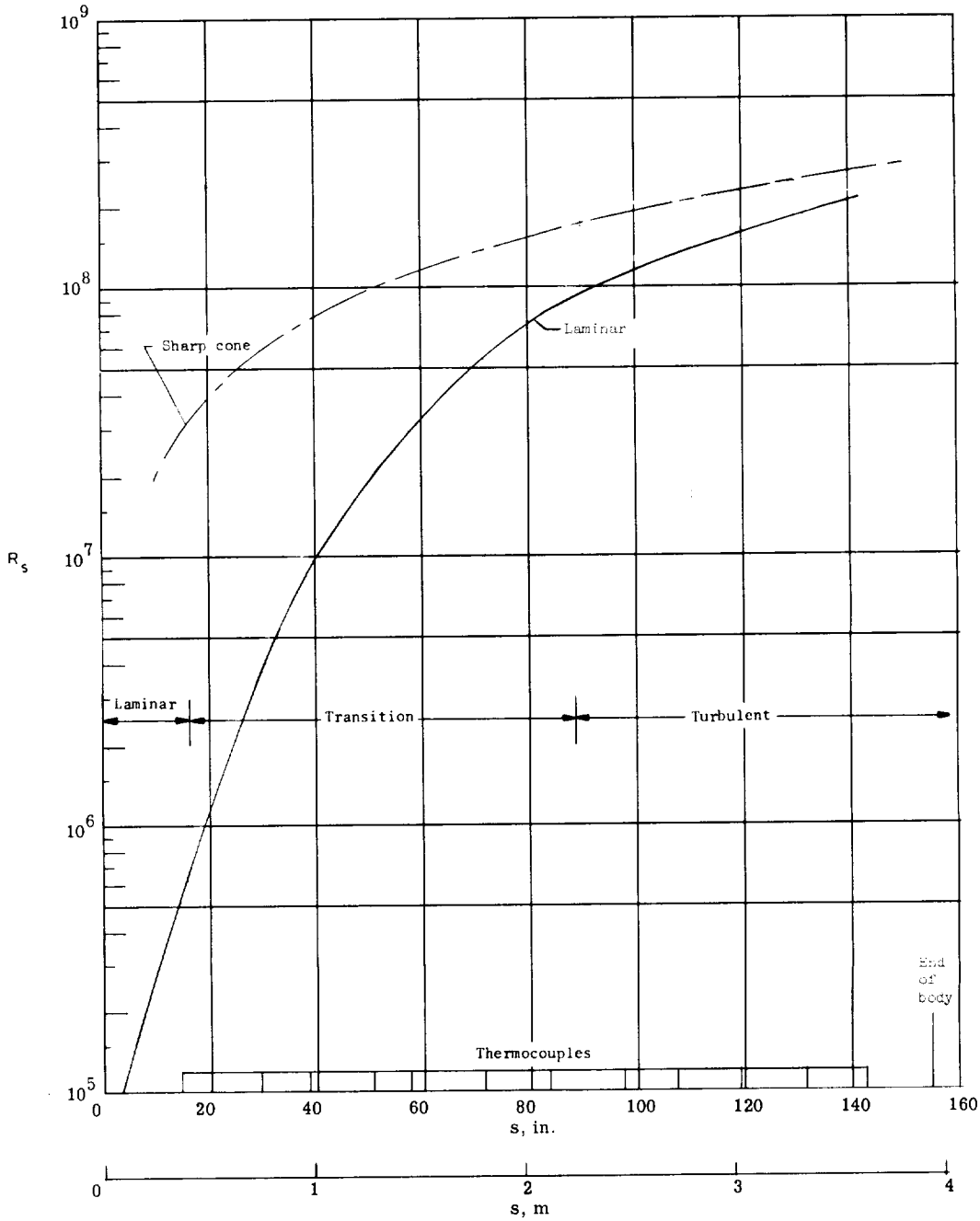

(j) h = 18.29 km (60 000 ft); V_∞ = 5.80 km/sec (19 018 ft/sec); r_n = 3.988 mm (0.157 in.); $\theta_{c,eff} = 3.45^\circ$.

Figure 4.- Concluded.

[redacted]

[redacted]

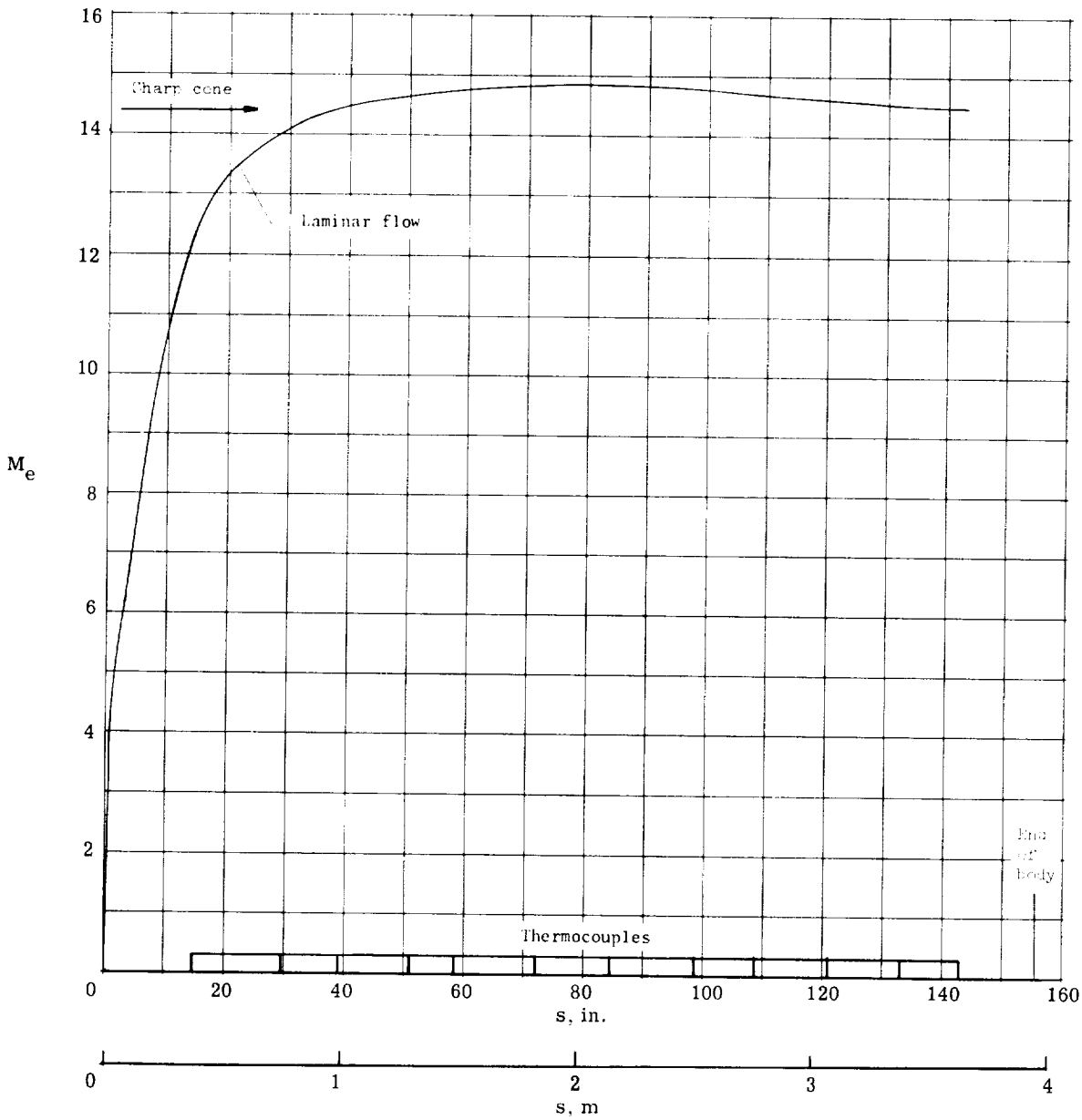

(a) h = 36.58 km (120 000 ft); V_∞ = 6.03 km/sec (19 786 ft/sec); r_n = 2.896 mm (0.114 in.); $\theta_{c,eff} = 5^o$.

Figure 5.- Local Mach number along vehicle. $\theta_s = 5^o$.

[redacted]

[redacted]

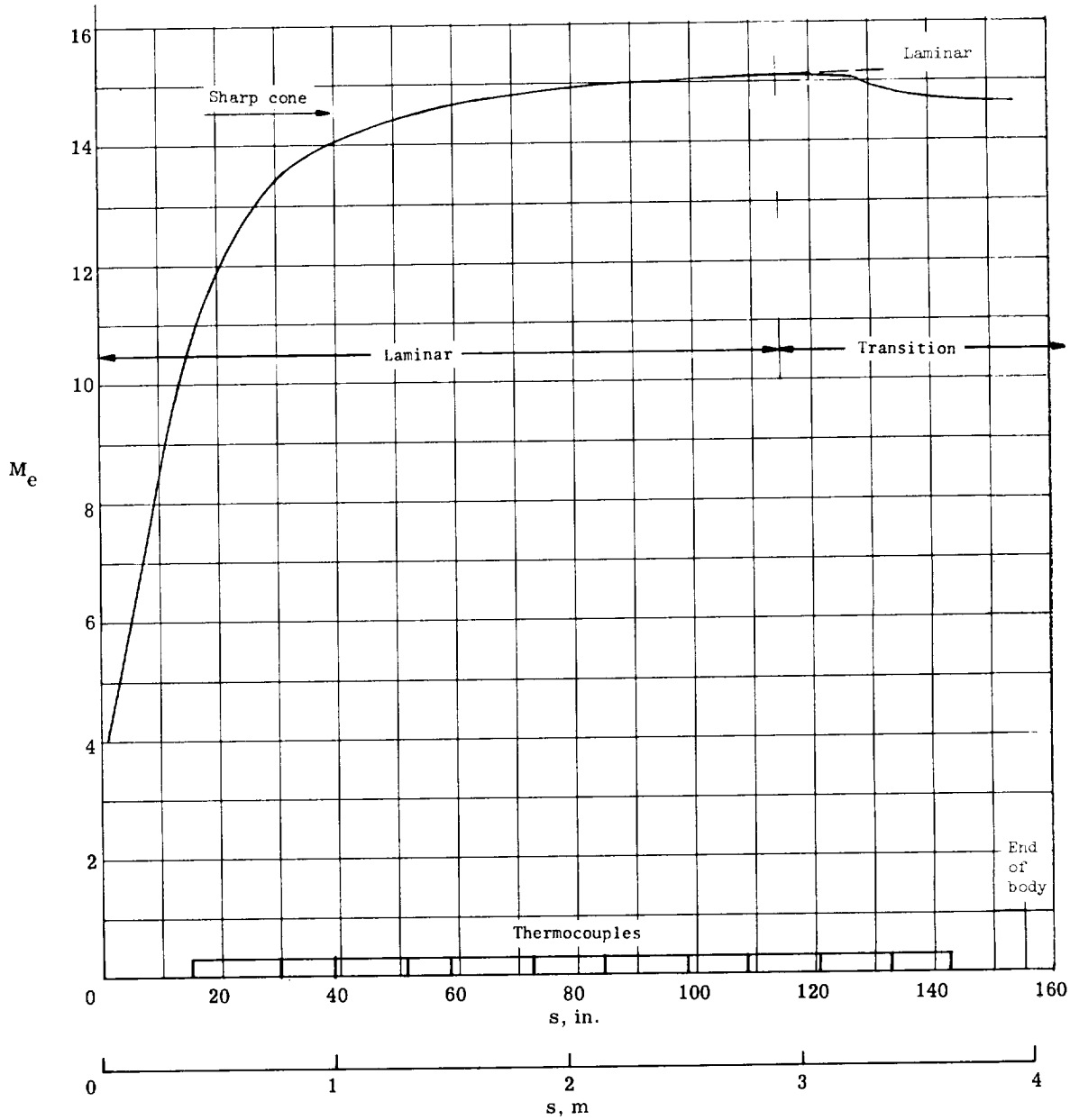

(b) h = 30.48 km (100 000 ft); V_∞ = 6.02 km/sec (19 747 ft/sec); r_n = 3.099 mm (0.122 in.); $\theta_{c,eff} = 5^o$.

Figure 5.- Continued.

[redacted]

[redacted]

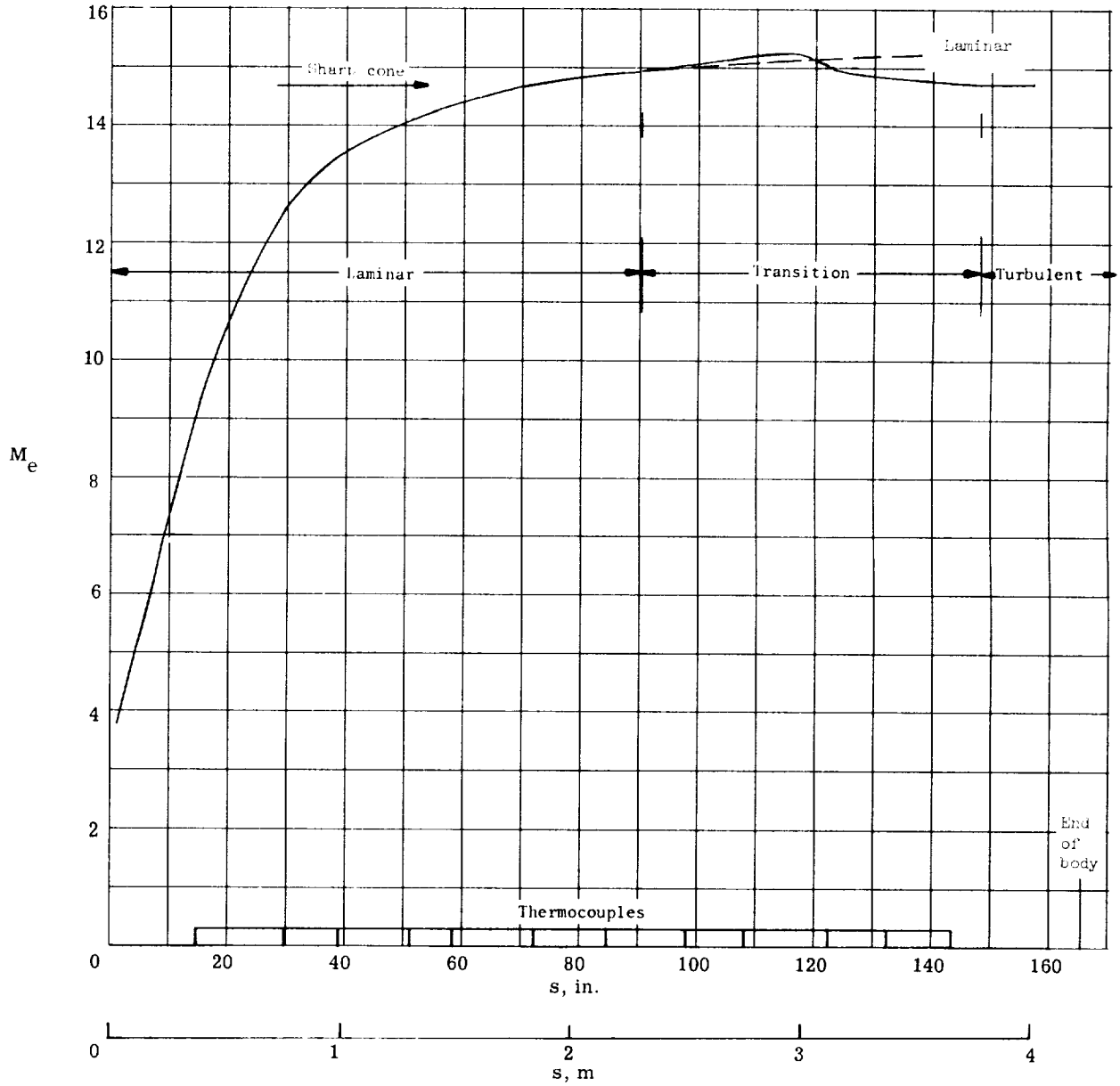

(c) h = 27.43 km (90 000 ft); V_∞ = 6.00 km/sec (19 687 ft/sec); r_n = 3.251 mm (0.128 in.); $\theta_{c,eff} = 5^o$.

Figure 5.- Continued.

[redacted]

[redacted]

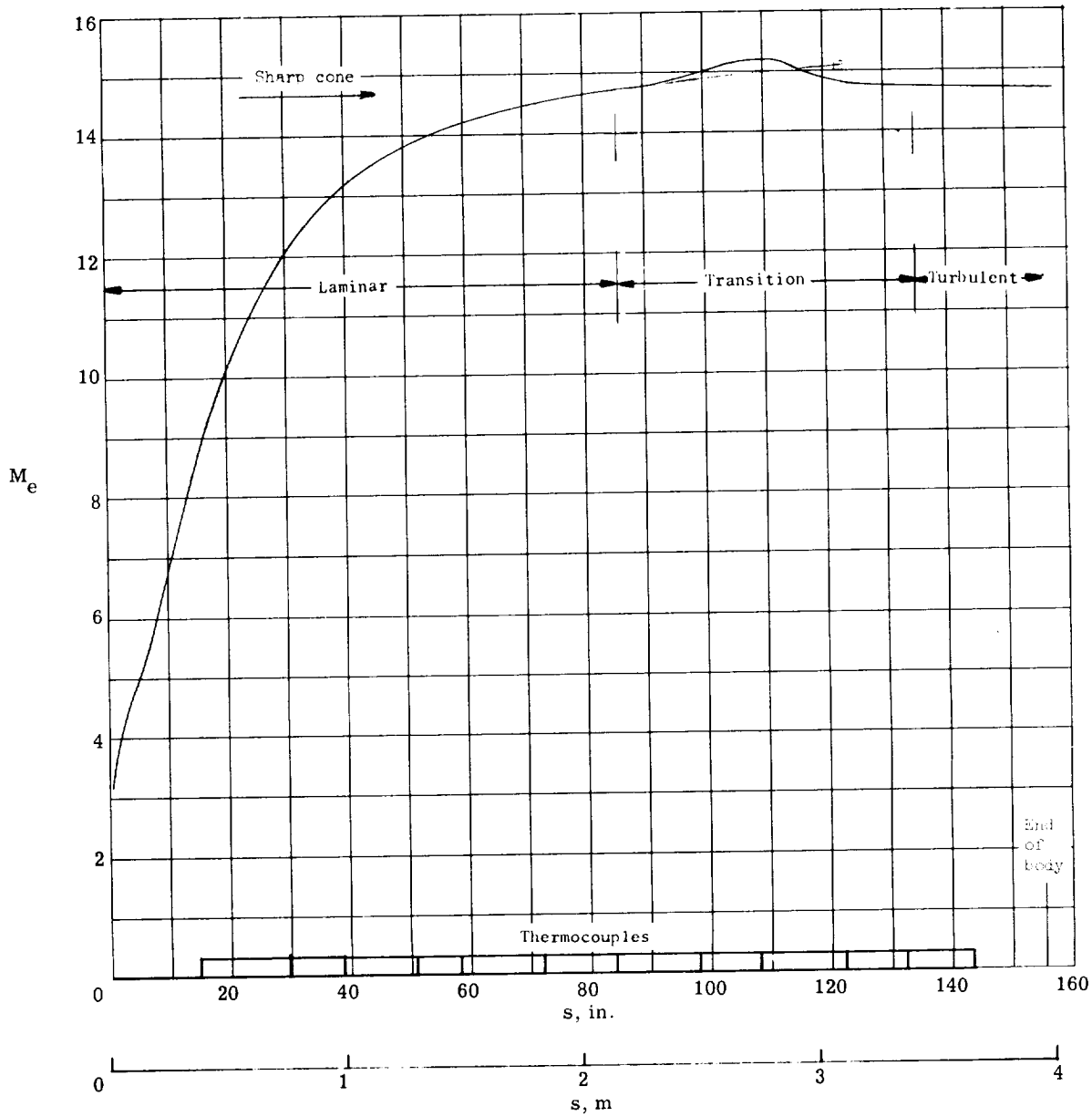

(d) h = 25.91 km (85 000 ft); V_∞ = 5.99 km/sec (19 638 ft/sec); r_n = 3.327 mm (0.131 in.); $\theta_{c,eff} = 5^o$.

Figure 5.- Continued.

[redacted]

[redacted]

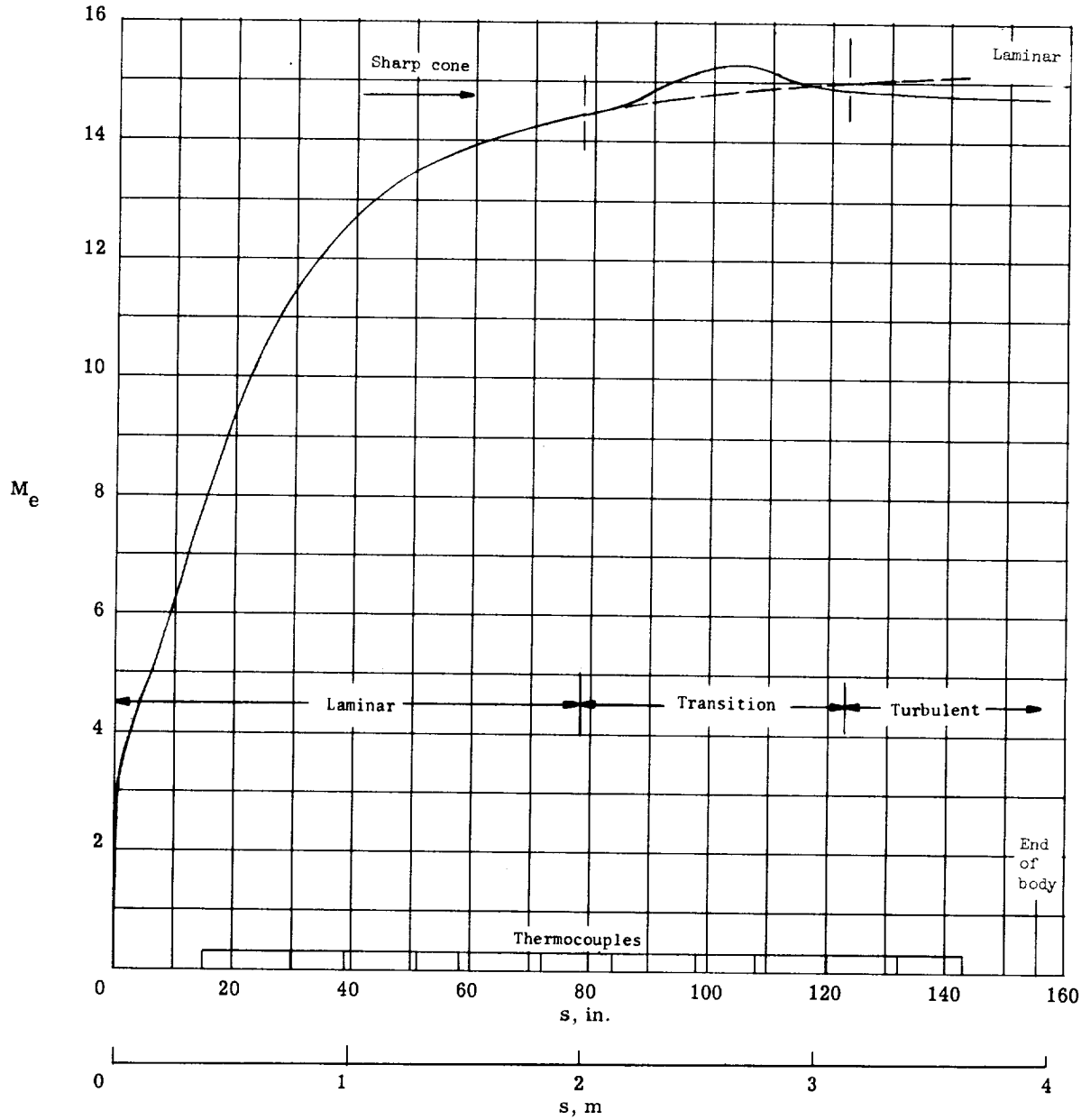

(e) h = 24.38 km (80 000 ft); V_∞ = 5.97 km/sec (19 572 ft/sec); r_n = 3.429 mm (0.135 in.); $\theta_{c,eff} = 4.860^\circ$.

Figure 5.- Continued.

[redacted]

[redacted]

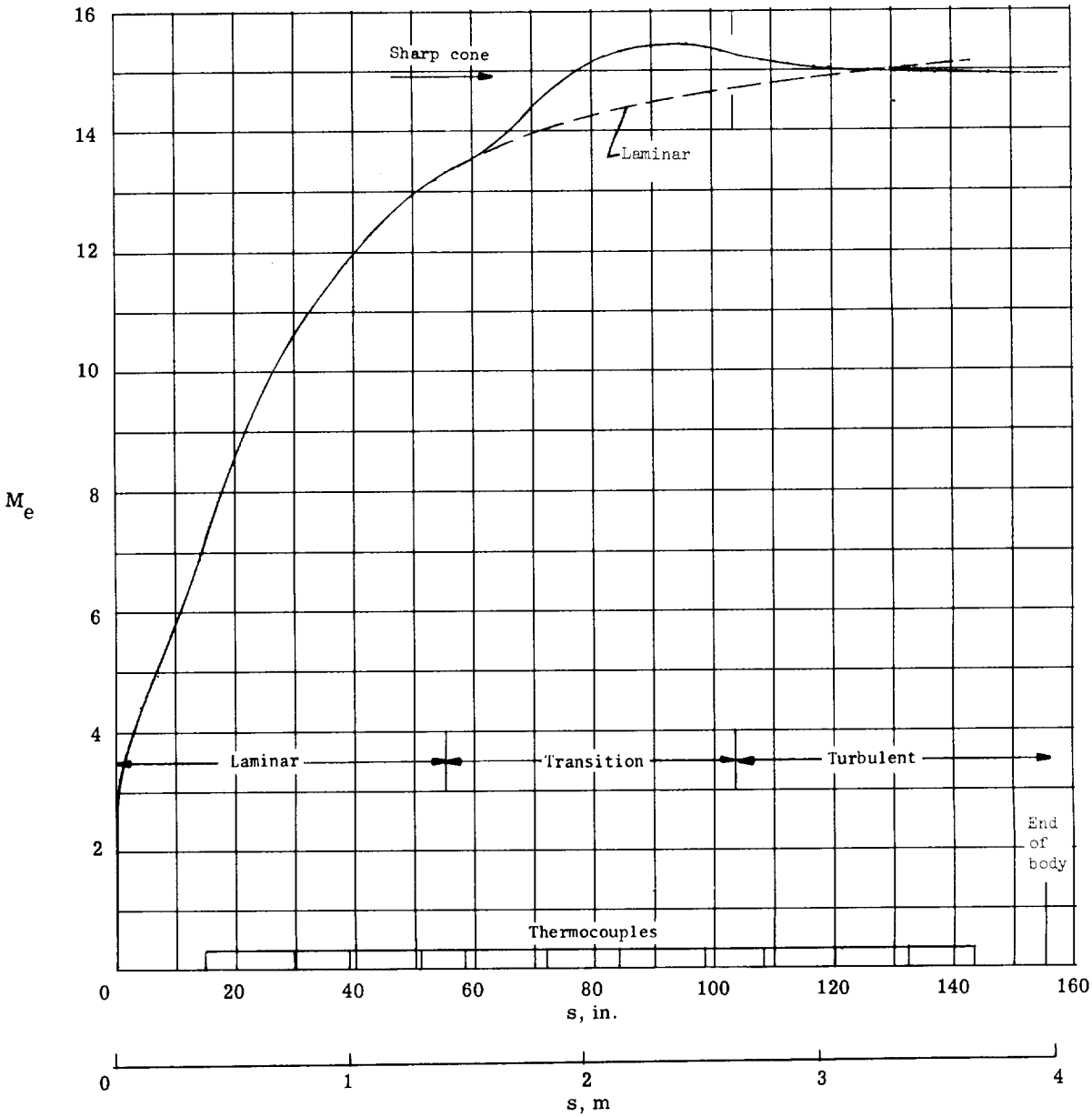

(f) h = 22.86 km (75 000 ft); V_∞ = 5.94 km/sec (19 482 ft/sec); r_n = 3.556 mm (0.140 in.); $\theta_{c,eff} = 4.575^{\circ}$.

Figure 5.- Continued.

[redacted]

[redacted]

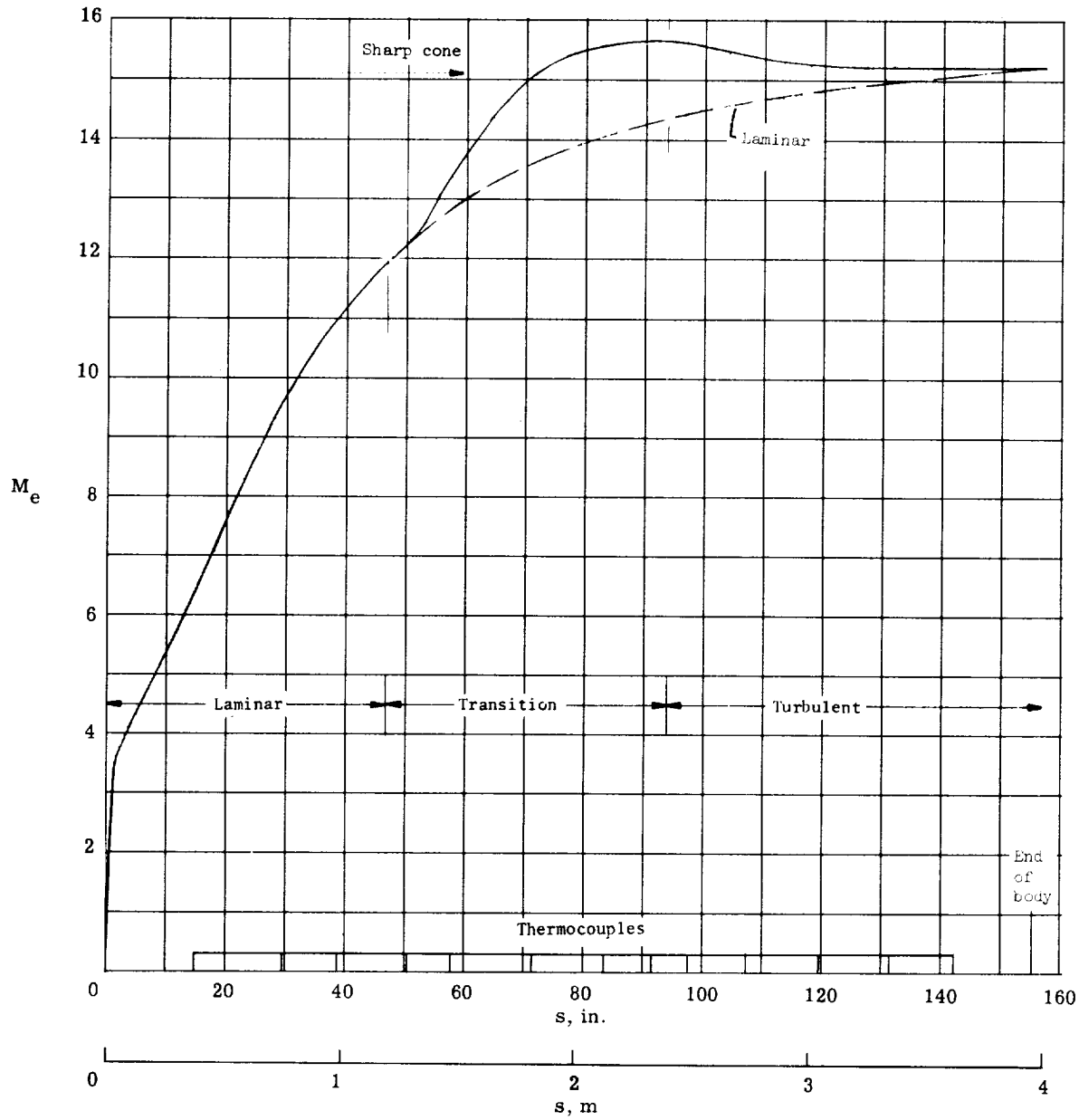

(g) h = 21.34 km (70 000 ft); V_∞ = 5.90 km/sec (19 367 ft/sec); r_n = 3.683 mm (0.145 in.); $\theta_{c,eff}$ = 4.340°.

Figure 5.- Continued.

[redacted]

[redacted]

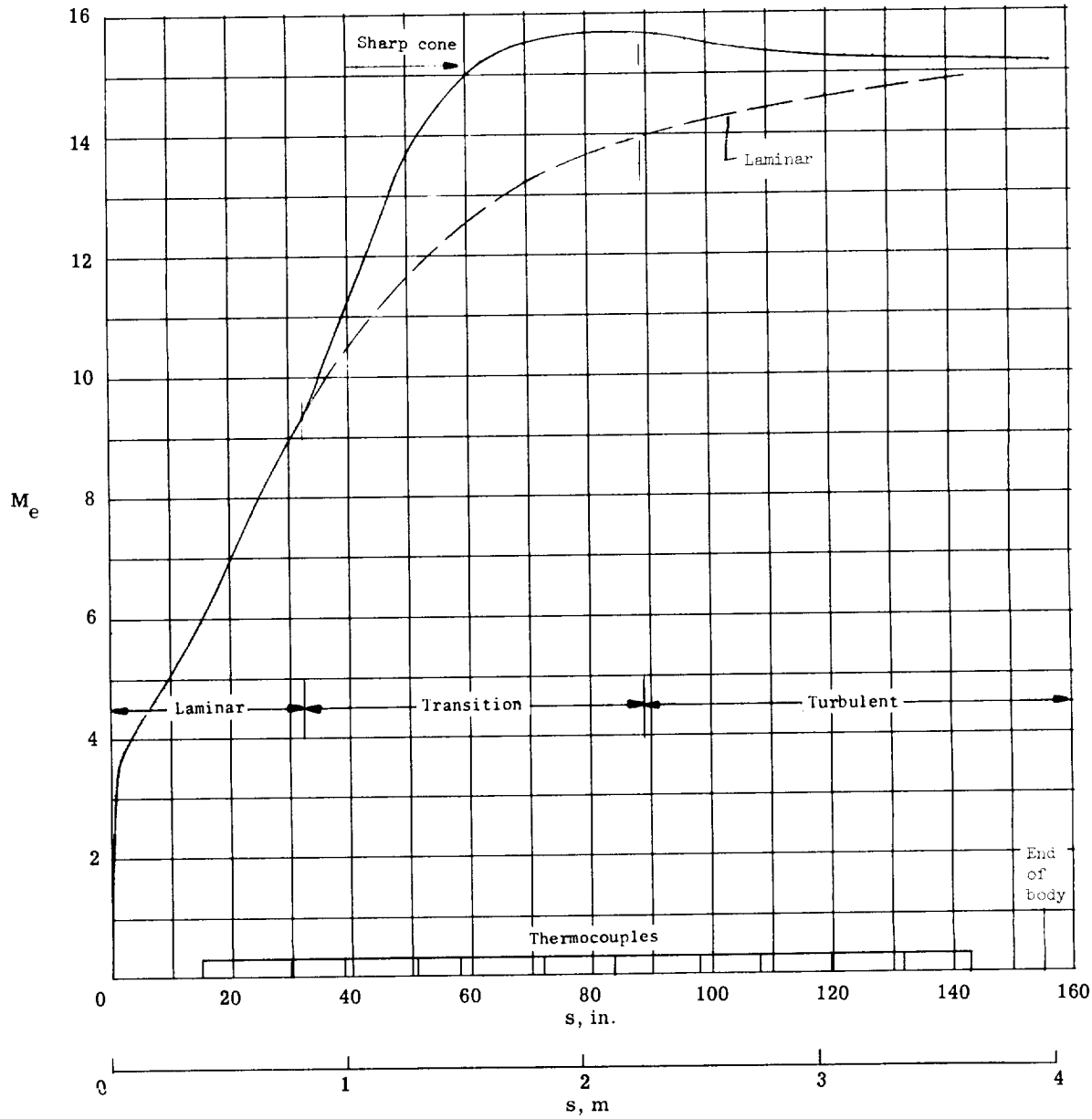

(h) h = 19.81 km (65 000 ft); V_∞ = 5.86 km/sec (19 215 ft/sec); r_n = 3.835 mm (0.151 in.); $\theta_{c,eff} = 4.285^{\circ}$.

Figure 5.- Continued.

[redacted]

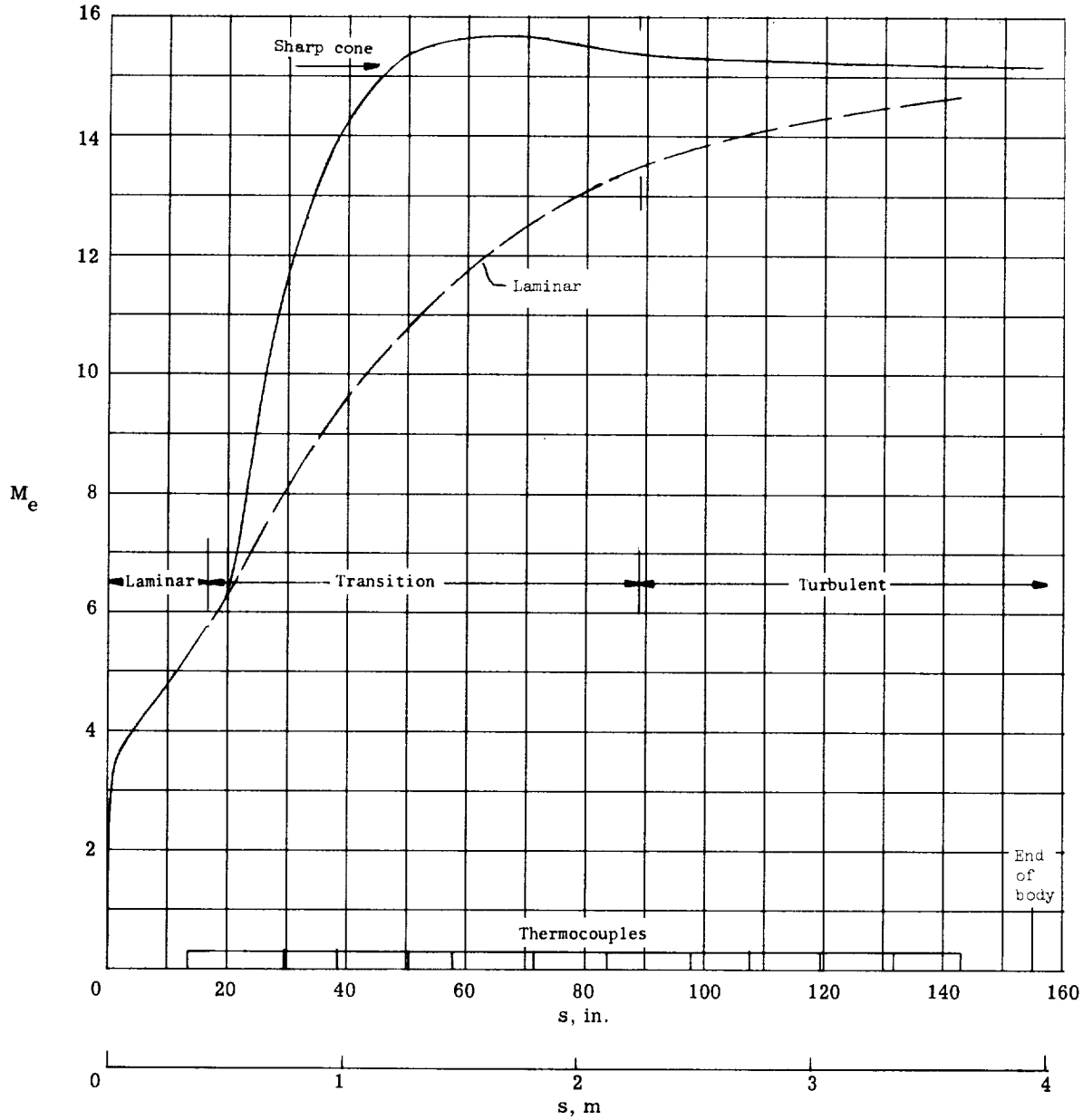

(i) h = 18.29 km (60 000 ft); V_∞ = 5.80 km/sec (19 018 ft/sec); r_n = 3.988 mm (0.157 in.); $\theta_{c,eff}$ = 4.250°.

Figure 5.- Continued.

[redacted]

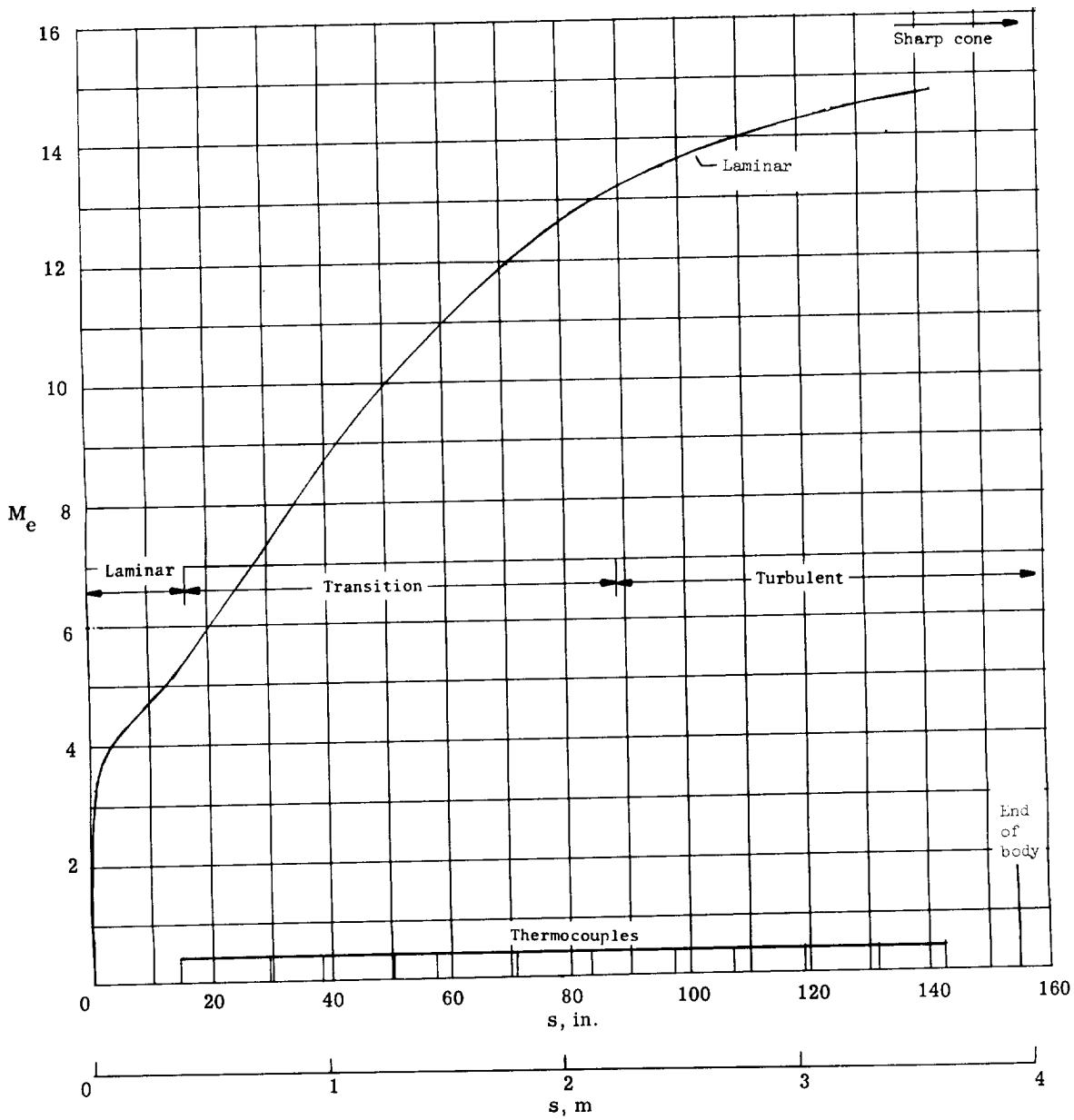

(j) h = 18.29 km (60 000 ft); V_∞ = 5.80 km/sec (19 018 ft/sec); r_n = 3.988 mm (0.157 in.); $\theta_{c,eff} = 3.45^{\circ}$.

Figure 5.- Concluded.

[redacted]

[redacted]

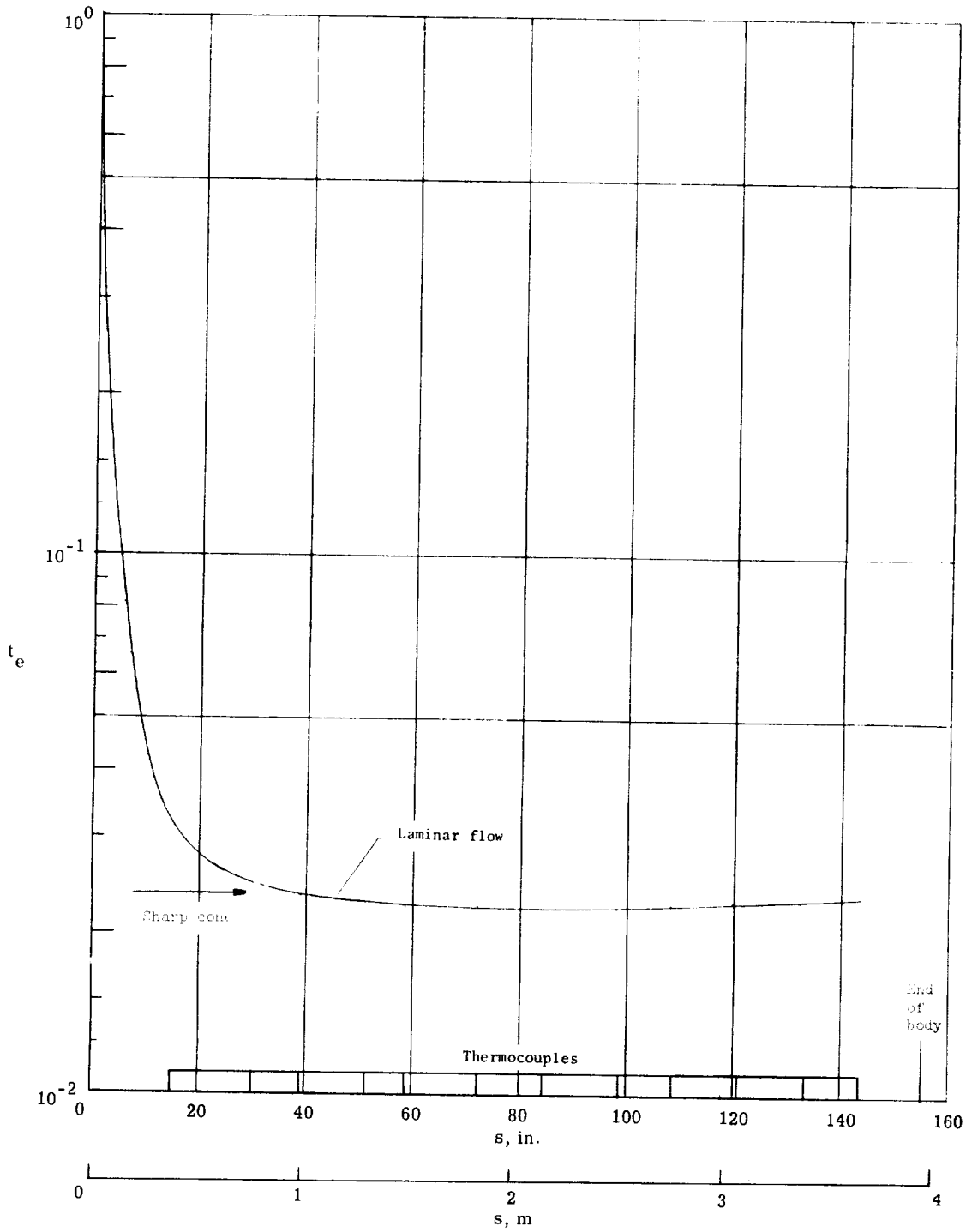

(a) h = 36.58 km (120 000 ft); V_∞ = 6.03 km/sec (19 786 ft/sec); r_n = 2.896 mm (0.114 in.); $\theta_{c,eff} = 5^o$.

Figure 6.- Local edge enthalpy ratio along vehicle. $\theta_s = 5^o$.

[redacted]

[redacted]

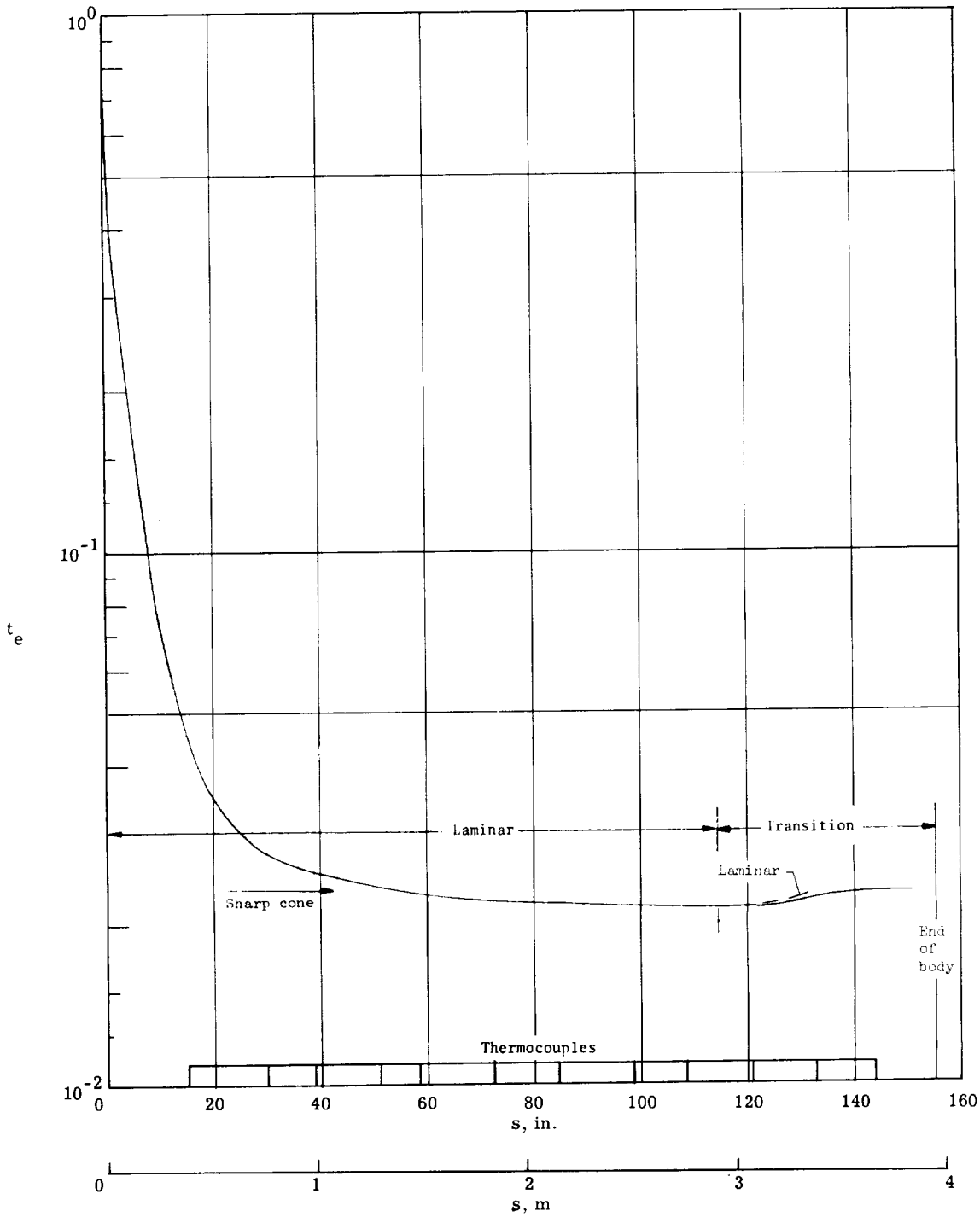

(b) h = 30.48 km (100 000 ft); V_∞ = 6.02 km/sec (19 747 ft/sec); r_n = 3.099 mm (0.122 in.); $\theta_{c,eff} = 5^\circ$.

Figure 6.- Continued.

[redacted]

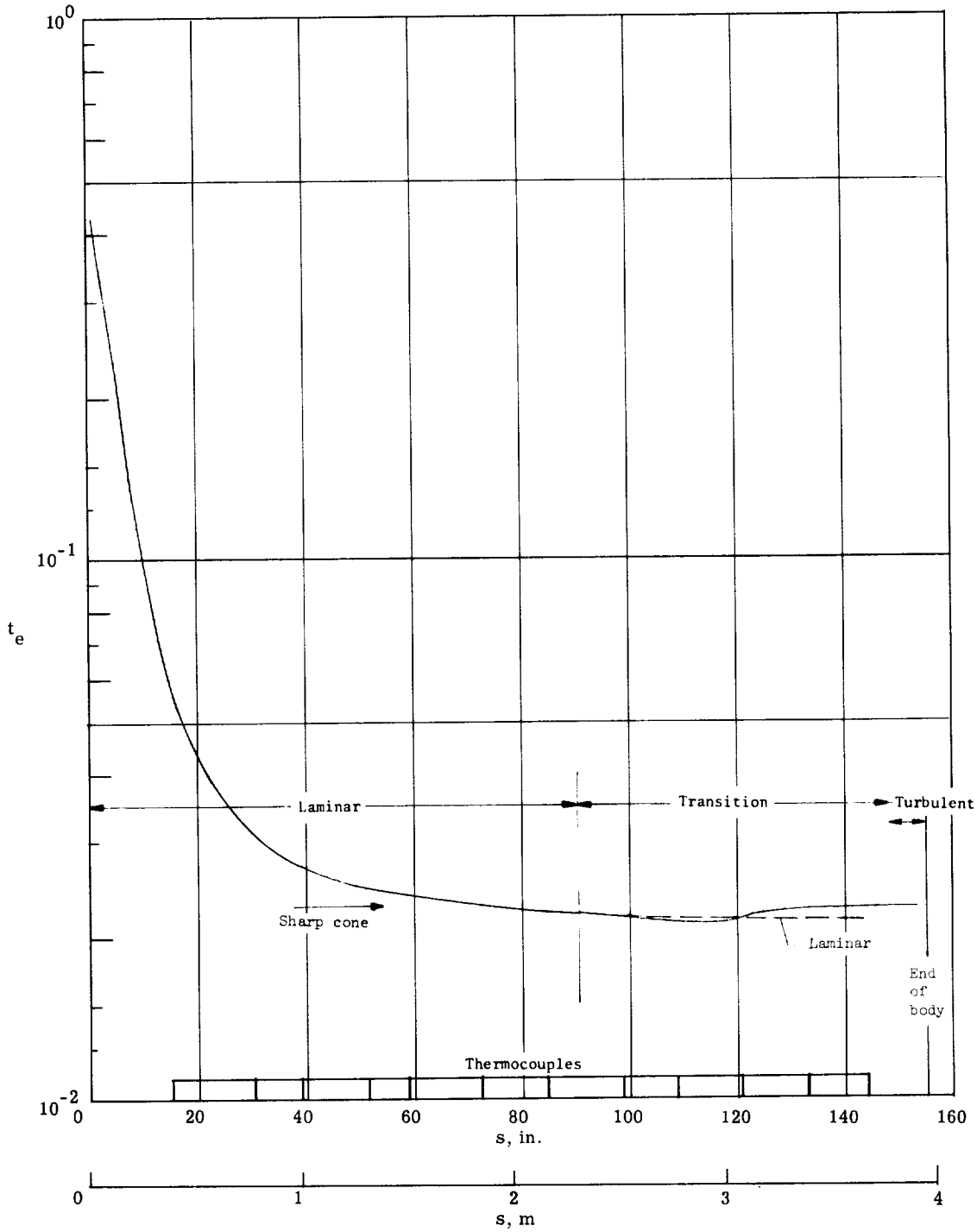

(c) h = 27.43 km (90 000 ft); V_∞ = 6.00 km/sec (19 687 ft/sec); r_n = 3.251 mm (0.128 in.); $\theta_{c,eff} = 5^\circ$.

Figure 6.- Continued.

[redacted]

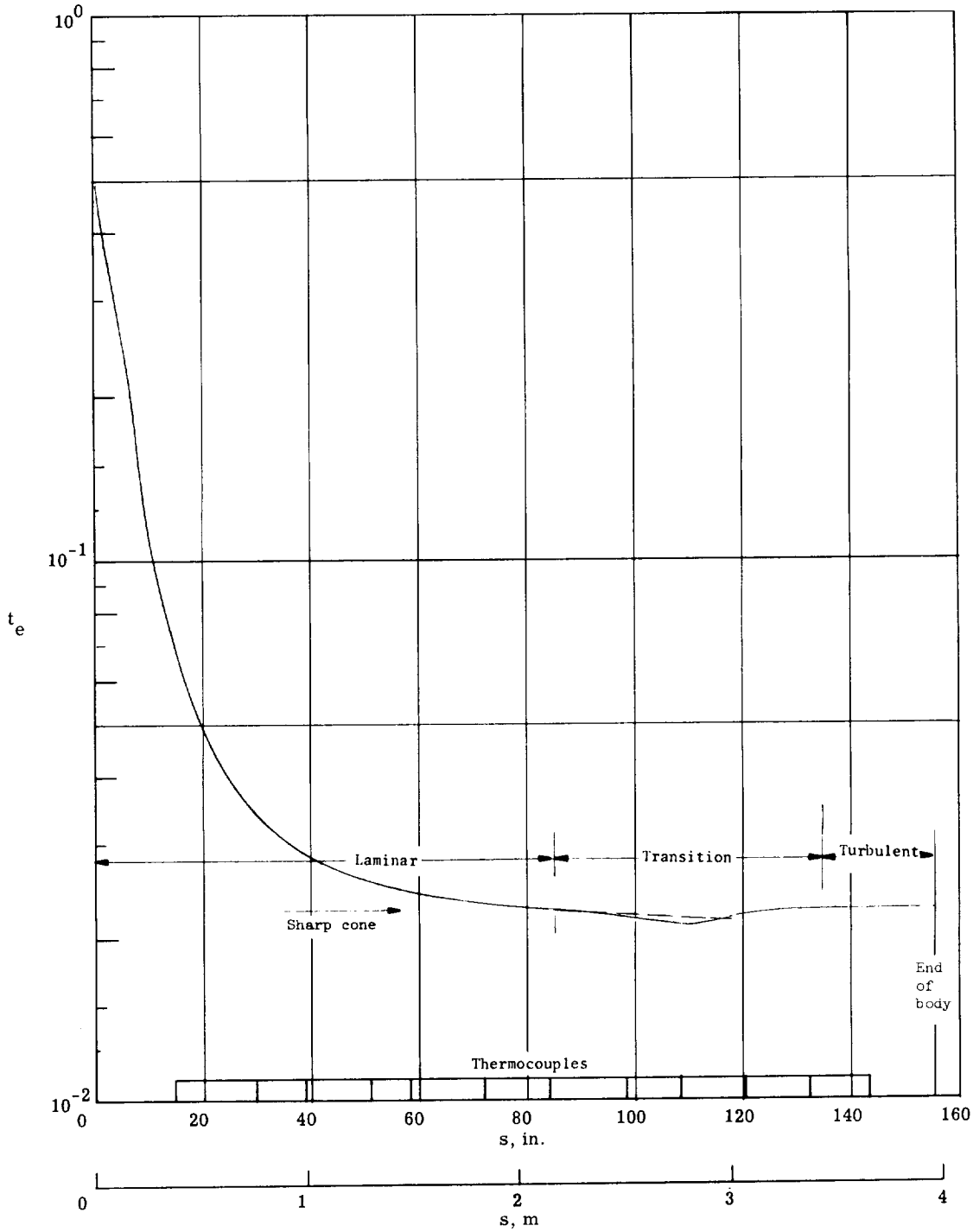

(d) h = 25.91 km (85 000 ft); V_∞ = 5.99 km/sec (19 638 ft/sec); r_n = 3.327 mm (0.131 in.); $\theta_{c,eff} = 5^\circ$.

Figure 6.- Continued.

[redacted]

[redacted]

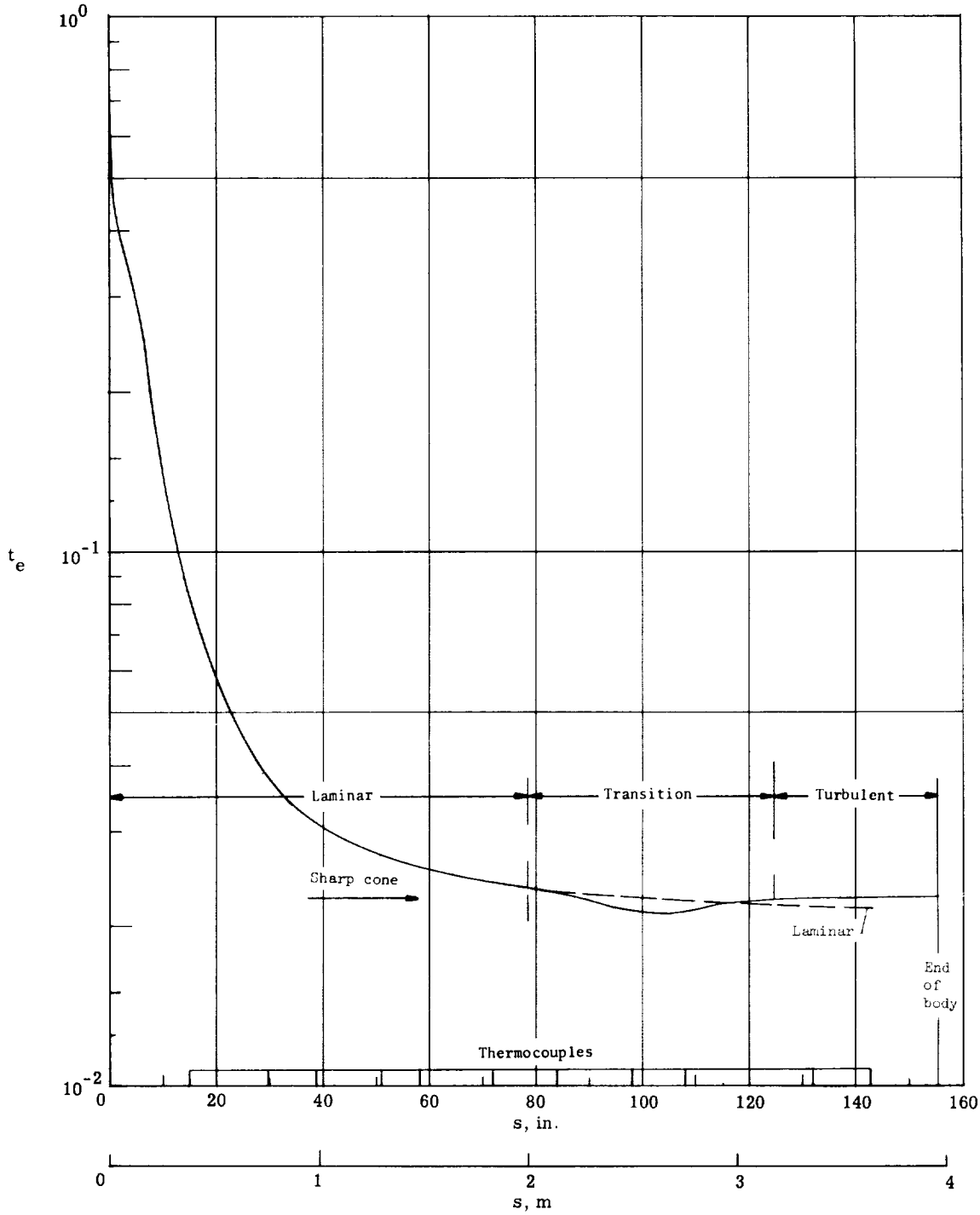

(e) h = 24.38 km (80 000 ft); V_∞ = 5.97 km/sec (19 572 ft/sec); r_n = 3.429 mm (0.135 in.); $\theta_{c,eff} = 4.860^\circ$.

Figure 6.- Continued.

[redacted]

[redacted]

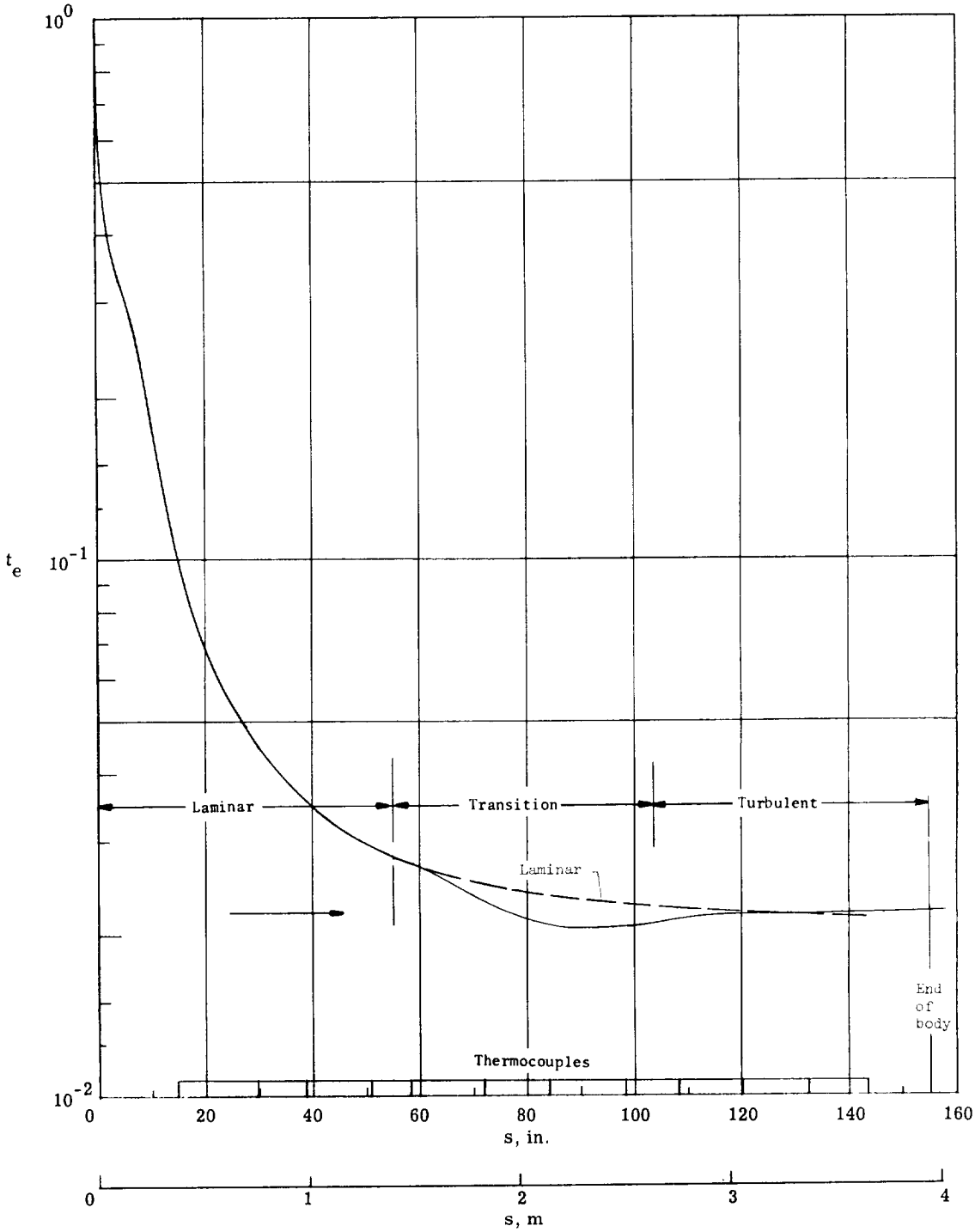

(f) h = 22.86 km (75 000 ft); V_∞ = 5.94 km/sec (19 482 ft/sec); r_n = 3.556 mm (0.140 in.); $\theta_{c,eff}$ = 4.575°.

Figure 6.- Continued.

[redacted]

[redacted]

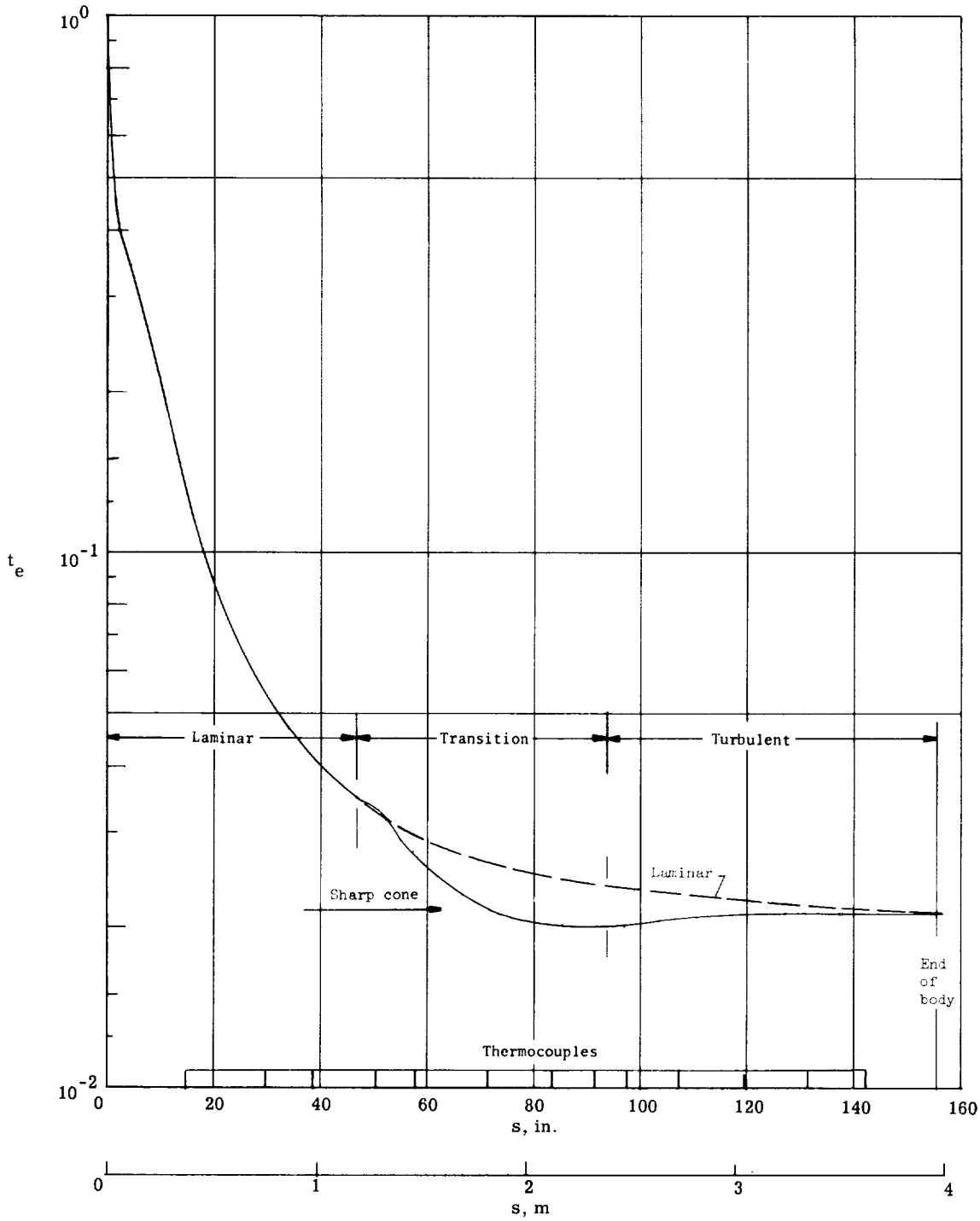

(g) h = 21.34 km (70 000 ft); V_∞ = 5.90 km/sec (19 367 ft/sec); r_n = 3.683 mm (0.145 in.); $\theta_{c,eff} = 4.340^\circ$.

Figure 6.- Continued.

[redacted]

[redacted]

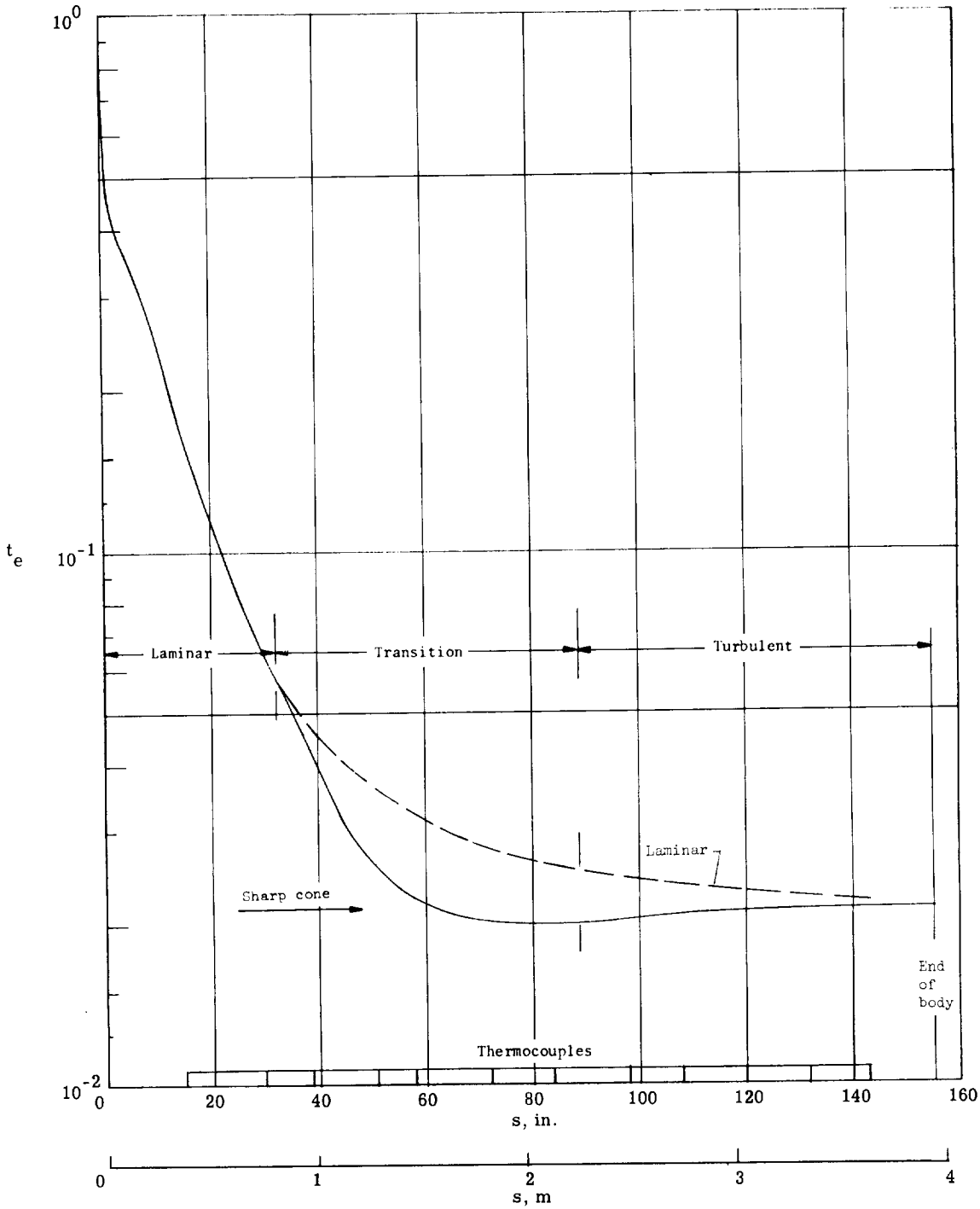

(h) h = 19.81 km (65 000 ft); V_∞ = 5.86 km/sec (19 215 ft/sec); r_n = 3.835 mm (0.151 in.); $\theta_{c,eff} = 4.285^\circ$.

Figure 6.- Continued.

[redacted]

[redacted]

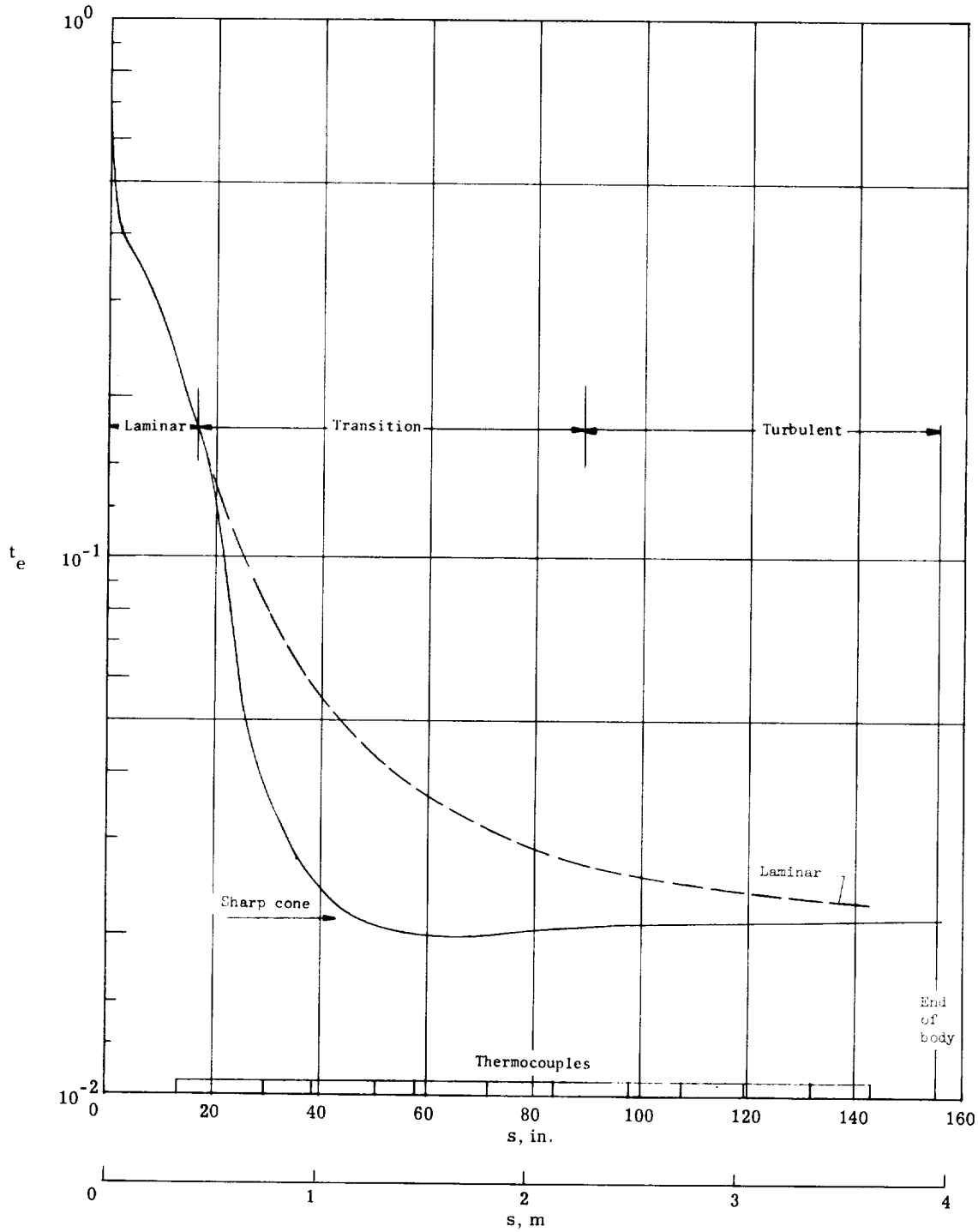

(i) h = 18.29 km (60 000 ft); V_∞ = 5.80 km/sec (19 018 ft/sec); r_n = 3.988 mm (0.157 in.); $\theta_{c,eff} = 4.250^\circ$.

Figure 6.- Continued.

[redacted]

[redacted]

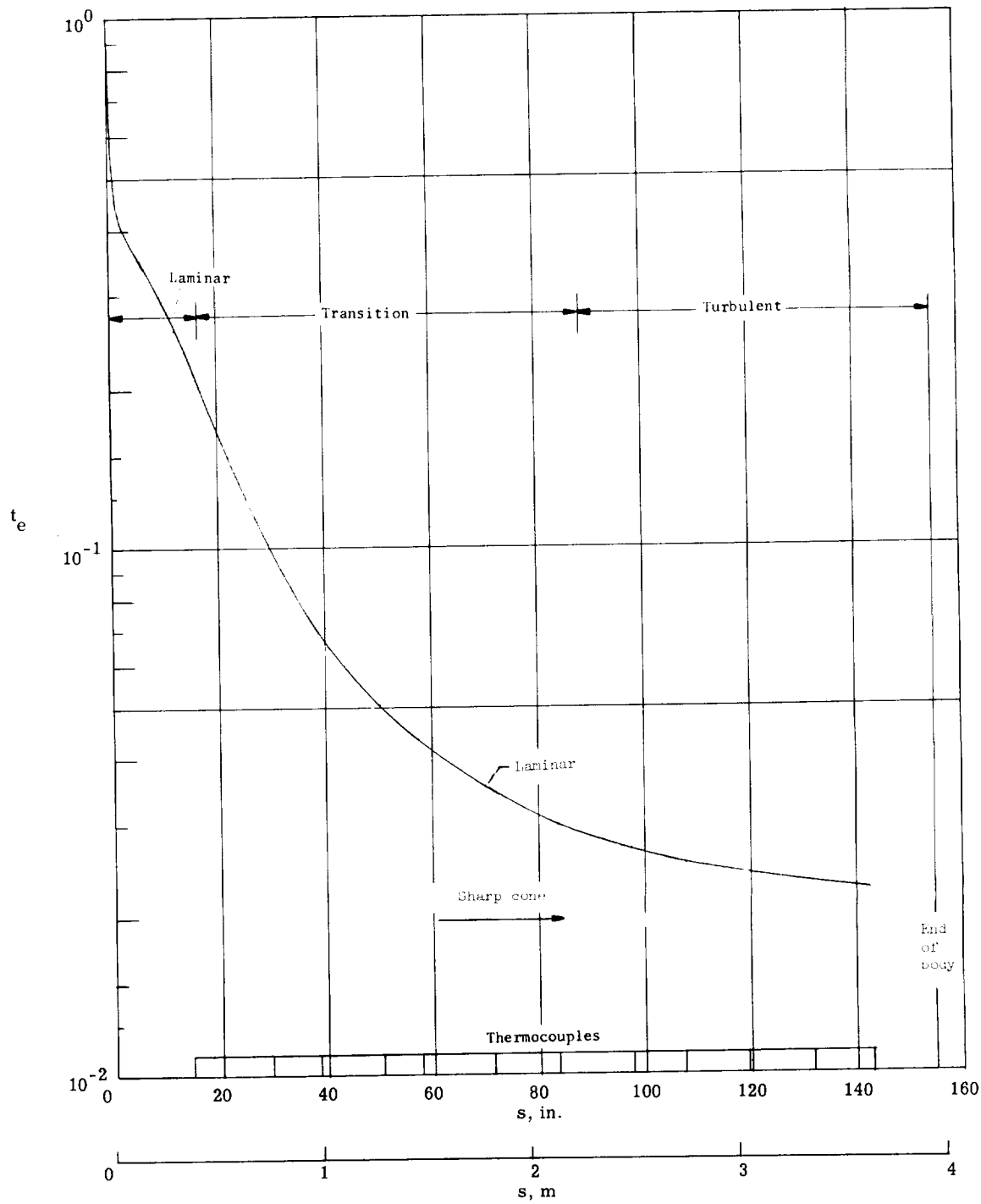

(j) h = 18.29 km (60 000 ft); V_∞ = 5.80 km/sec (19 018 ft/sec); r_n = 3.988 mm (0.157 in.); $\theta_{c,eff} = 3.45^\circ$.

Figure 6.- Concluded.

[redacted]

[redacted]

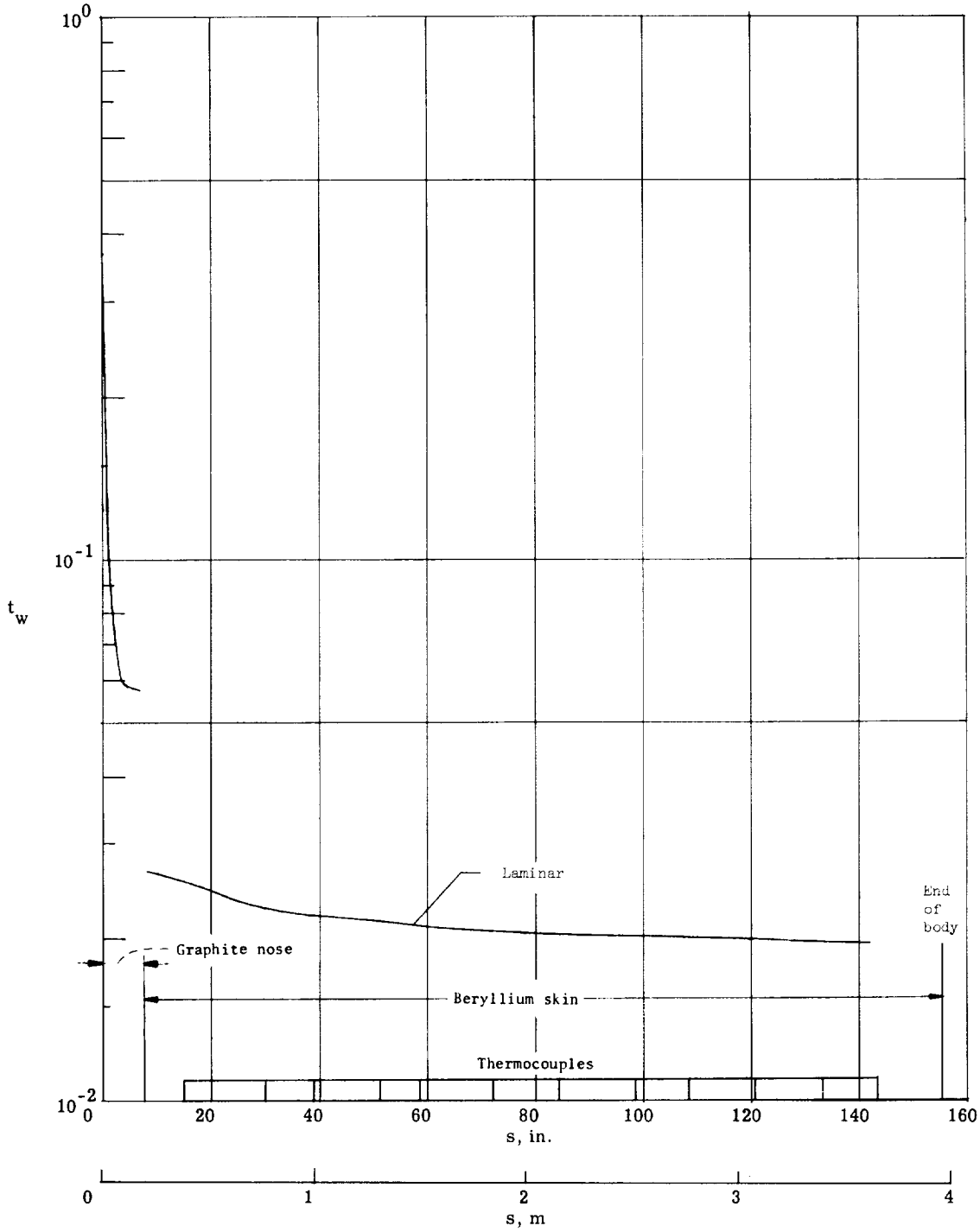

(a) h = 36.58 km (120 000 ft); V_∞ = 6.03 km/sec (19 786 ft/sec); r_n = 2.896 mm (0.114 in.); $\theta_{c,eff} = 5^o$.

Figure 7.- Local wall enthalpy ratio along vehicle $\theta_s = 5^o$.

[redacted]

[redacted]

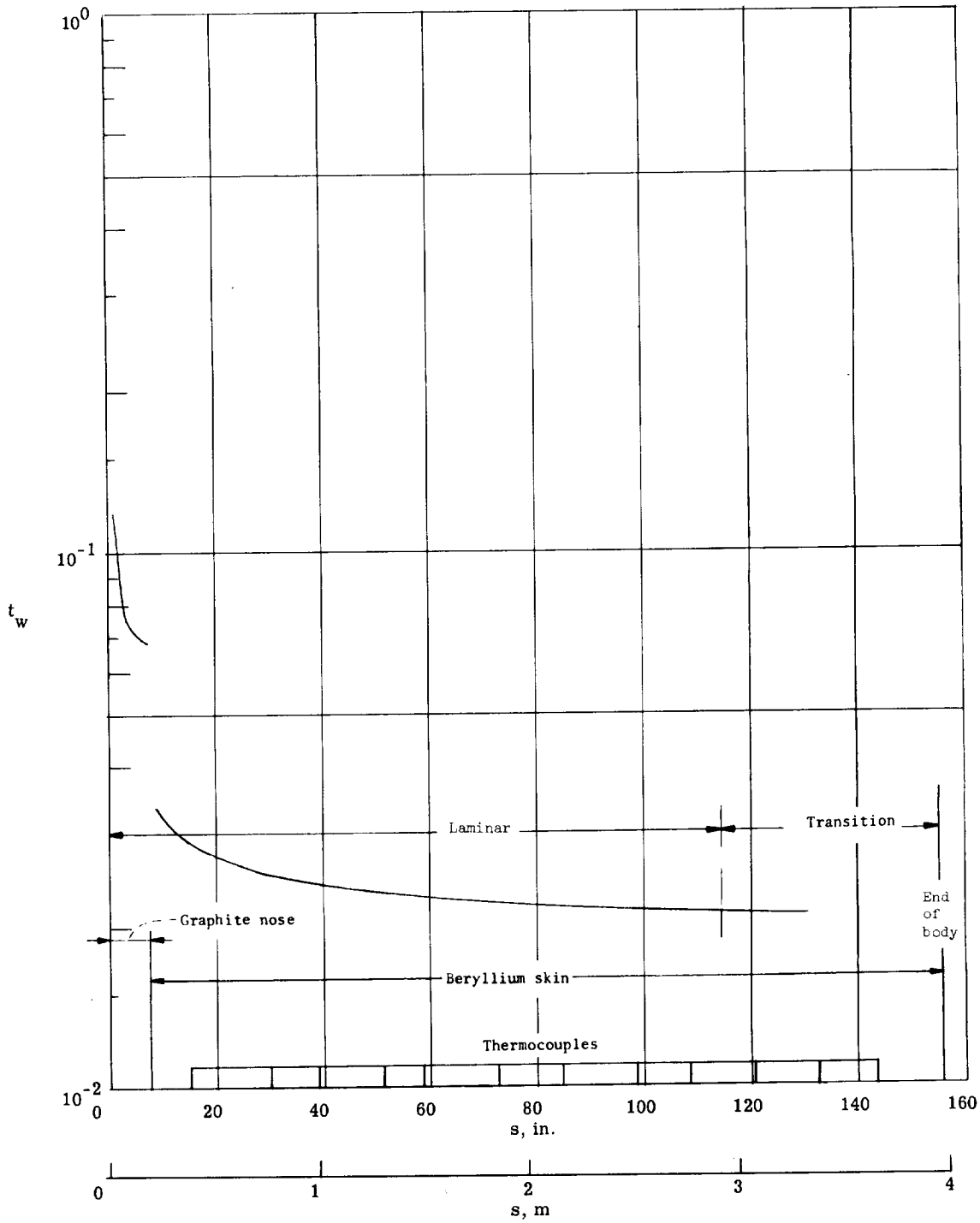

(b) h = 30.48 km (100 000 ft); V_∞ = 6.02 km/sec (19 747 ft/sec); r_n = 3.099 mm (0.122 in.); $\theta_{c,eff} = 5^o$.

Figure 7.- Continued.

[redacted]

[redacted]

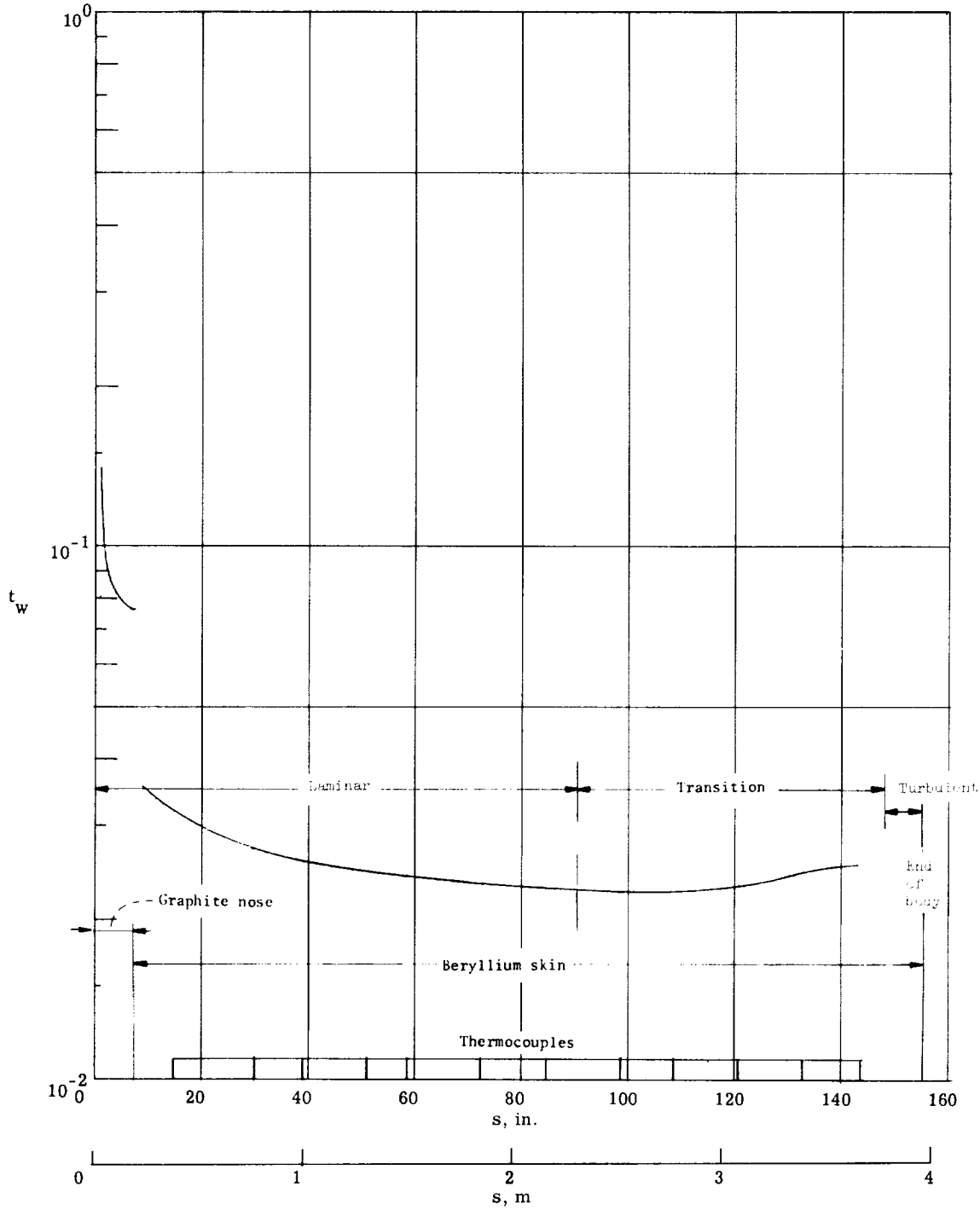

(c) h = 27.43 km (90 000 ft); V_∞ = 6.00 km/sec (19 687 ft/sec); r_n = 3.251 mm (0.128 in.); $\theta_{c,eff} = 5^o$.

Figure 7.- Continued.

[redacted]

[redacted]

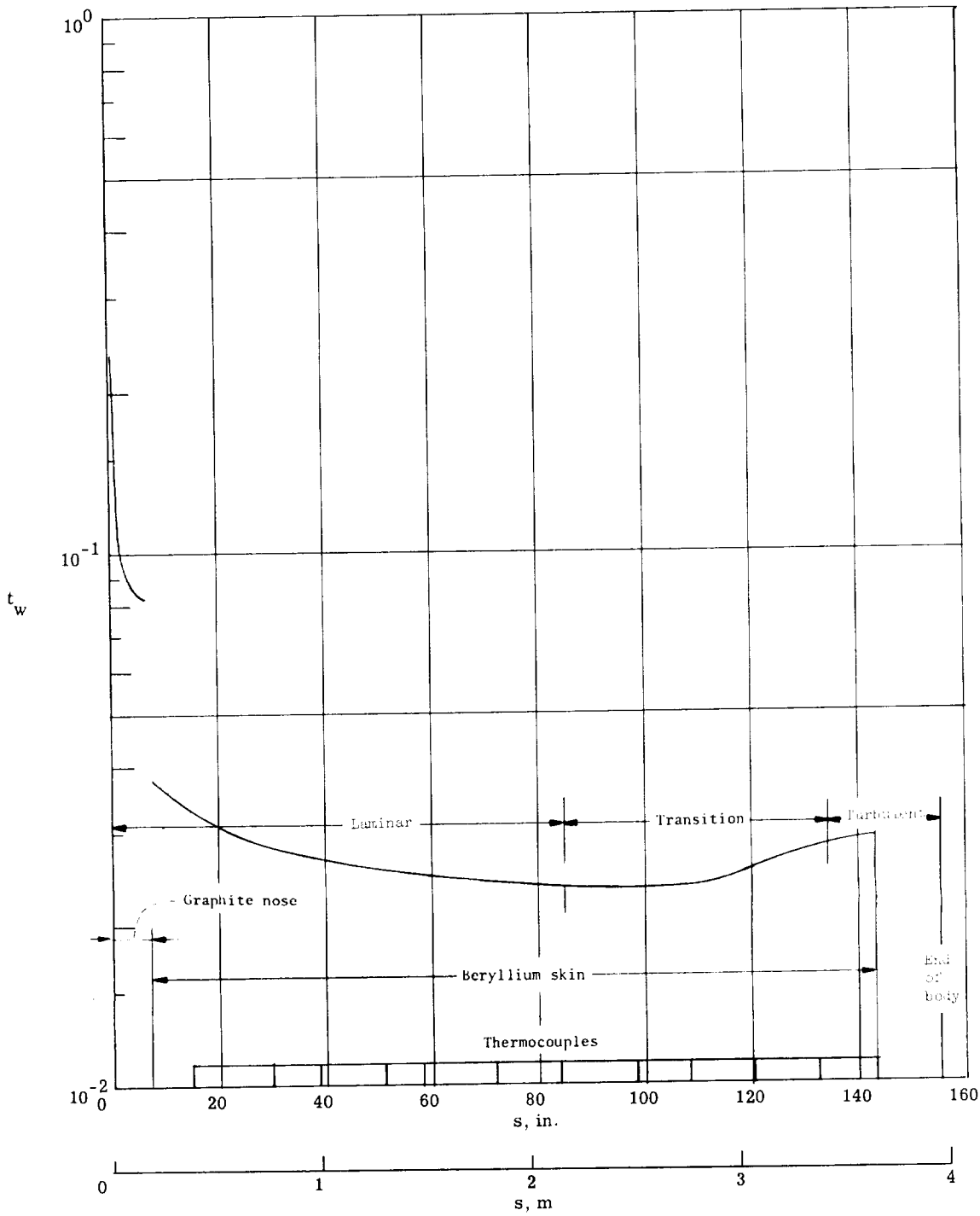

(d) h = 25.91 km (85 000 ft); V_∞ = 5.99 km/sec (19 638 ft/sec); r_n = 3.327 mm (0.131 in.); $\theta_{c,eff} = 5^o$.

Figure 7.- Continued.

[redacted]

[redacted]

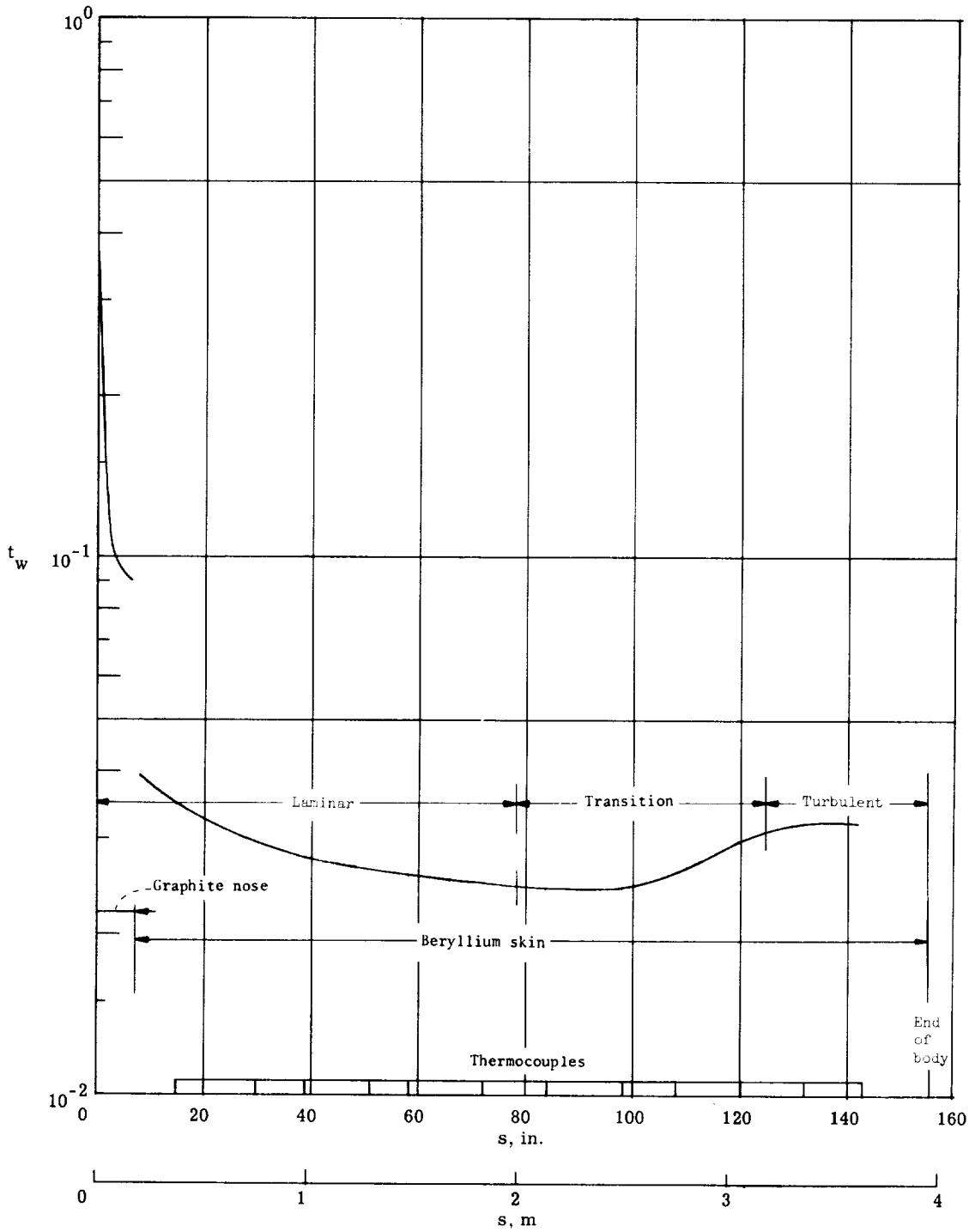

(e) h = 24.38 km (80 000 ft); V_∞ = 5.97 km/sec (19 572 ft/sec); r_n = 3.429 mm (0.135 in.); $\theta_{c,eff} = 4.860^\circ$.

Figure 7.- Continued.

[redacted]

[redacted]

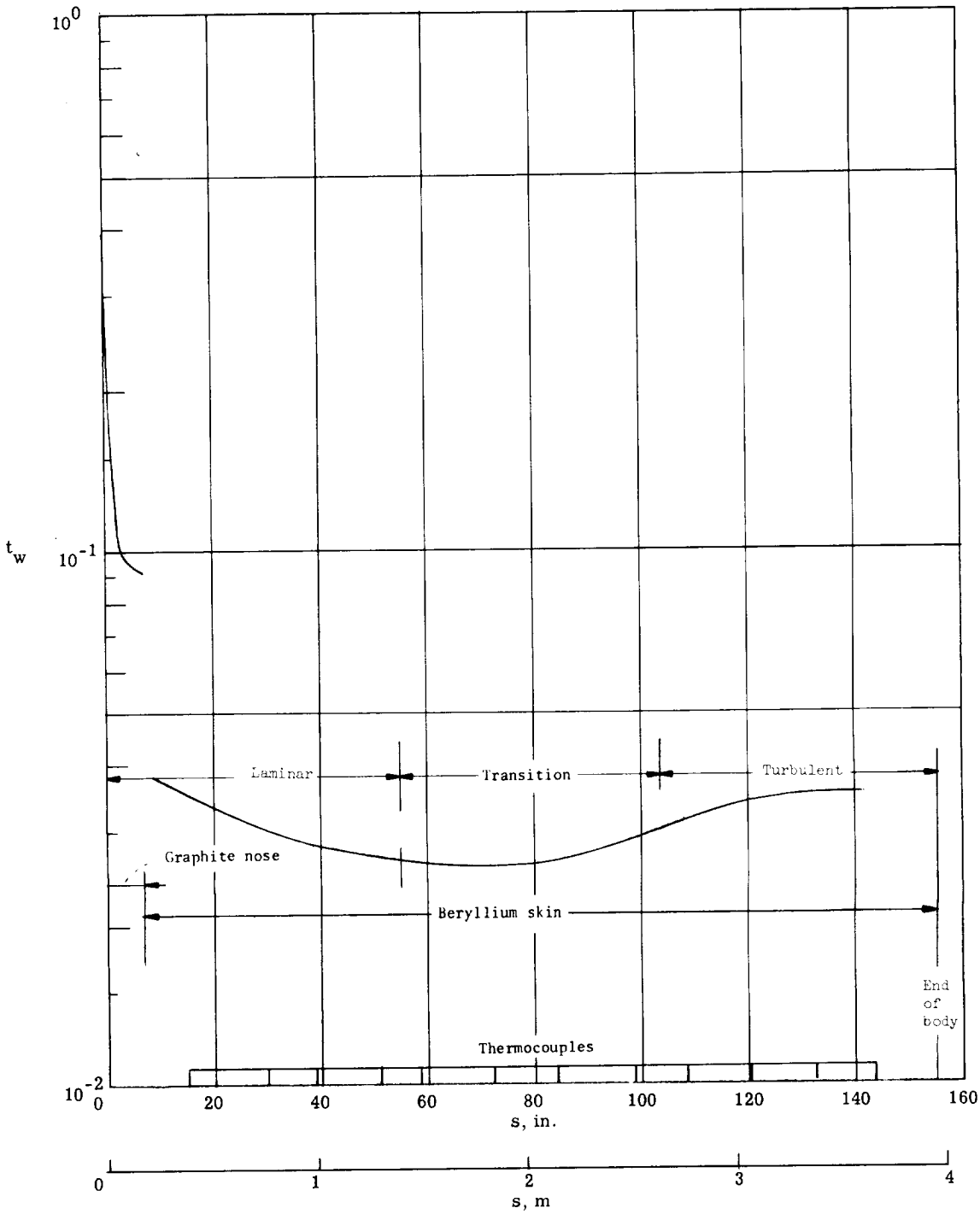

(f) h = 22.86 km (75 000 ft); V_∞ = 5.94 km/sec (19 482 ft/sec); r_n = 3.556 mm (0.140 in.); $\theta_{c,eff} = 4.575^\circ$.

Figure 7.- Continued.

[redacted]

[redacted]

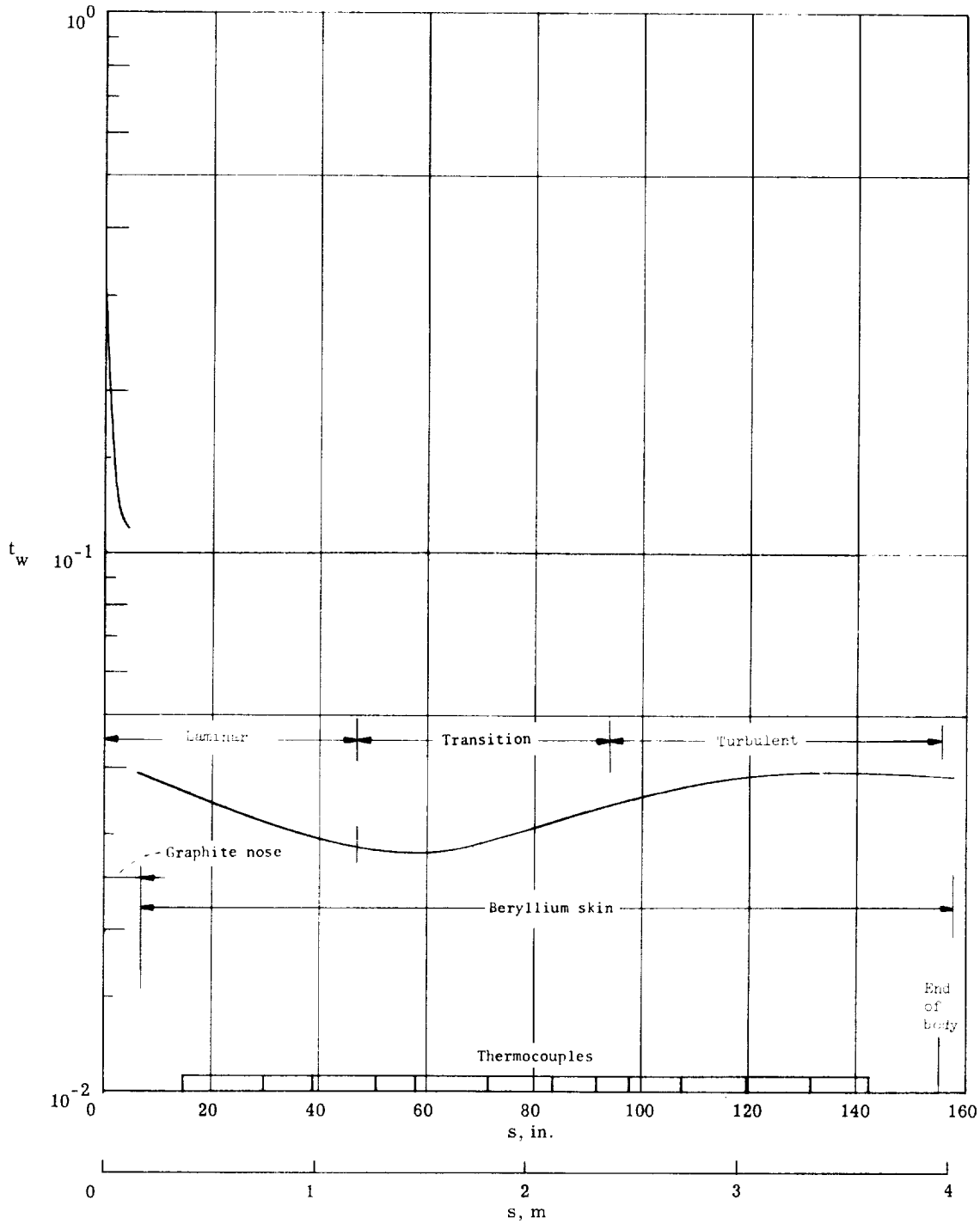

(g) h = 21.34 km (70 000 ft); V_∞ = 5.90 km/sec (19 367 ft/sec); r_n = 3.683 mm (0.145 in.); $\theta_{c,eff} = 4.340^\circ$.

Figure 7.- Continued.

[redacted]

[redacted]

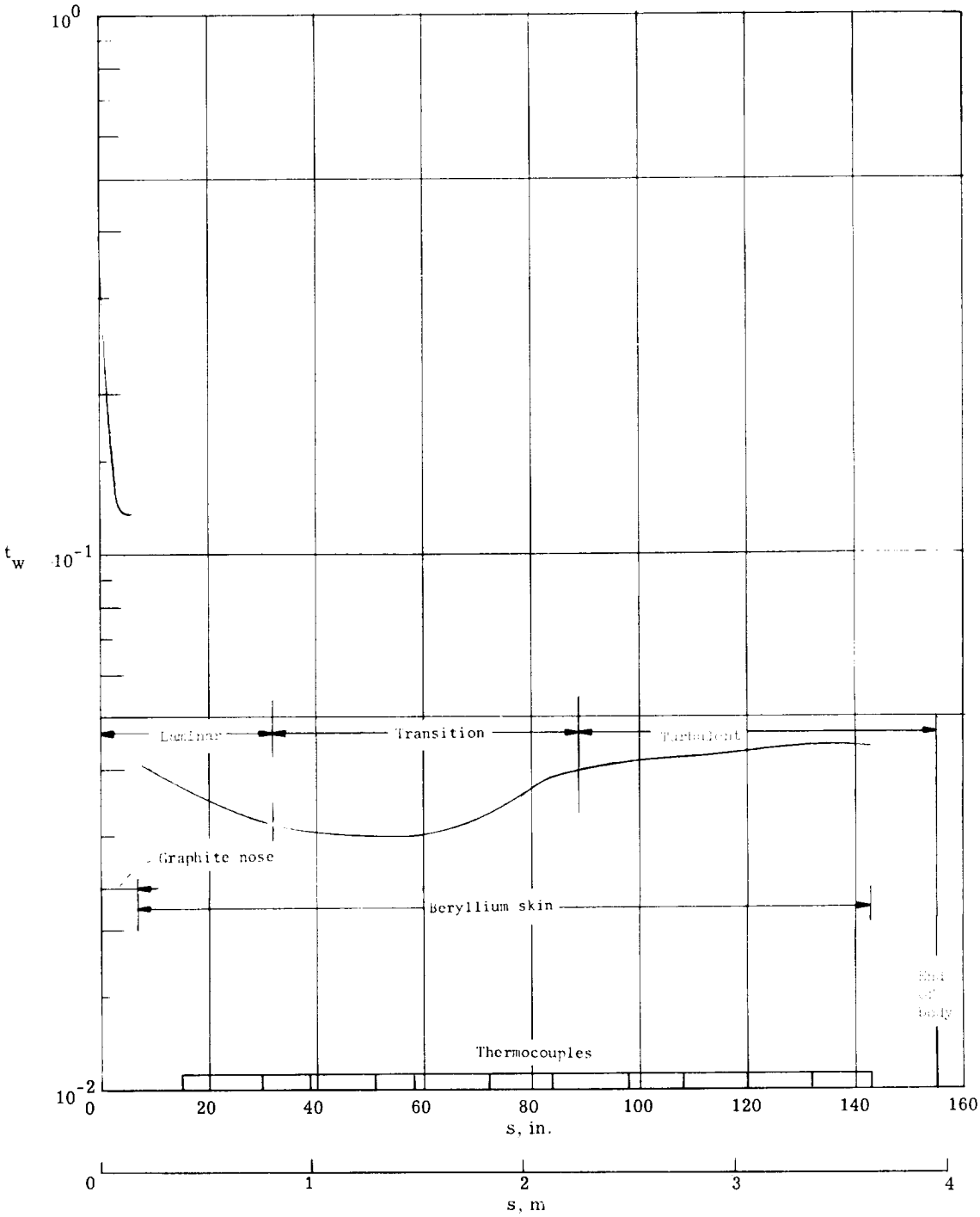

(h) h = 19.81 km (65 000 ft); V_∞ = 5.86 km/sec (19 215 ft/sec); r_n = 3.835 mm (0.151 in.); $\theta_{c,eff} = 4.285^\circ$.

Figure 7.- Continued.

[redacted]

[redacted]

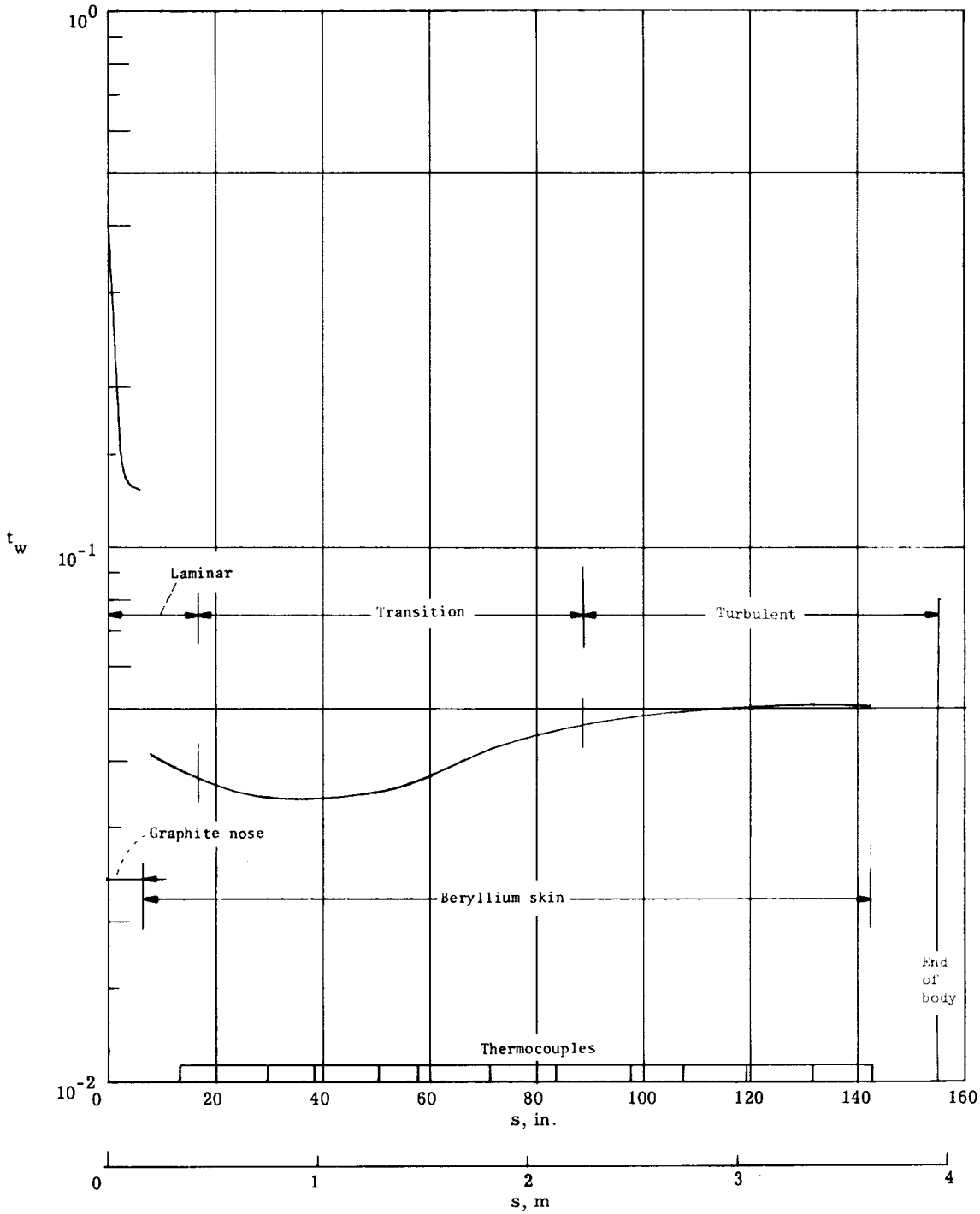

(i) h = 18.29 km (60 000 ft); V_∞ = 5.80 km/sec (19 018 ft/sec); r_n = 3.988 mm (0.157 in.); $\theta_{c,eff}$ = 4.250°.

Figure 7.- Continued.

[redacted]

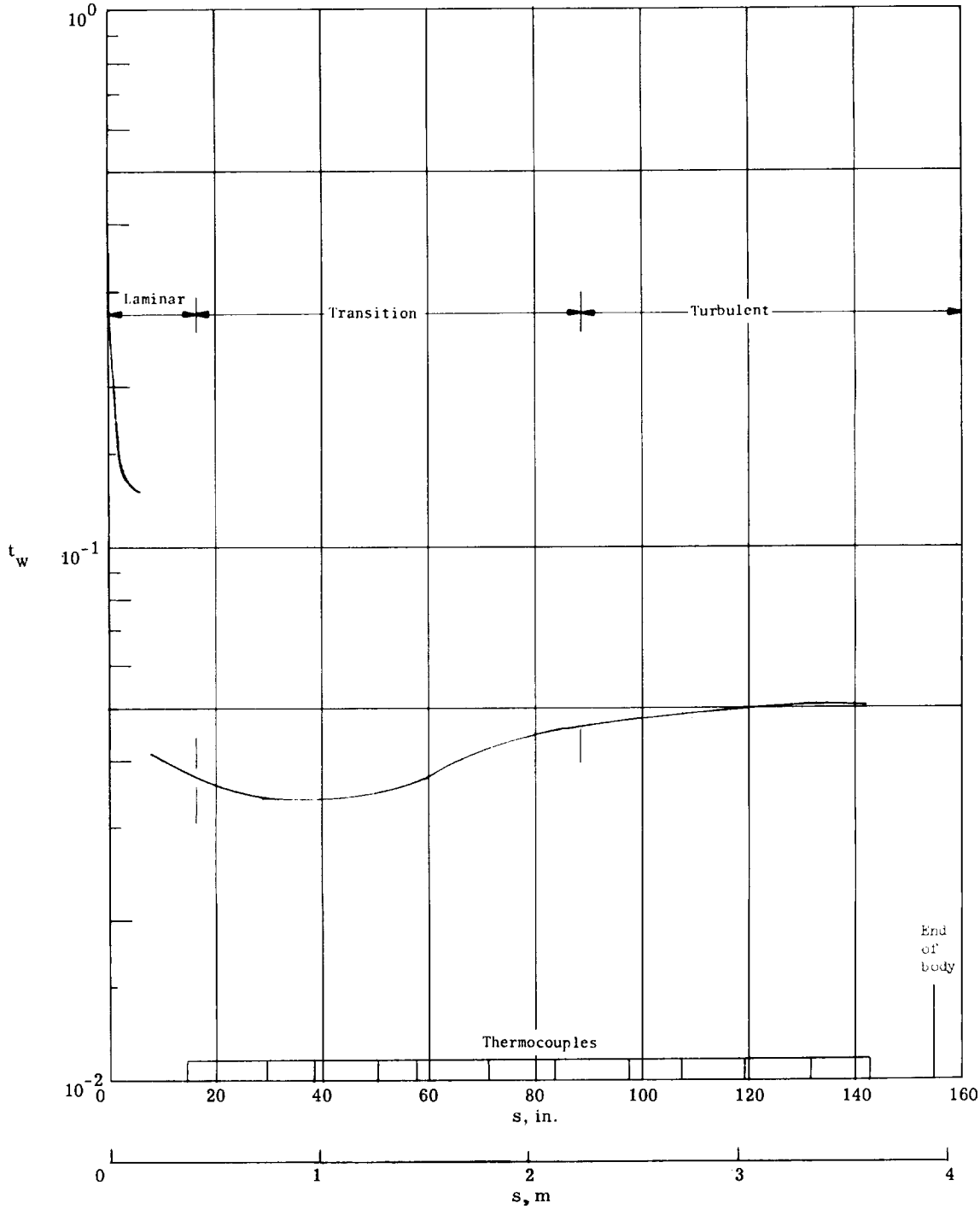

(j) h = 18.29 km (60 000 ft); V_∞ = 5.80 km/sec (19 018 ft/sec); r_n = 3.988 mm (0.157 in.); $\theta_{c,eff} = 3.45^\circ$.

Figure 7.- Concluded.

[redacted]

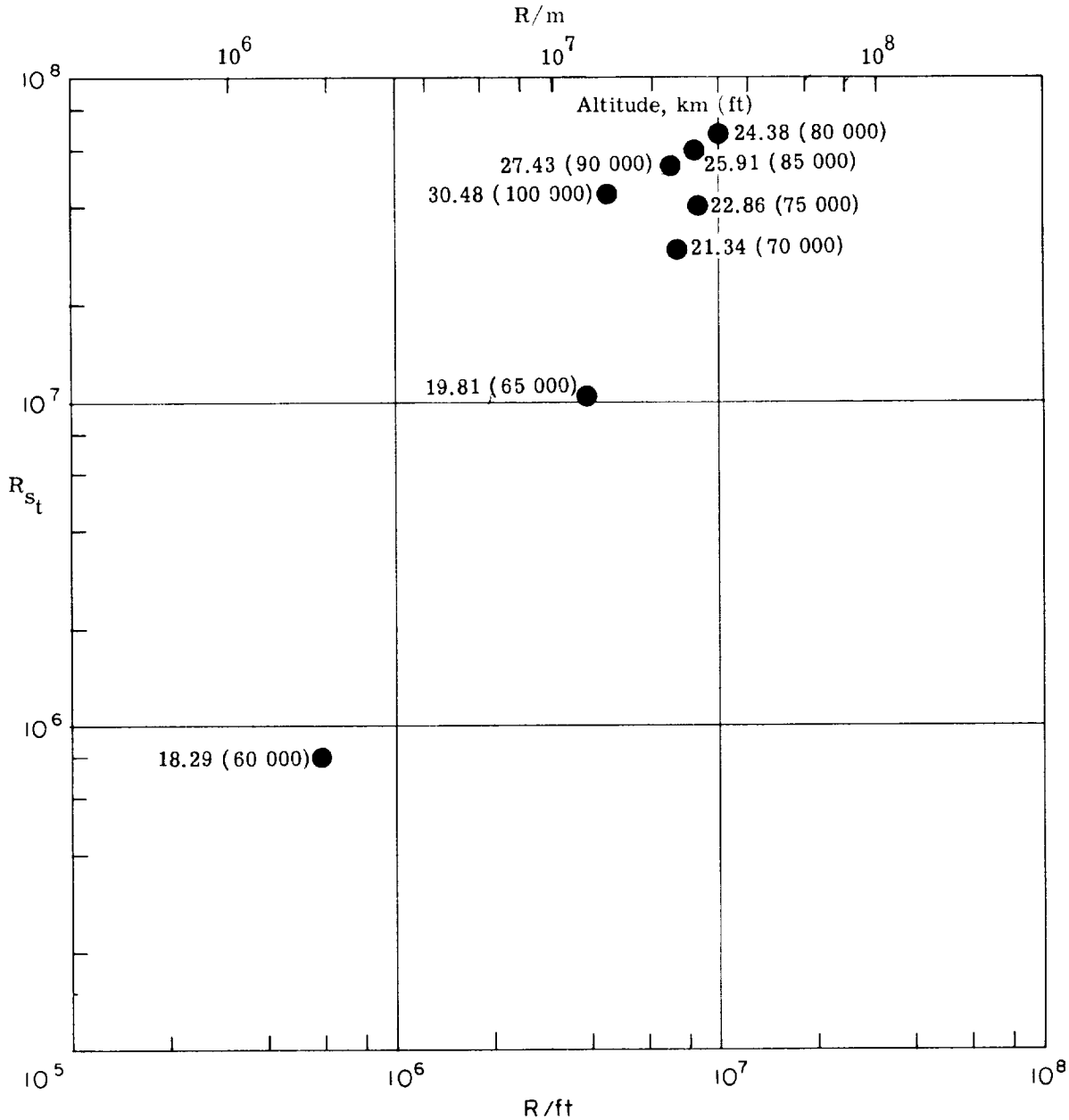

Figure 8.- Local transition Reynolds number as a function of local unit Reynolds number.

[redacted]

[redacted]

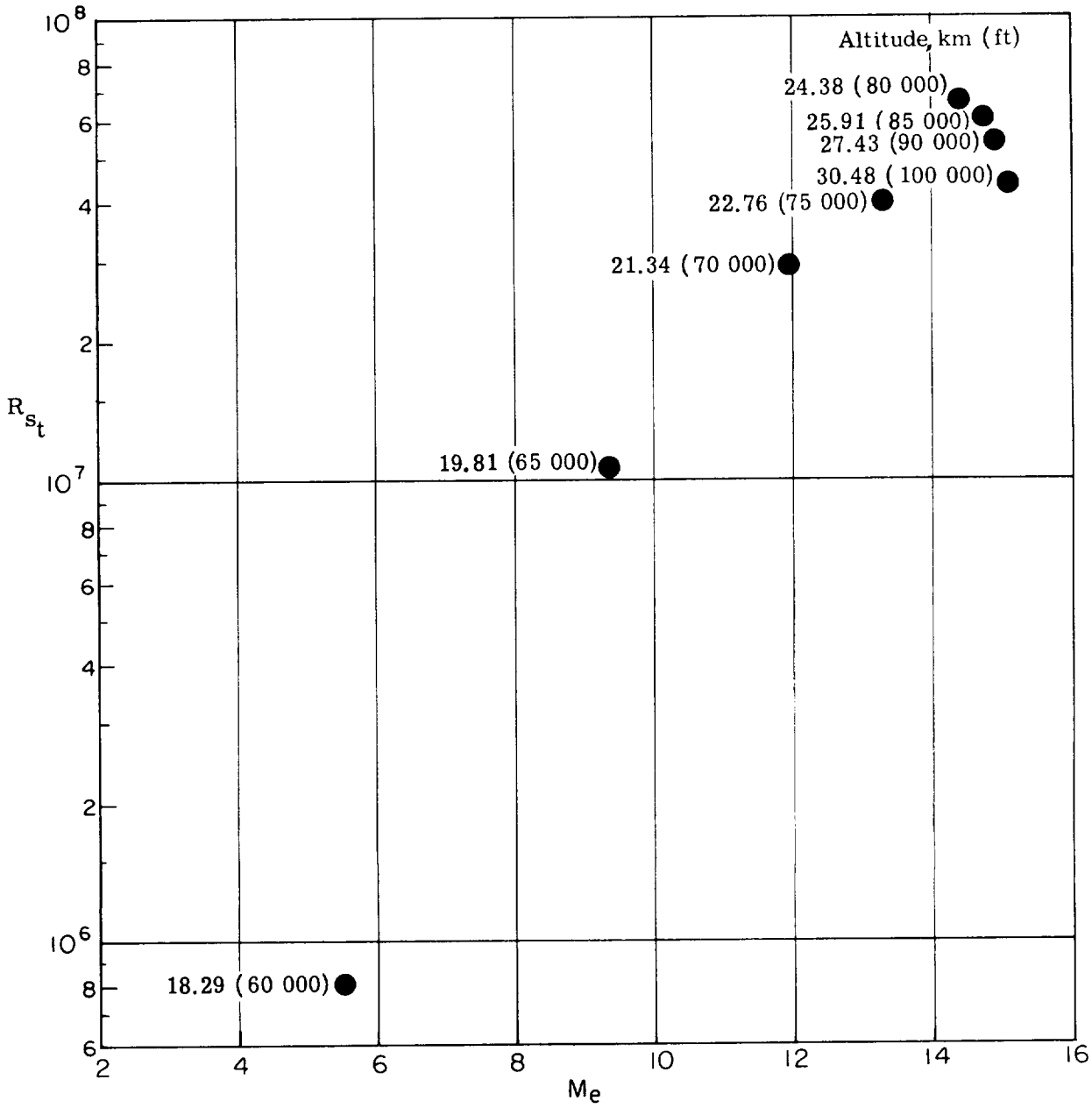

Figure 9.- Local transition Reynolds number as a function of local Mach number.

[redacted]

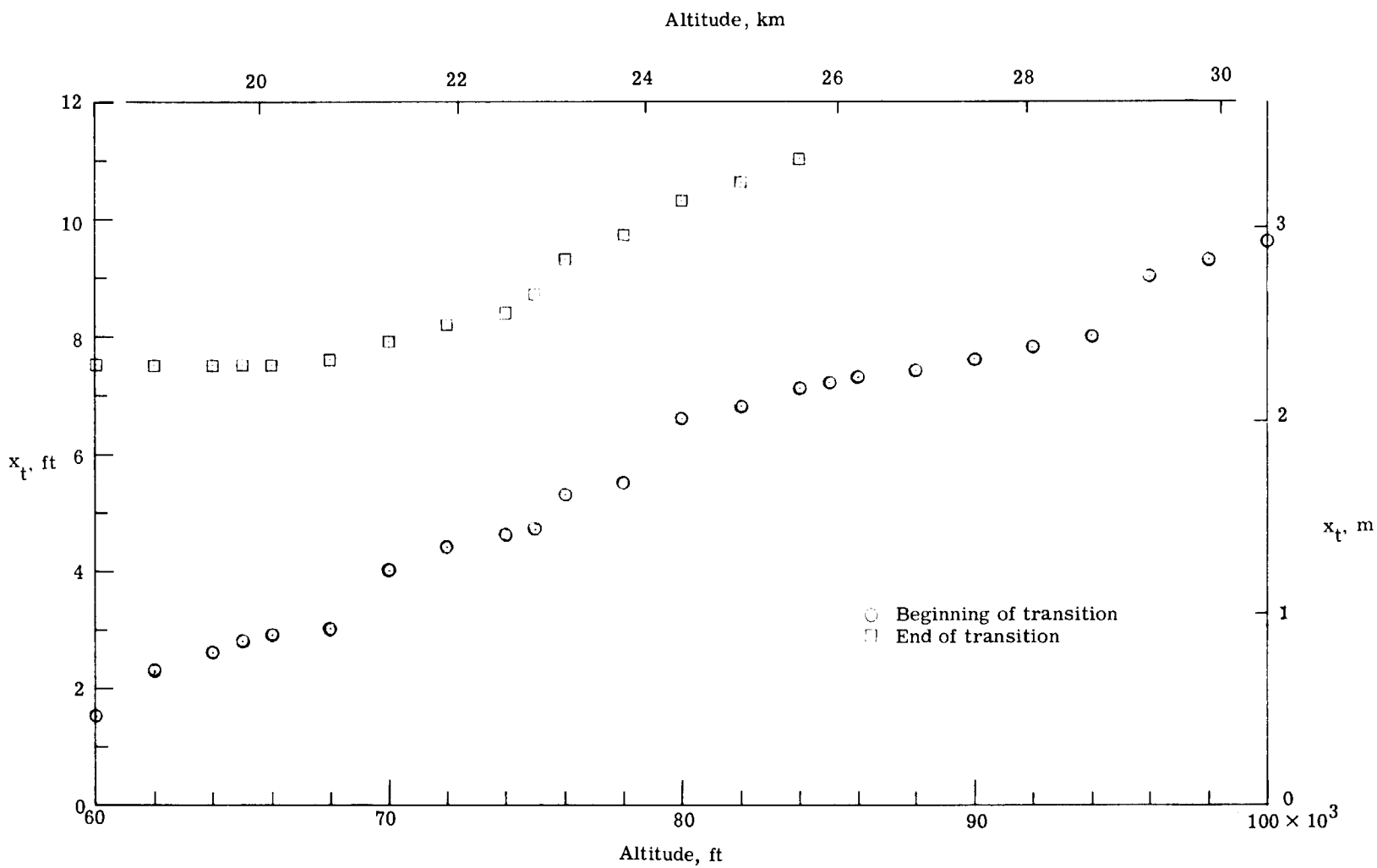

Figure 10.- Axial location of transition from apex of virtual origin obtained from faired curves of heat-transfer data (ref. 5).

[redacted]

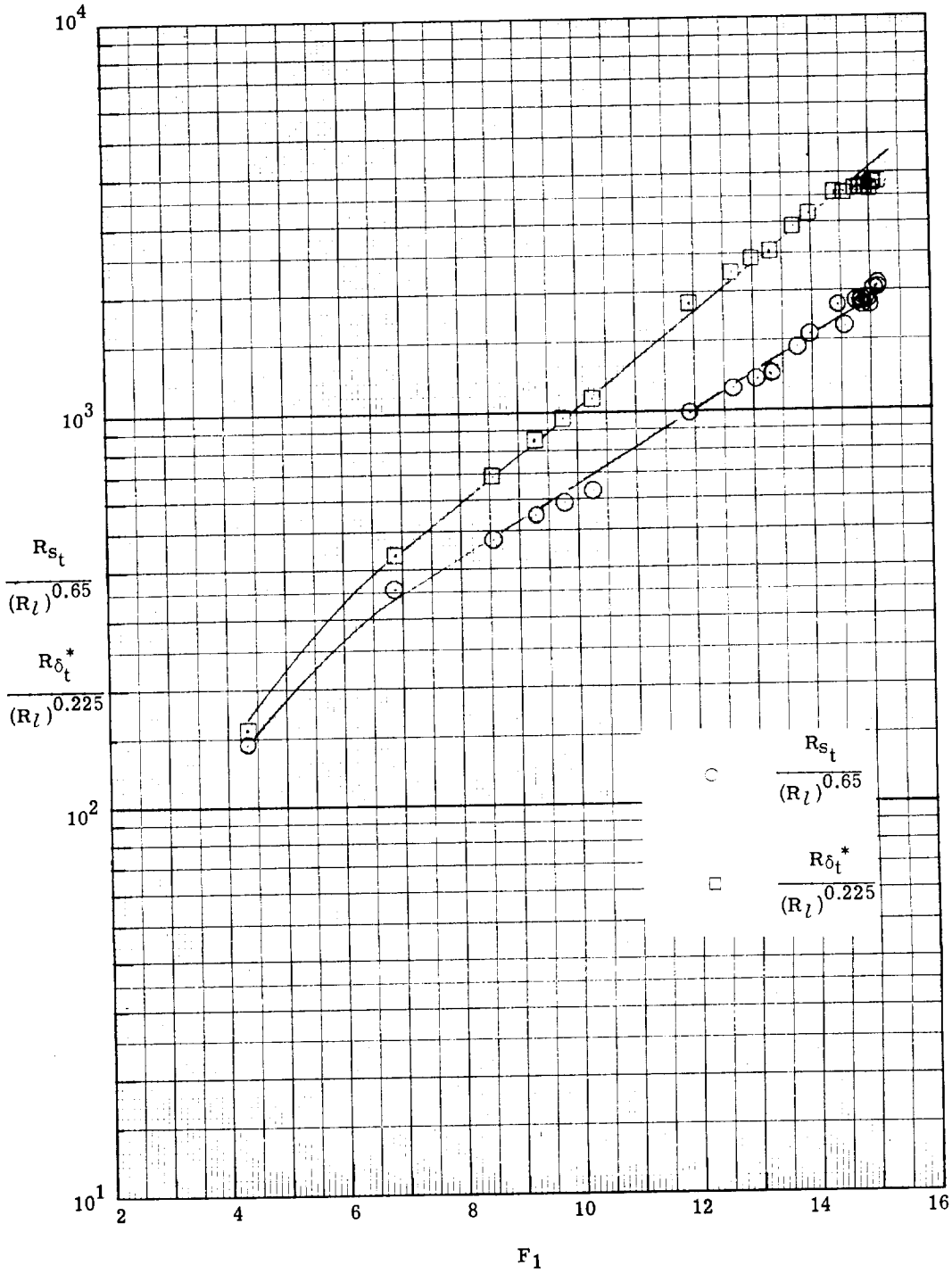

Figure 11.- Correlation of Reentry F transition data in the form of $R_L/(R_l)^n$ as a function of F_1, with $L = \delta_t^*$ and s_t and $l = 0.3048$ m (1.0 ft).

[redacted]

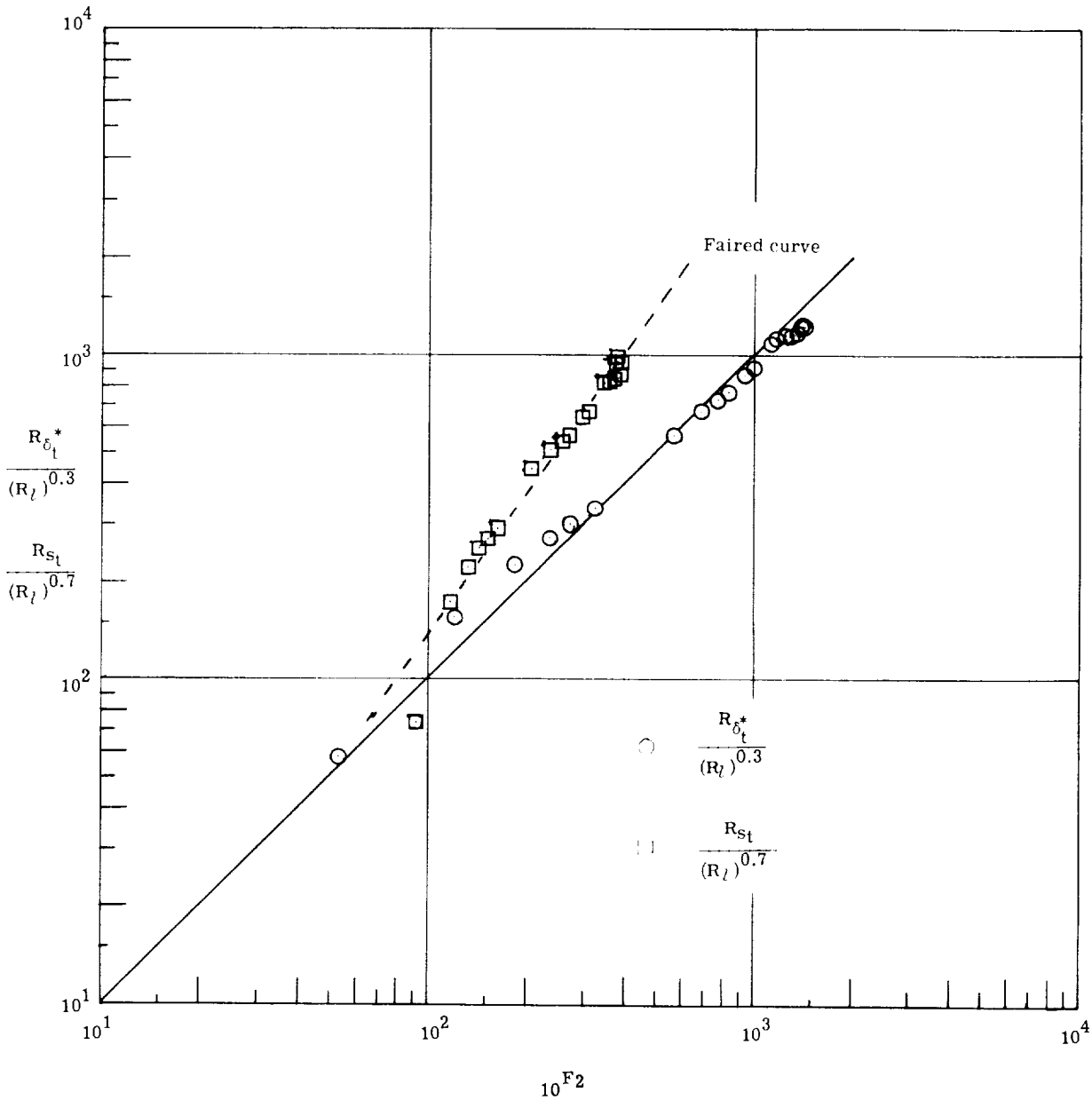

Figure 12.- Correlation of Reentry F transition data in the form of $R_L/(R_l)^n$ as a function of F_2, with $L = \delta_t^*$ and s_t and $l = 0.3048$ m (1.0 ft).

[redacted]

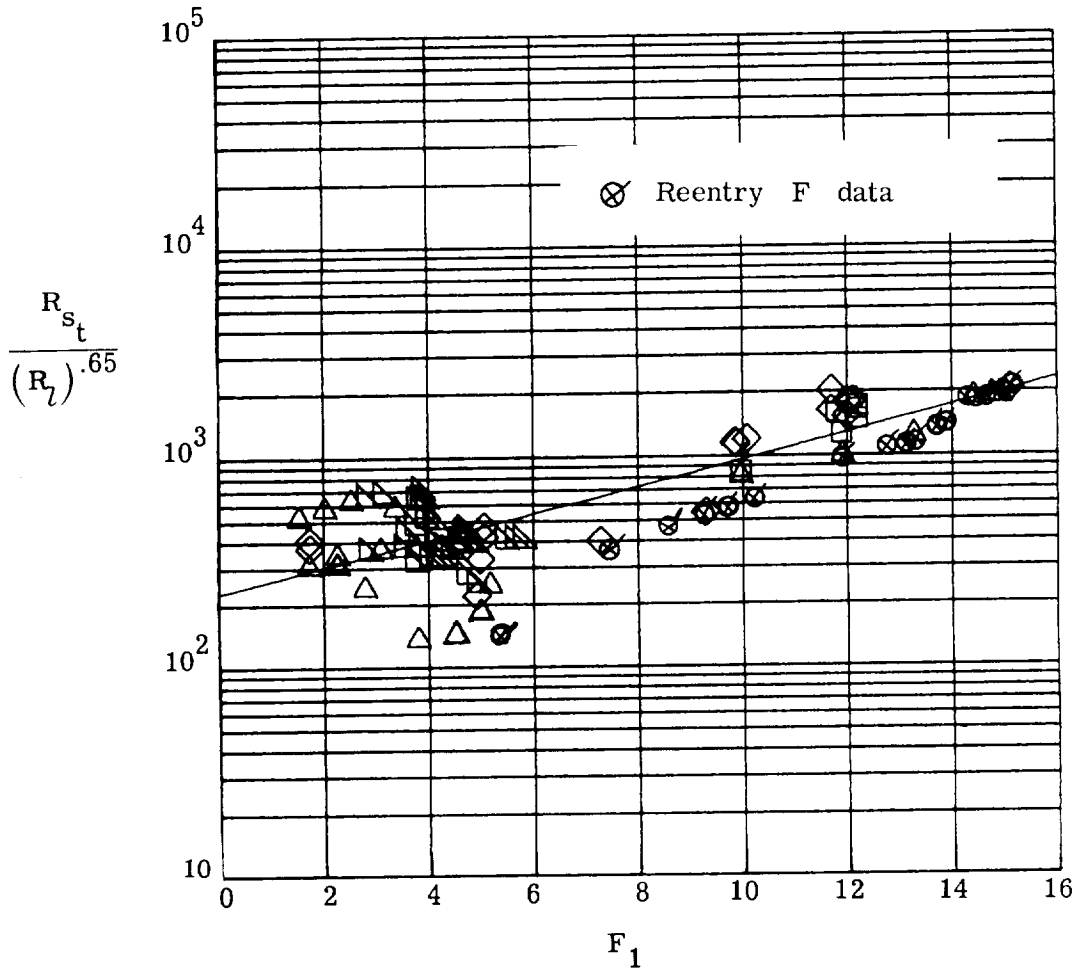

Figure 13.- Comparison of Reentry F data with other flight data in the form of $R_L/(R_l)^{0.65}$ as a function of F_1, with $L = s_t$ and $l = 0.3048$ m (1.0 ft).

[redacted]

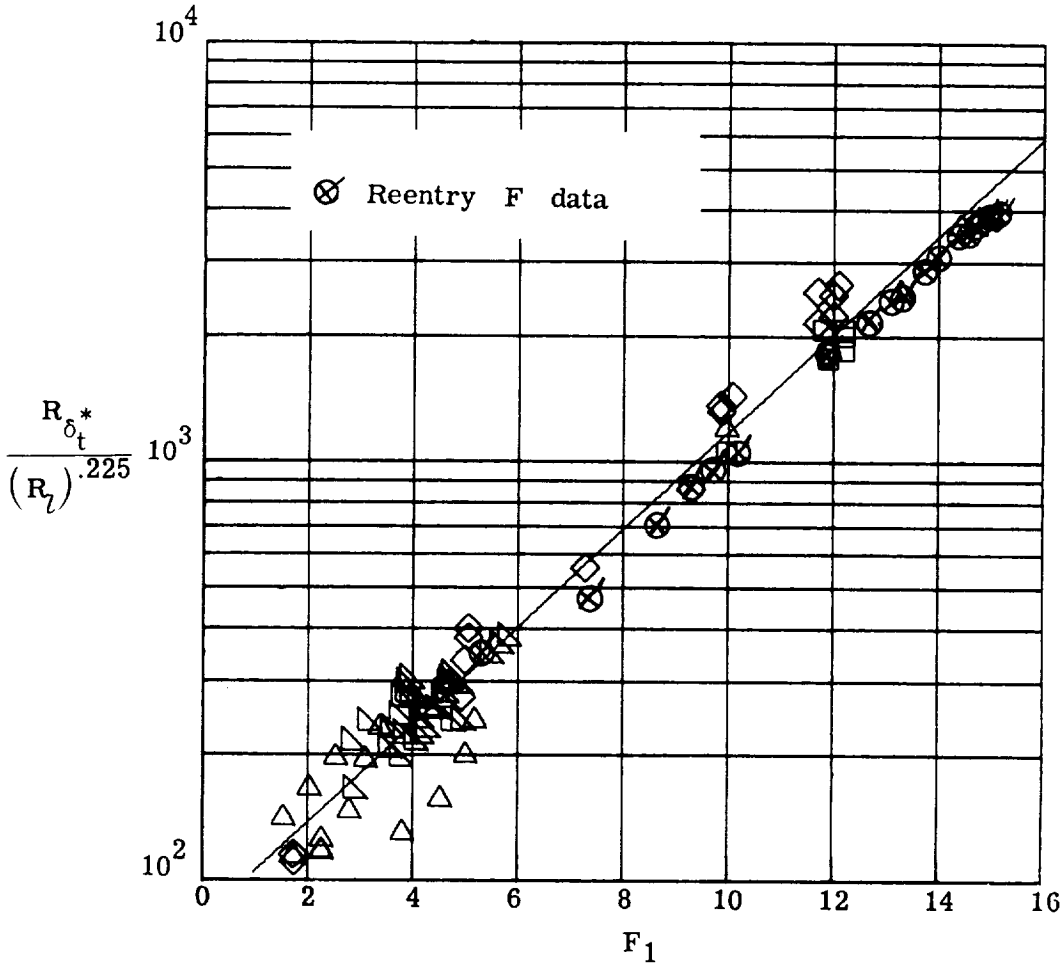

Figure 14.- Comparison of Reentry F data with other flight data in the form of $R_L/(R_l)^{0.225}$ as a function of F_1, with $L = \delta_t^*$ and $l = 0.3048$ m (1.0 ft).

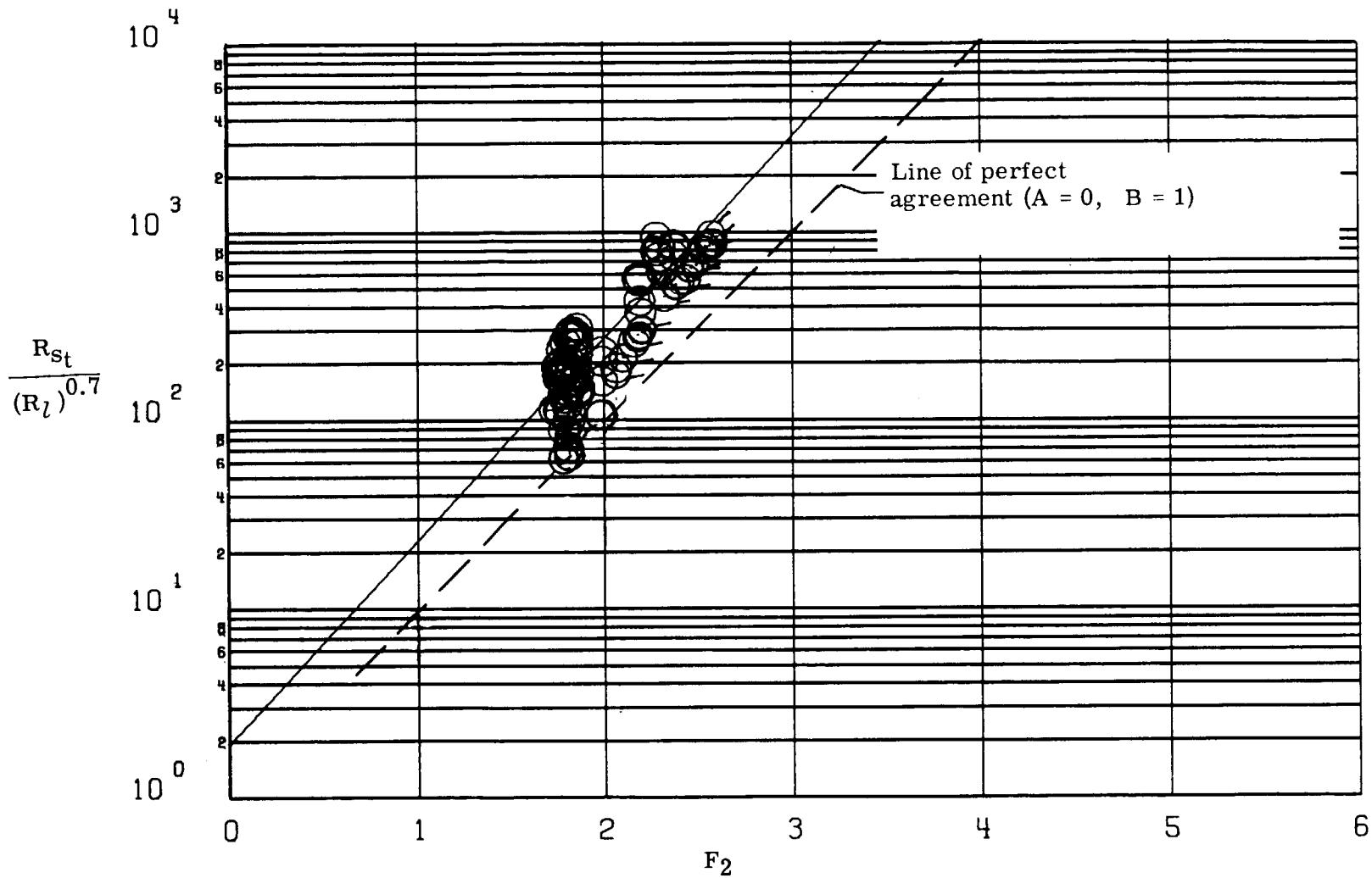

(a) $R_{S_t}/(R_l)^{0.7}$ as a function of F_2.

Figure 15.- Comparison of Reentry F data with other flight data, with $l = 0.3048$ m (1.0 ft). (Flagged symbols represent Reentry F data.)

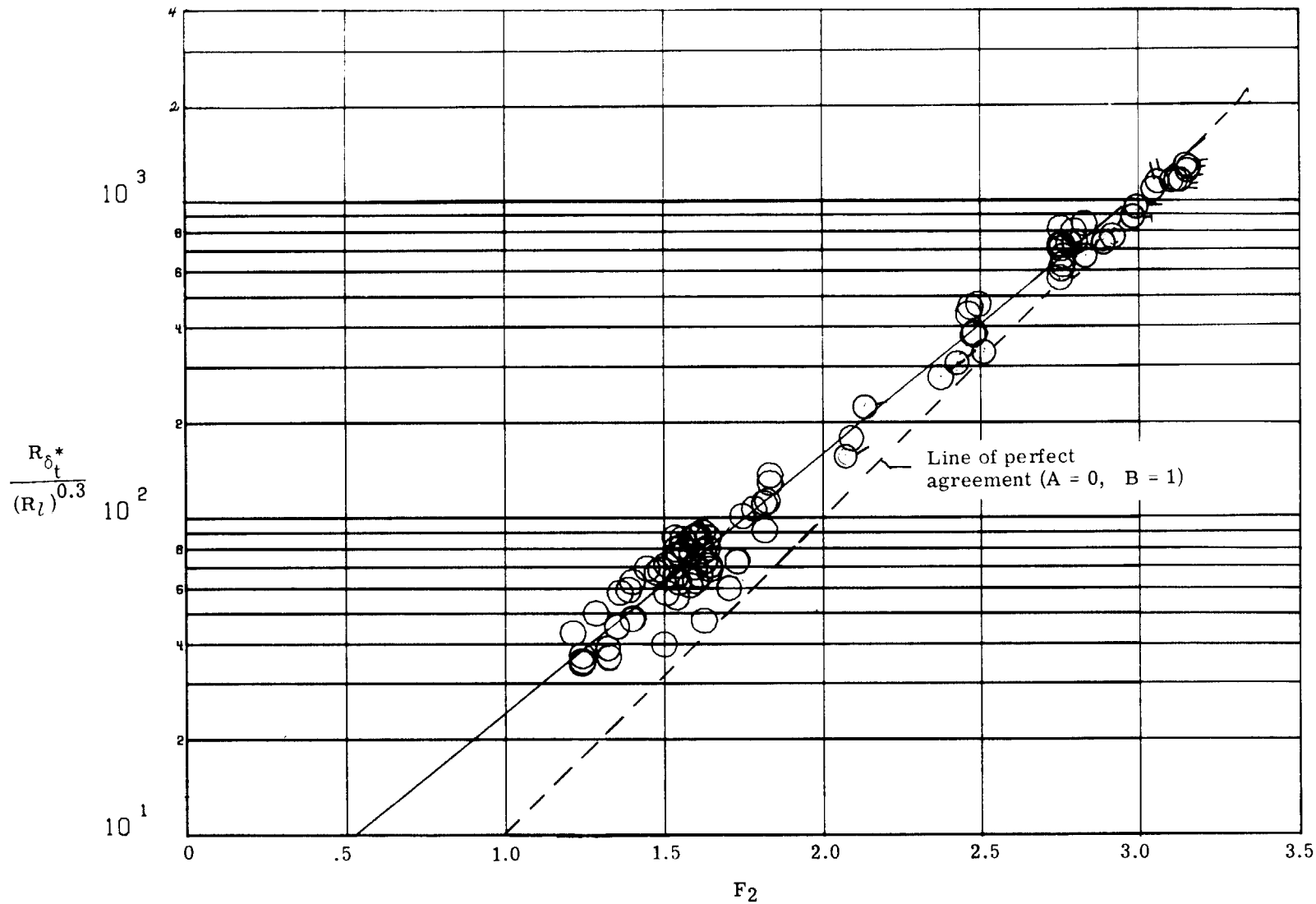

(b) $R_{\delta_t^*}/(R_l)^{0.3}$ as a function of F_2.

Figure 15.- Concluded.

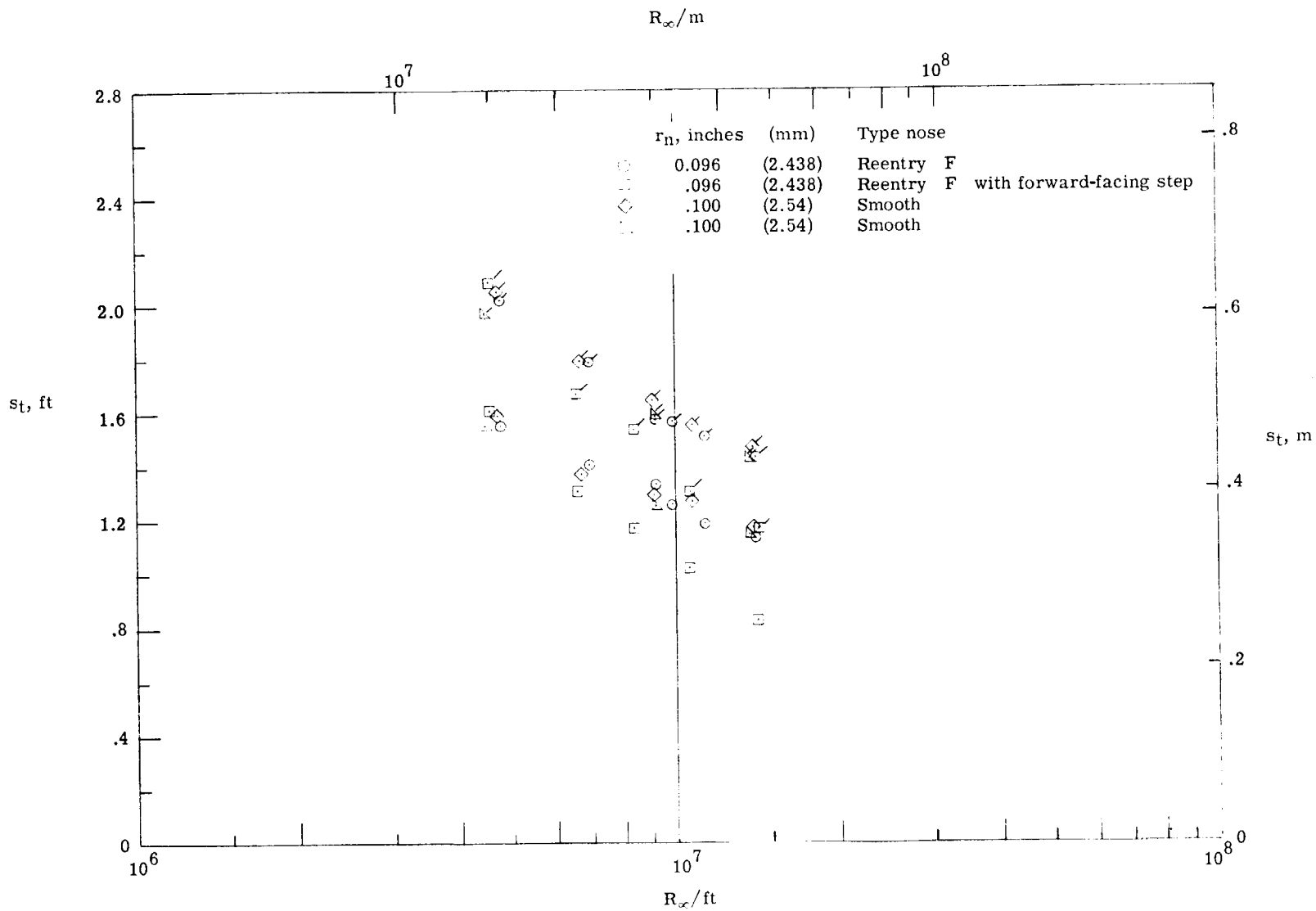

(a) $\alpha = 1.5^{\circ}$; windward ray.

Figure 16.- Effect of unit Reynolds number and nose geometry at $M_\infty = 8$ on transition location. (Flagged symbols represent end of transition.)

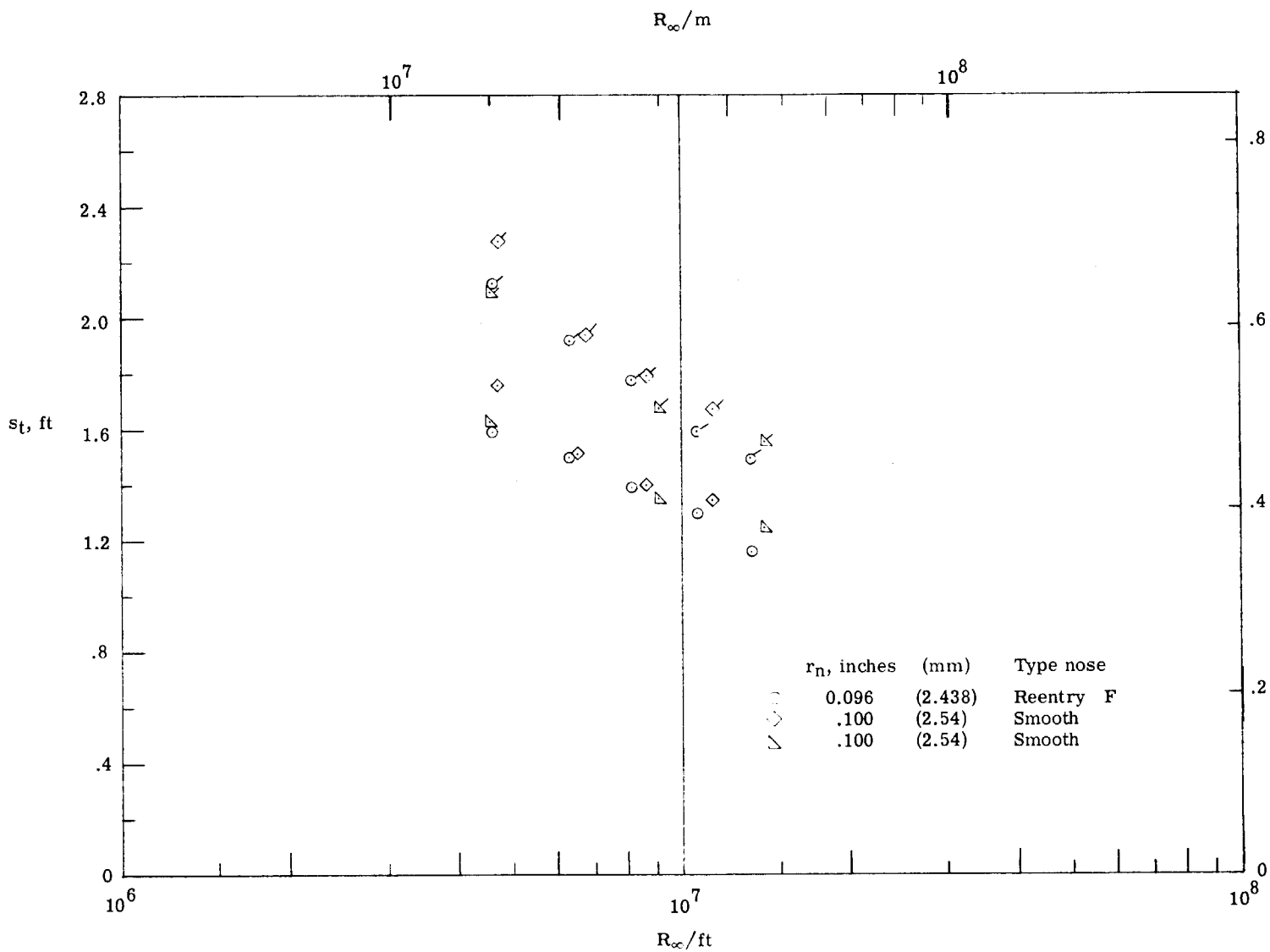

(b) $\alpha = 1.0^{\circ}$; windward ray.

Figure 16.- Continued.

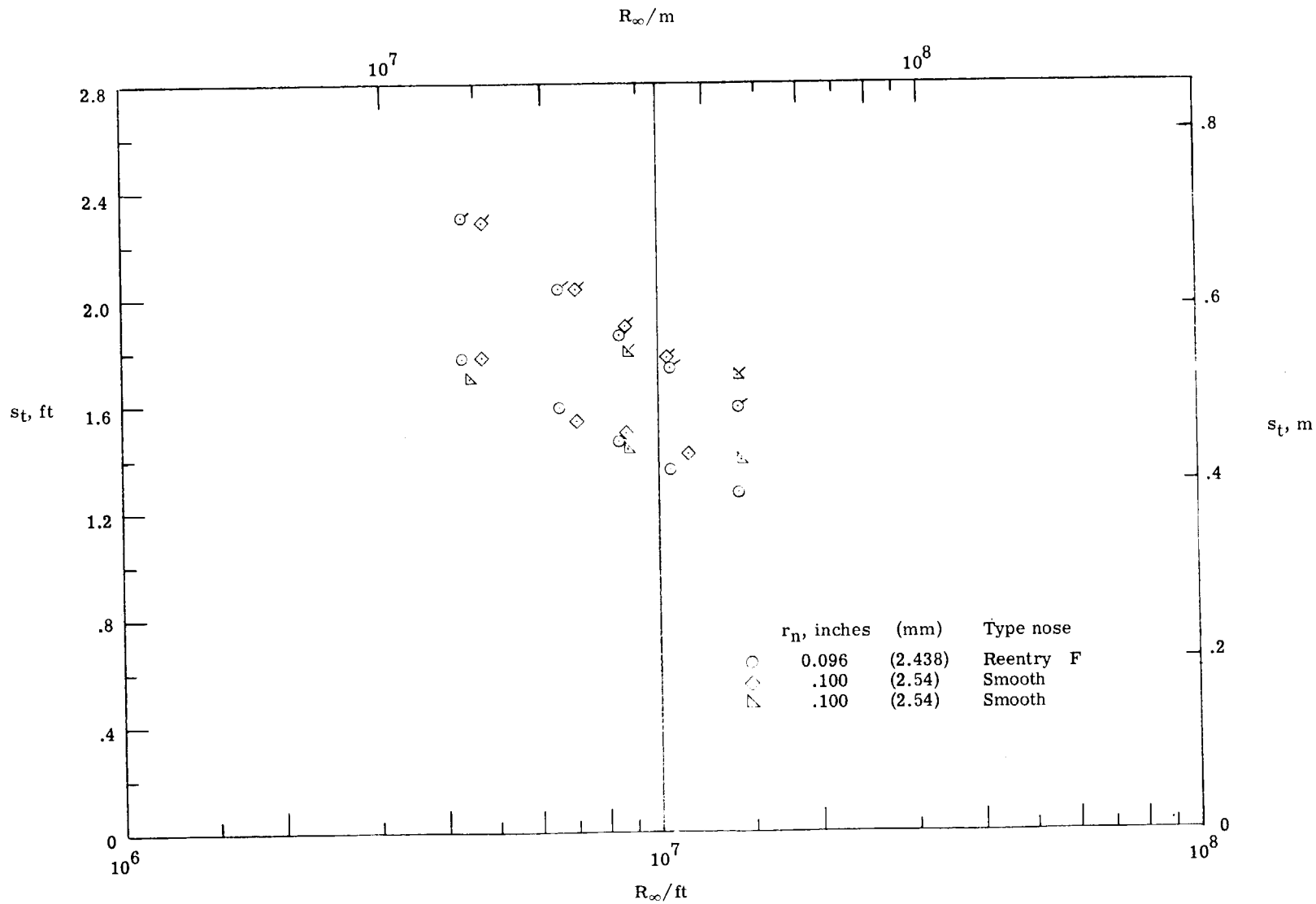

(c) $\alpha = 0.5^{\circ}$; windward ray.

Figure 16.- Continued.

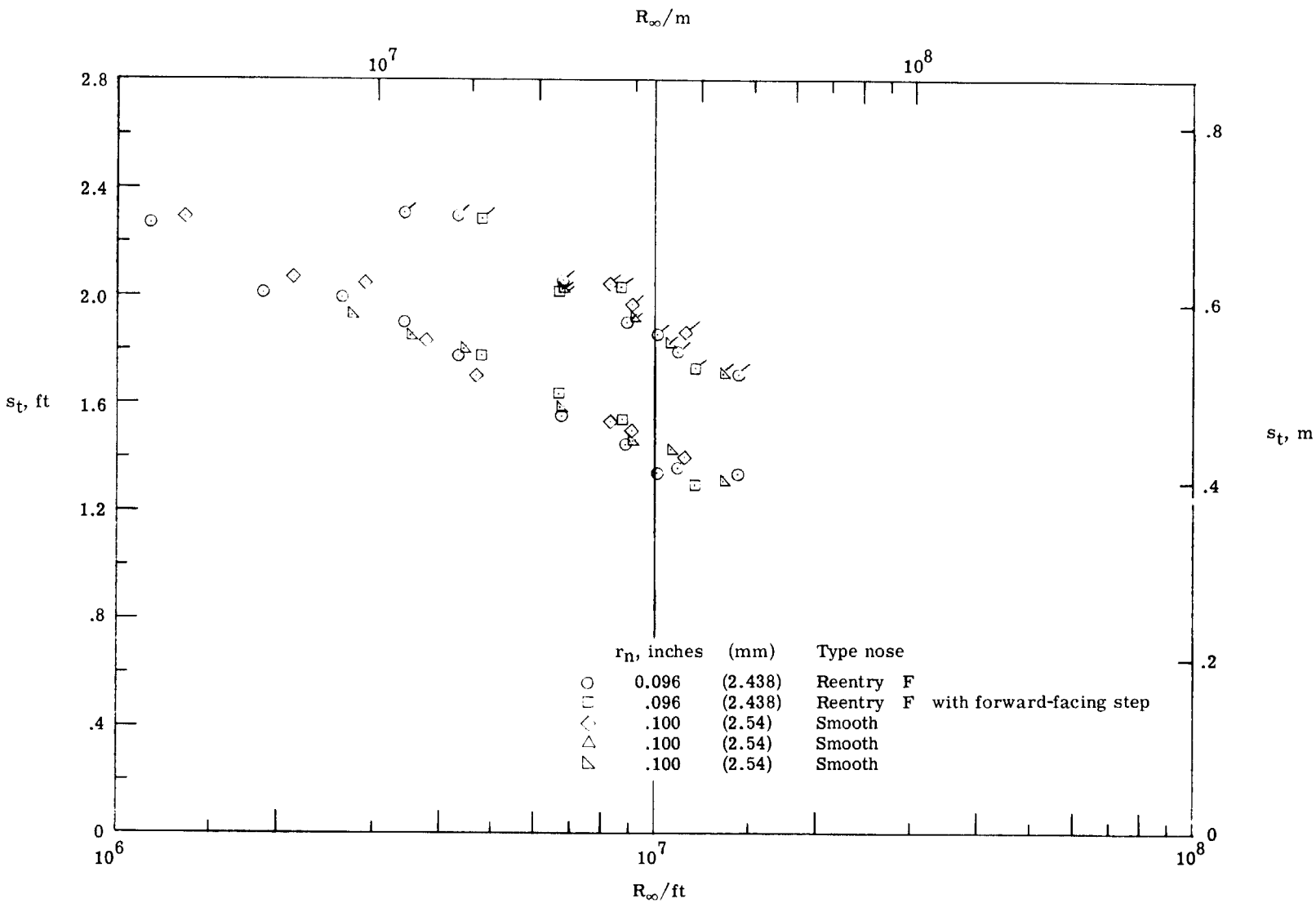

(d) $\alpha = 0^{\circ}$.

Figure 16.- Continued.

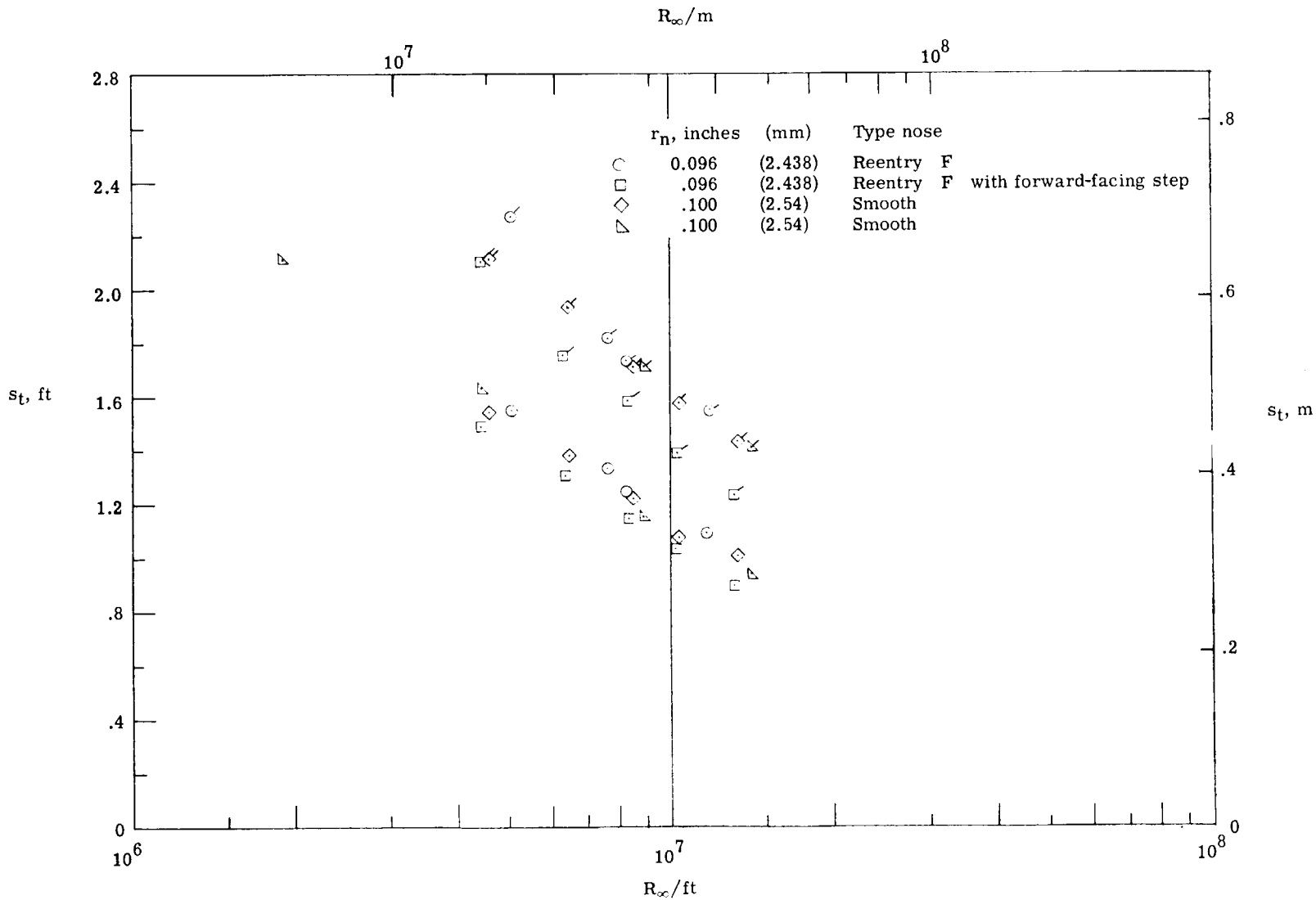

(e) $\alpha = 0.5^{\circ}$; leeward ray.

Figure 16.- Continued.

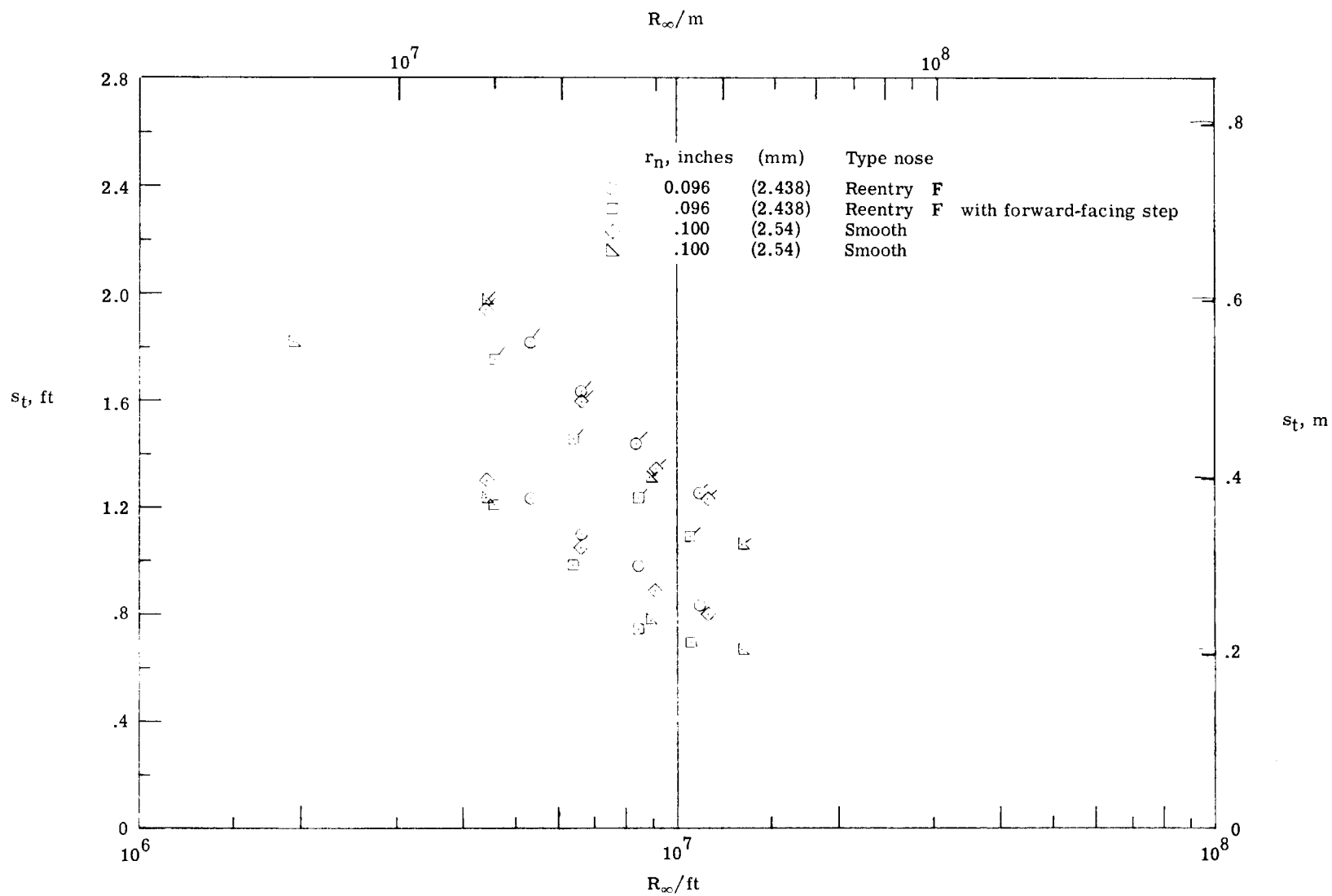

(f) $\alpha = 1.0^{\circ}$; leeward ray.

Figure 16.- Continued.

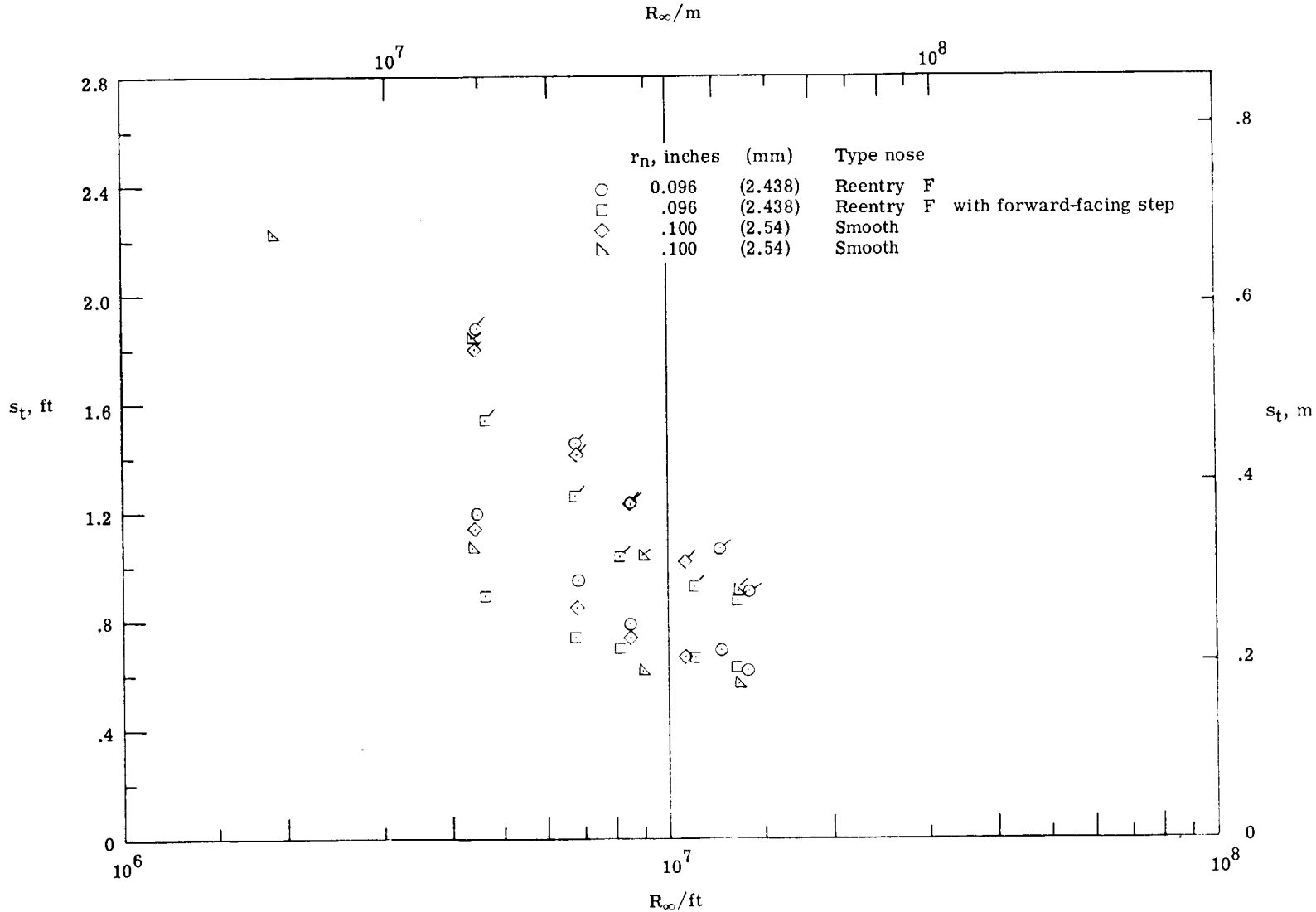

(g) $\alpha = 1.5^{\circ}$; leeward ray.

Figure 16.- Concluded.

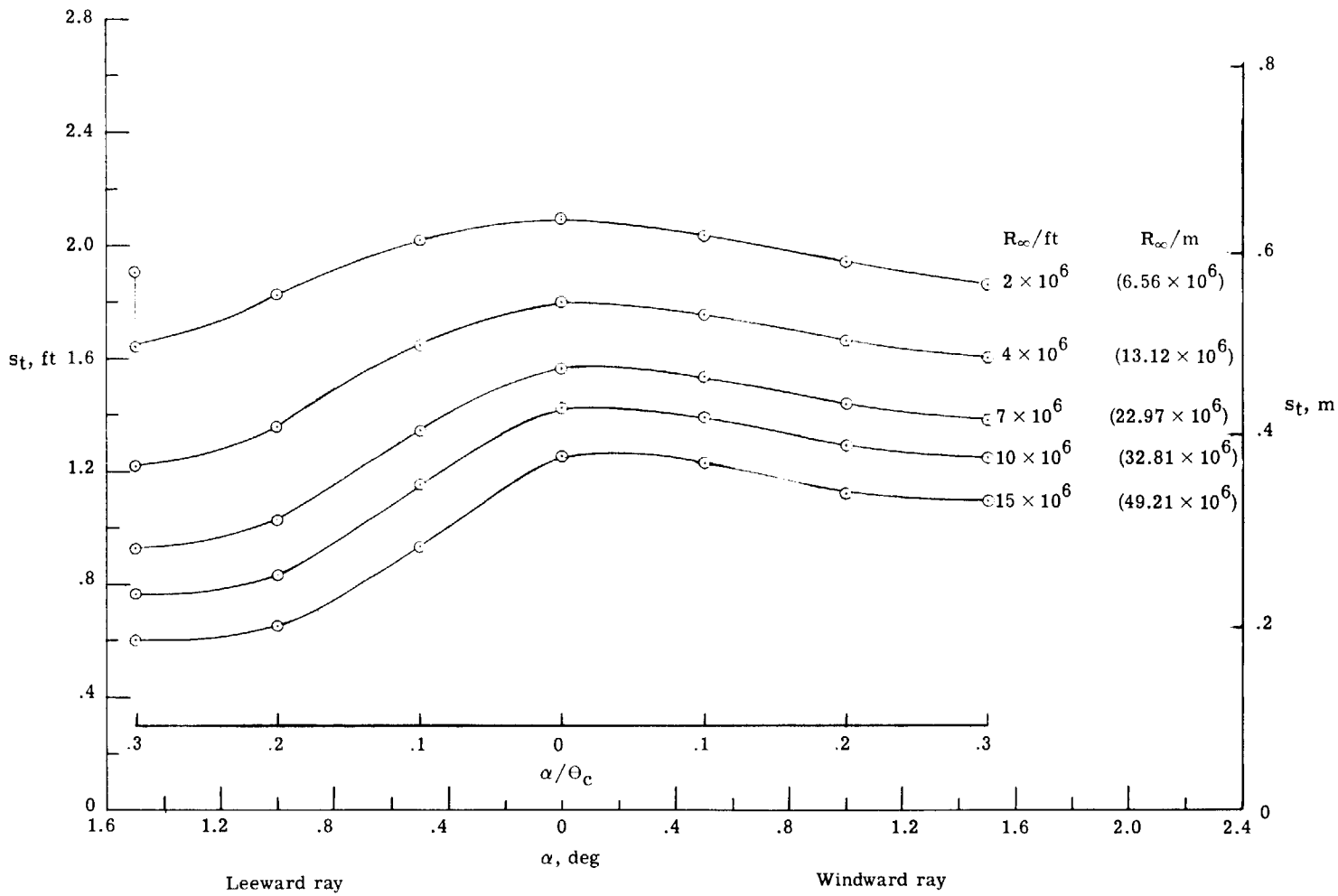

(a) r_n = 2.54 mm (0.100 in.).

Figure 17.- Effect of angle of attack on location of beginning of transition. $M_\infty = 8$.

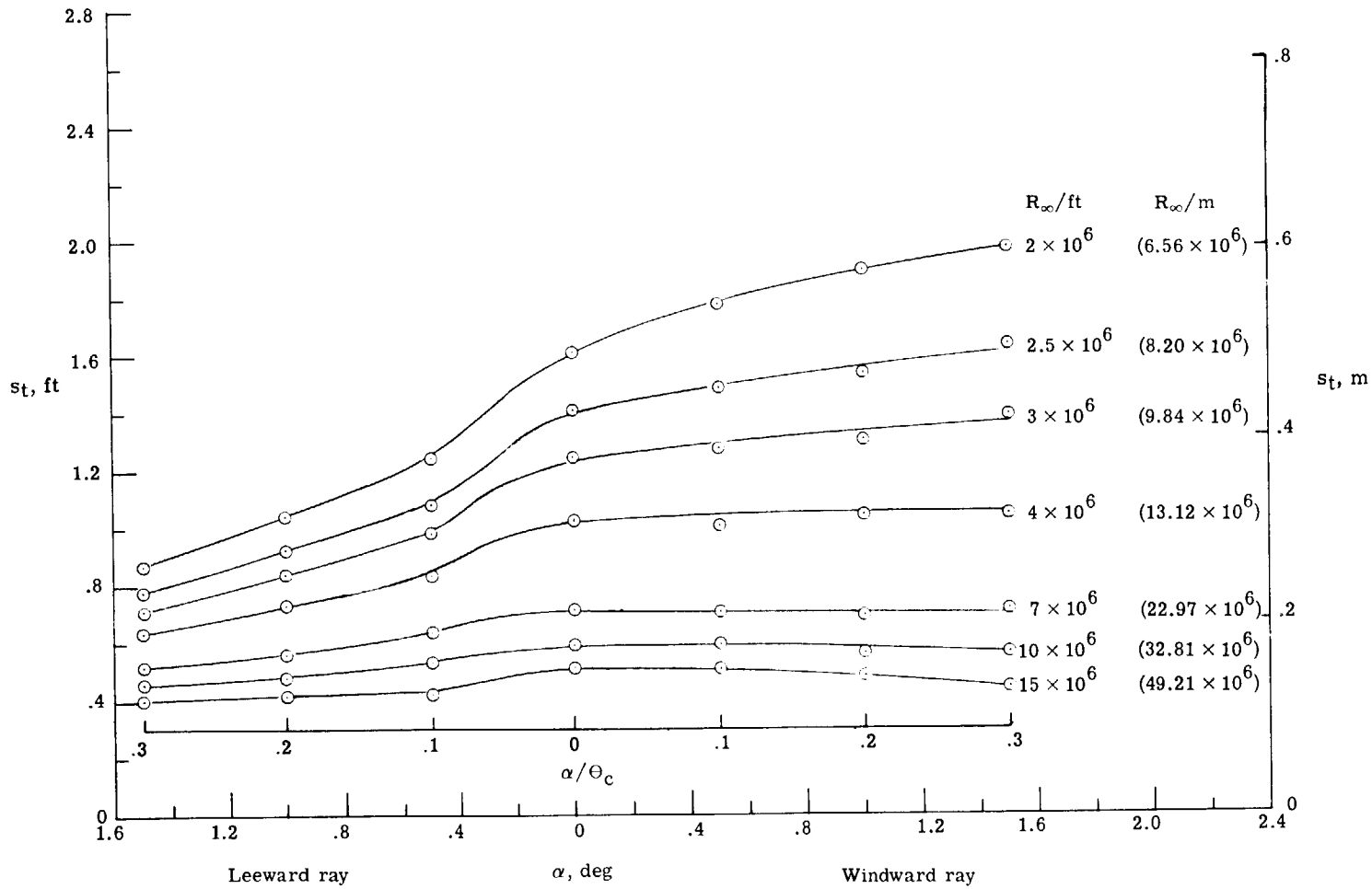

(b) $r_n = 0.508$ mm (0.020 in.).

Figure 17.- Concluded.

NASA-Langley, 1972 — 12 L-8313

[redacted]

"The aeronautical and space activities of the United States shall be conducted so as to contribute . . . to the expansion of human knowledge of phenomena in the atmosphere and space. The Administration shall provide for the widest practicable and appropriate dissemination of information concerning its activities and the results thereof."

—NATIONAL AERONAUTICS AND SPACE ACT OF 1958

NASA SCIENTIFIC AND TECHNICAL PUBLICATIONS

TECHNICAL REPORTS: Scientific and technical information considered important, complete, and a lasting contribution to existing knowledge.

TECHNICAL NOTES: Information less broad in scope but nevertheless of importance as a contribution to existing knowledge.

TECHNICAL MEMORANDUMS: Information receiving limited distribution because of preliminary data, security classification, or other reasons.

CONTRACTOR REPORTS: Scientific and technical information generated under a NASA contract or grant and considered an important contribution to existing knowledge.

TECHNICAL TRANSLATIONS: Information published in a foreign language considered to merit NASA distribution in English.

SPECIAL PUBLICATIONS: Information derived from or of value to NASA activities. Publications include conference proceedings, monographs, data compilations, handbooks, sourcebooks, and special bibliographies.

TECHNOLOGY UTILIZATION PUBLICATIONS: Information on technology used by NASA that may be of particular interest in commercial and other non-aerospace applications. Publications include Tech Briefs, Technology Utilization Reports and Notes, and Technology Surveys.

Details on the availability of these publications may be obtained from:

SCIENTIFIC AND TECHNICAL INFORMATION OFFICE

NATIONAL AERONAUTICS AND SPACE ADMINISTRATION

Washington, D.C. 20546

[redacted]